Hochschule Karlsruhe
University of
Applied Sciences

Fakultät Elektro- und Informationstechnik

**Studiengang Elektro- und Informationstechnik,
Elektromobilität und Erneuerbare Energien**

Master Thesis

In collaboration with: European Organization for Nuclear Research (CERN)
Instituto Nazionale de Fisica Nucleare (INFN Genoa)

Simulation of quench behaviour of the recombination dipole magnet for the LHC High Luminosity upgrade

created by

Lennard Bender

No. 456

Matrikelnummer: 66654

Referent: Prof. Dr. Jürgen Weizenecker
Co-referent: Prof. Dr. Klaus Wolfrum

Workplace: CERN
Supervisor: Dr. Emmanuele Ravaioli (CERN Geneva)
Supervisor: Dr. Barbara Caiffi (INFN Genoa)

Time period: 04/01/2022 - 09/30/2022

Abstract

Superconducting magnets are one of the key components of particle accelerators. Their safety and integrity as well as understanding their behavior is of great interest. In order to simulate the complex transients occurring in superconducting magnet circuits, the STEAM framework, which consists of dedicated software tools and model libraries, was developed at CERN. To enhance repeatability, consistency, traceability and versioning the STEAM framework was recently restructured into an interconnected Python framework called STEAM-SDK. This thesis describes the validation process of the recombination dipole magnet (MBRD) model, which will be part of the High Luminosity LHC, using the STEAM-SDK structure. A LEDET 2D electro-magnetic and thermal model is able to simulate quench transients at high current very well. To improve the model at low current the quench propagation in the third dimension can be included in LEDET. To capture the quench transient of a quench heater protected magnet at all current levels a consecutive simulation process, consisting of LEDET and PyBBQ is proposed. By modelling the longitudinal quench propagation in the coil turns in thermal contact to quench heaters with PyBBQ it is possible to account for cooling effects occurring due to superfluid helium. The PyBBQ output can be used as initial value for the propagation in the third dimension in LEDET. In this thesis a generalized function for quench heater protected magnets is developed and implemented in STEAM-SDK structuring the simulation process and thereby allowing in the future efficient and fast simulation and model validation against experimental results. The validated model of MBRD is used to predict key parameters in different operation scenarios and failure cases. On the basis of these results an alternative protection to the original baseline is proposed aiming for a significant reduction of hot-spot temperature and voltage to ground.

Kurzfassung

Hunderte supraleitende magnete sind das Herzstück des Large Hadron Collider (LHC) am CERN. Ihr sicherer Betrieb, sowie ein genaues Verständnis ihres Verhaltens sind somit von großer Bedeutung. Das Modellieren komplexer Vorgänge in supraleitenden Magneten ist durch das am CERN entwickelte STEAM Framework möglich geworden. Um Wiederholbarkeit, Konsitenz, Rückverfolgbarkeit und Versionierung zu optimieren, wurde der aus einzelnen, unabhängigen Programmen bestehende Verbund vor Kurzem in ein vernetztes Python Framework namens STEAM-SDK umstrukturiert. Unter Verwendung der STEAM-SDK-Struktur beschreibt diese Arbeit den Validierungsprozess eines Simulationsmodels des Rekombinations-Dipolmagneten (MBRD), welcher Teil des High Luminosity LHCs sein wird. Die Modellierung der longitudinalen Quenchausbreitung, mit dem STEM tool PyBBQ, in den Teilen des Magneten, die in thermischem Kontakt zu den Quench Heatern stehen, ermöglicht es Kühleffekte zu berücksichtigen, die durch superfluides Helium entstehen. Unter der Berücksichtigung des PyBBQ outputs im STEAM tool LEDET kann der Entladevorgang eines Quench Heater geschützten Magneten bei allen Stromstärken simulativ erfasst werden. In dieser Arbeit wird eine verallgemeinerte Python Funktion für Quench Heater geschützte Magnete entwickelt und in die STEAM-SDK-Struktur eingebettet. Durch ihre Nutzung sind in Zukunft effiziente und schnelle Simulations- und Validierungsprozesse dieses Magnettyps möglich. Außerdem wird das validierte Model des MBRD Dipolmagneten zur Vorhersage von Schlüsselparametern in verschiedenen Betriebsszenarien und Fehlerfällen des Magneten verwendet. Auf Basis dieser Ergebnisse wird eine Alternative zum bestehenden Schutzkonzept vorgeschlagen, die eine erhebliche Reduzierung der Hot-Spot-Temperatur und der Spannung gegen Erde gewährleistet.

Declaration on oath

I hereby declare, on oath, that I have written the present thesis by my own and have not used other than the acknowledged resources and aids.

Eidesstattliche Erklärung

Hiermit erkläre ich an Eides statt, dass ich die vorliegende Thesis selbst verfasst und keine anderen als die angegebenen Quellen und Hilfsmittel benutzt habe.

Place, Date

Signature

Contents

Acronyms

Abbriviation	Full word
AC	Alternating current
ALICE	A Large Ion Collider Experiment
ATLAS	A Toroidal LHC-Aparatus
AWAKE	Advanced Proton Driven Plasma Wakefield Acceleration Experiment
BBQ	Bus Bar Quench
CCT	Canted Cosine Theta
CERN	Conseil européen pour la recherche nucléaire
CLIQ	Coupling-Loss Induced Quench
CMS	Compact Muon Solenoid
COSIM	Co-operative Simulation
EE	Energy extraction
ELENA	The Extra Low Energy Antiproton ring
FiQuS	Finite Elements Quench Simulator
GetDP	A General Environment for the Treatment of Discrete Problems
He II	Super-fluid helium at 1.9 K
HL	High Luminosity
IFCC	Inter-filament coupling currents
IFCL	Inter-filament coupling loss
INFN	National Institute for Nuclear Physics
ISCC	Inter-starnd coupling currents
ISCL	Inter-starnd coupling loss
ISOLDE	Isotope Separator Online Device
LEDET	Lumped-Element Dynamic Electro-Thermal
LHC	Large Hadron Collider
LHCb	Large Hadron Collider beauty
MBRD	Recombination dipole magnet
MBXF	Separation dipole magnet
MQSX	Main quadrupole
Nb-Ti	Niobium-titanium
Nb_3Sn	Niobium3-Tin
NIST	National Institute of Standards and Technology
ProteCCT	Protection of Canted Cosine Theta
PyBBQ	Python based Bus Bar Quench
QH	Quench heaters
RMS	Root Mean Square
RRR	Residual-resistance ratio
SDK	Software Development Kit
SIGMA	STEAM Integrated Generator of Magnets for Accelerators
SING	STEAM Integrated Network Generator
STEAM	Simulation of Transient Effects in Accelerator Magnets
YAML	Yet Another Markup Language

Symbols

Symbol	Unit	Description
A	m^2	Area
A_{bare}	m^2	Area of a bare cable
$A_{insulated}$	m^2	Area of a cable including the insulation
$A_{strands}$	m^2	Area of the strands in a cable
B	T	Magnetic flux
$\vec{B}$	T	Vector of magnetic flux
B_c	T	Critical field
B_{c1}	T	Lower critical field
B_{c2}	T	Upper critical field
C_{CLIQ}	F	Capacitance of CLIQ-system
$C_{th,b}$	F	Electric analogy to heat capacity
$\bar{c}$	$\frac{J}{m^3K}$	Volumetric heat capacity
$d_{strands}$	m	Diameter of a strand
E	J	Energy
$\vec{F}$	N	Vector of force
f_{eff}		Effective transverse resistivity
$f_{external,voids}$	%	Fraction of cross-section of a cable associated to external voids
$f_{insulation}$	%	Fraction of cross-section of a cable associated to the insulation
$f_{internal,voids}$	%	Fraction of cross-section of a cable associated to internal voids
$f_{strands}$	%	Fraction of cross-section of a cable associated to the strands
f_{voids}	%	Fraction of cross-section of a cable associated to all voids
f_{vq}	%	Scaling factor of quench propagation velocity
h_{bare}	m	Height of a bare cable
h_{ins}	m	Thickness of the insulation along the height of a cable
I	A	Current
I_{CLIQ}	A	Current of CLIQ-system
I_e	A	Current in element of electrical sub-network
$I_{if,b}$	A	Analogy to heat source of inter filament coupling
$I_{if,x}$	A	Analogy to heat source of inter filament coupling in x-direction
$I_{if,y}$	A	Analogy to heat source of inter filament coupling in y-direction
$I_{is,b}$	A	Analogy to heat source of inter strand coupling
$\mathrm{I_{meas}}$	A	Measured current through the magnet during the discharge
I_{nom}	A	Nominal current
$I_{ohm,b}$	A	Electric analogy to heat source ohmic loss
$\mathrm{I_{QH2}}$	A	Measured current quench heater 2

$\mathrm{I}_{\mathrm{QH5}}$	A	Measured current quench heater 5
I_{ult}	A	Ultimate current
J	$\frac{A}{m^2}$	Current density
J_c	$\frac{A}{m^2}$	Critical current density
κ	$\frac{W}{mK}$	Thermal conductivity
L	H	Inductivity
L_{CLIQ}	H	Inductivity of CLIQ system
L_a	H	Inductivity of coil element
L_{cc}	H	Inductance of the external coupling circuit
L_n	H	Inductivity of coil element
l_{cu}	m	Length of copper plated parts of QH
l_{magnet}	m	Length of a magnet
l_{QH}	m	Length of a heating station
l_q	m	Initial length of a quench
$\vec{l}$		Direction of a conductor
M		Coupling of coil elements
M_{cc}		Coupling element to the external coupling circuit
MIIT	$10^6 A^2 s$	Quench load
μ_0	$\frac{H}{m}$	Vacuum permeability
n		Number of units
$n_{QH,stations}$		Number of heating stations
n_l		Number of layers of a cable
$n_{s,l}$		Number of strands per layer of a cable
$n_{strands}$		Number of strands in a cable
P_{cc}	W	Heat source coupling loss
P_{ex}	W	Heat exchange
P_{if}	W	Heat source inter filament coupling
P_{is}	W	Heat source inter strand coupling
P_{ohm}	W	Heat source ohmic loss
P_{sink}	W	Heat flow to helium
p	m	Perimeter
$per_{external}$	m	Perimeter to take external cooling into account
$per_{internal}$	m	Perimeter to take internal cooling into account
per_{total}	m	Perimeter of rectangular cable
p_1	m	Distance of point 1 to the beginning of the conductor
p_2	m	Distance of point 2 to the beginning of the conductor
q	C	Charge of an electron
$R_{Circuit}$	Ω	Electric resistance of magnet cabling
R_{CLIQ}	Ω	Electric resistance of CLIQ-system
$R_{Coil,a}$	Ω	Electric resistance of coil element

$R_{Coil,n}$	Ω	Electric resistance of coil element
$R_{Crowbar}$	Ω	Electric resistance of crowbar
R_b	Ω	Electric analogy to insulation layer to next thermal element
R_c	Ω	Electrical resistance of the strand contact points of a cable
R_{cc}	Ω	Resistance of the external coupling circuit
R_{EE}	Ω	Electric resistance of energy extraction system
R_e	Ω	Electrical resistance of elements of a thermal element
$R_{He,b}$	Ω	Electric analogy to insulation layer to helium bath
$R_{if,x}$	Ω	Resistance of inter filament coupling network in x-direction
$R_{if,y}$	Ω	Resistance of inter filament coupling network in x-direction
R_{is}	Ω	Resistance of inter strand coupling network
R_{warm}	Ω	Resistance of the warm parts of the heater circuit
T	K	Temperature
$T_{adiabatic}$	K	Adiabatic hot-spot temperature
T_c	K	Critical temperature
T_{cs}	K	Current sharing temperature
T_{He}	K	Temperature of helium bath
T_{p2}	K	Temperature in point 2
T_{real}	K	Hot-spot temperature including heat transfer
t_{CLIQ}		Switch which triggers CLIQ-system
t_{EE}		Switch which triggers energy extraction system
t_{PC}		Switch which decouples power supply of a magnet circuit
t_{p1}	s	Time until the quench reaches point 1
t_{p2}	s	Time until the quench reaches point 2
t_{QD}	s	Time it takes to detect the quench
t_{QH}	s	Time it takes to trigger the quench heaters
t_{qs}	s	Time when the quench is initiated
t_v	s	Validation time
U_b	V	Electric analogy to the temperature of a thermal element
$U_{Crowbar}$	V	Voltage representing diode of crowbar
U_{diff}	V	Differential voltage between the apertures of MBRD
U_{ground}	V	Voltage to ground
$U_{He,b}$	V	Electric analogy to the temperature of the helium bath
U_h	V	Electric analogy to the temperature of any thermal element
U_{PC}	V	Voltage representing the power supply of a magnet circuit
$U_{TurntoTurn}$	V	Turn to turn voltage
V_{1A}	V	Voltage across coil 1A
V_{1B}	V	Voltage across coil 1B
V_{2A}	V	Voltage across coil 2A
V_{2B}	V	Voltage across coil 2B

V_{b1}	V	Voltage across block 1
V_{b2}	V	Voltage across block 2
V_{b3}	V	Voltage across block 3
V_{b4}	V	Voltage across block 4
V_{b5}	V	Voltage across block 5
v_q^{QH}	$\frac{m}{s}$	Quench propagation velocity between heating stations
v_q	$\frac{m}{s}$	Quench propagation velocity
v_q'	$\frac{m}{s}$	Corrected quench propagation velocity
vq_{BBQ}	$\frac{m}{s}$	Quench propagation velocity calculated by BBQ
$v_{q,corrected}$	$\frac{m}{s}$	Corrected quench propagation velocity
w_{bare}	m	Width of a bare cable
$wetted_p$		Fraction of strand area in direct contact to helium
w_{ins}	m	Thickness of the insulation along the width of a cable

1 Introduction

The LHC[1] located at CERN[2] is a circular accelerator, which accelerates two beams of particles in opposite directions and collides them at four different locations at nearly the speed of light. At this collision points conditions like shortly after the big bang are being reproduced and scientists can thereby extend the knowledge about our universe. To detect particles and radiation, highly specific detectors are placed at these locations. The ATLAS[3] detector is the largest general-physics experiment at CERN and became famous through the ground-breaking discovery of the Higgs-Boson in 2012 [2]. The LHCb[4] experiment records the decay of "B-Mesons" and "Anti-B-Mesons" to understand the asymmetry between matter and antimatter [3]. The CMS[5] detector is specialised in detecting muons but can detect any other physical phenomenon as well, through which it contributed to the discovery of the Higgs-Boson [4]. The ALICE[6] experiment is dedicated to study the quark-gluon-plasma, arising through collisions of lead ions, which are injected into the LHC for parts of the year [5]. To accelerate the beam to the energy which is necessary to inject it into the LHC, an accelerator chain is used as shown in Figure 1.1.

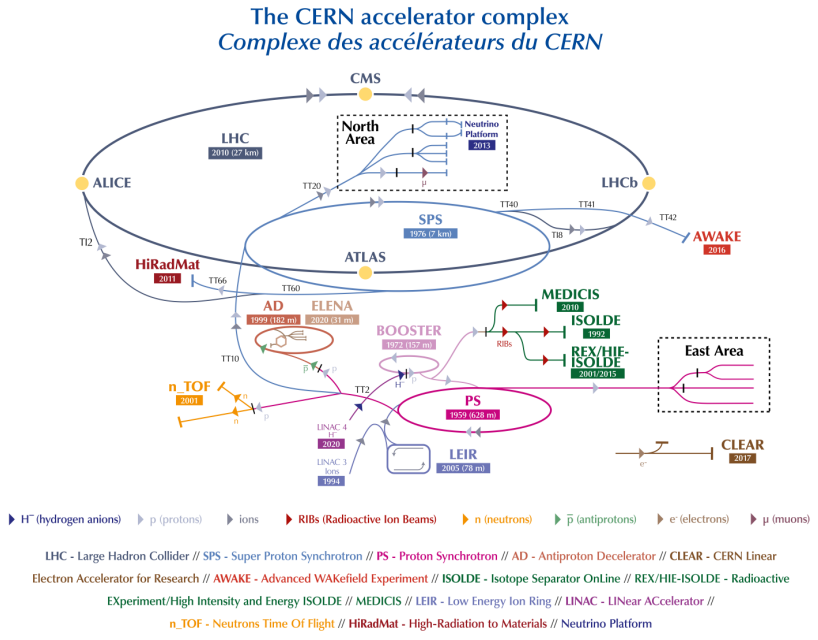

Figure 1.1: Accelerator complex of CERN showing the accelerators chain, various experiments and utilised particles [6].

[1] Large Hadron Collider
[2] Conseil européen pour la recherche nucléaire
[3] A Toroidal LHC-Aparatus
[4] Large Hadron Collider beauty
[5] Compact Muon Solenoid
[6] A Large Ion Collider Experiment

Starting from a proton source the beam goes through a linear accelerator and three circular ones before it is injected into the LHC. Along the chain there are various possibilities to use the beam in other experiments, like ISOLDE[7], ELENA[8] or AWAKE[9], to name just a few. To fill the LHC, a complex chain of smaller accelerators is needed. Several cycles of these accelerators are necessary to completely fill up the machine [6].

1.1 High Luminosity LHC project

Since its completion in 2010, the LHC is the biggest accelerator in size worldwide and surpasses all others in energy levels as well [7]. As shown in Figure 1.2, LHC followed a schedule switching from periods of operation to shut down periods where improvements were implemented and the machine was maintained. Starting from 7 TeV, it reached 13 TeV in its second run from 2015-2018. Simultaneously, the luminosity increased to the ultimate value of $2 \cdot 10^{34} \frac{1}{\text{cm}\cdot\text{s}}$ at the end of run 2 as well. In run 3 from 2022-2025, which got extended lately, there will be an increase of energy to 14 TeV but no change in luminosity, due to heat deposition and lack of cooling in the current configuration which would lead to damage in the machine. First upgrades for the detectors ATLAS and CMS as well as extensive upgrades in LHCb and ALICE were implemented in the resent shut down period. At the end of run 3 various components will come to the end of their lifetime, because of radiation damage.

Figure 1.2: Schedule of the development of the LHC since its completion, including shutdown and active periods. The plan reaches further by showing the research and development periods for the HL-LHC and its introduction in the future [10].

A natural way to further exploit the infrastructure of LHC is to not only replace the components in question, but also to upgrade key elements of the machine to sustain

[7] Isotope Separator Online Device
[8] The Extra Low Energy Antiproton ring
[9] Advanced Proton Driven Plasma Wakefield Acceleration Experiment

scientific progress and reach higher luminosity, through which statistically extremely rare events are more likely and in general more precise measurements are possible [8], [10]. The HL[10]-LHC project will increase the luminosity to $7.5 \cdot 10^{34}$ $\frac{1}{\text{cm} \cdot \text{s}}$, hence reaching an integrated luminosity up to 4000 $\frac{1}{\text{fb}}$ in the 12 years foreseen of operation. This value is 10 times higher than what was reached in the lifetime of the old LHC machine [8]. To make the HL-LHC upgrade possible, various changes to the machine are necessary. The components of the inner triplet regions close to the interaction points of the beam need to be replaced. The inner triplets consist of several quadrupole magnets, various high order corrector magnets, a separation and a recombination dipole magnet. To shield the quadrupole triplet magnets from collision debris, hence reducing the heat load and radiation damage the aperture has to be increased and a tungsten shielding has to be implemented. Some of the high order corrector magnets may not withstand the received dose of 30 MGy and therefore must be replaced. To recover additional space required by the triplets and the correctors and to insert the additional components needed for the HL-LHC upgrade, the length of the separation and recombination dipole magnets has to be reduced. At the same time the magnetic field has to be increased to preserve the same magnetic rigidity $\vec{B} \times \vec{l}$. This is done by redesigning the recombination dipole magnet and replacing the normal conducting separation dipole magnet with a superconducting one. Other areas which are effected by the upgrade are parts of the cryogenics, the collimation system, the focusing regions at ATLAS and CMS where new $11 - 12$ T quadrupole magnets are introduced and superconducting links to the newly installed power electronics will be implemented [8], [9]. Another important novelty to the HL-LHC are the crab cavities, which enlarge the overlap of the proton bunches before collision by tilting the beam on either side of ATLAS and CMS [9].

1.2 Superconducting magnets

1.2.1 Superconductivity

Superconductivity describes a state of no electric resistivity of a material under certain circumstances. It was first observed by Heike Kamerlingh Onnes in 1911, as he carried out experiments with mercury at low temperatures. He described a sudden drop in the resistivity of mercury from 0.1 Ω to below the measurement accuracy at the temperature of 4.1 K. Since then various elements were found superconducting at low temperature, high pressure or in special forms, like nanotubes or thin films. Additional to the phenomenon of no resistivity, one can observe the exclusion of the magnetic field from the inside of a superconductor. The so called Meissner effect can not be explained by applying Maxwell's equations but with screening currents at the surface of the conductor which produce a field opposite to the external one, hence extinguishing any field inside the conductor. As there is no magnetic field existent inside a superconductor and Ampere's law indicates $\nabla \times B = \mu_0 J$, one can conclude that the current only flows in a thin layer at the surface of the conductor.

[10] High Luminosity

This leads to high field and current density in the mentioned layer. Screening currents will sum up with the currents circulating in the superconductor, resulting in even higher current density. For the field, the same calculation can be done by adding the field produced by the current flowing in the direction of the conductor and external fields [11].

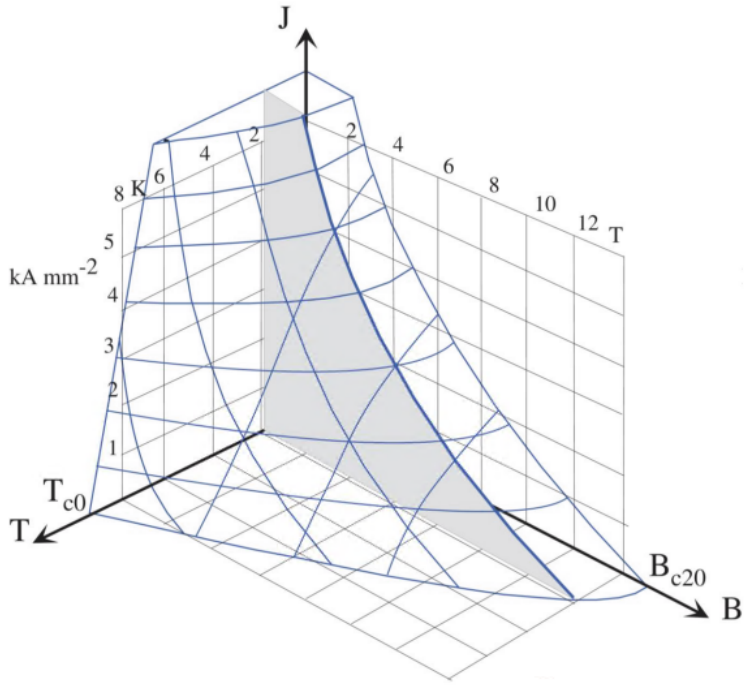

Figure 1.3: Critical surface of a superconductor where it transitions into the normal state, in respect to the temperature, magnetic field and current density [12].

Figure 1.3 shows the dependence of the state of superconductivity on three physical parameters T, B and J. When increasing the magnetic field while keeping the current and the temperature constant, the conductor gets resistive at a distinctive field, called the critical field B_c. The same accounts for the temperature and the current when reaching T_c or J_c. Thereby, a unique critical surface for each superconductor can be created, outside of which it always transitions into the so called normal state [12].
There are two main types of superconducting materials type-I and type-II superconductors. Most of the elemental superconductors belong to type-I, which are described by the critical surface shown above. The behaviour of cylindrical shaped type-I superconductor samples when an external magnetic field smaller than B_c is applied parallel to their axis is shown in Figure 1.4 a) at the top. An exclusion of the magnetic field from the conductor can be observed. When a perpendicular magnetic field smaller than B_c is applied instead one can observe field concentration in the outer layer of the conductor due to field distortion. For cylindrical shapes, the field reaches twice the value of the applied field in these regions. As the external field doesn't exceed B_c the conductor can't fully transition into the normal state. Thus only slices of the cylinder, where B_c is exceeded, are building up electric resistivity and in those regions the external field can penetrate as shown in Figure 1.4 a) at the bottom. Depending on the geometry of the superconductor and the direction of the external field, the point

where resistive regions develop is different. Only in the case of a thin cylinder with a parallel external field, the whole conductor transitions into the normal state at B_c.

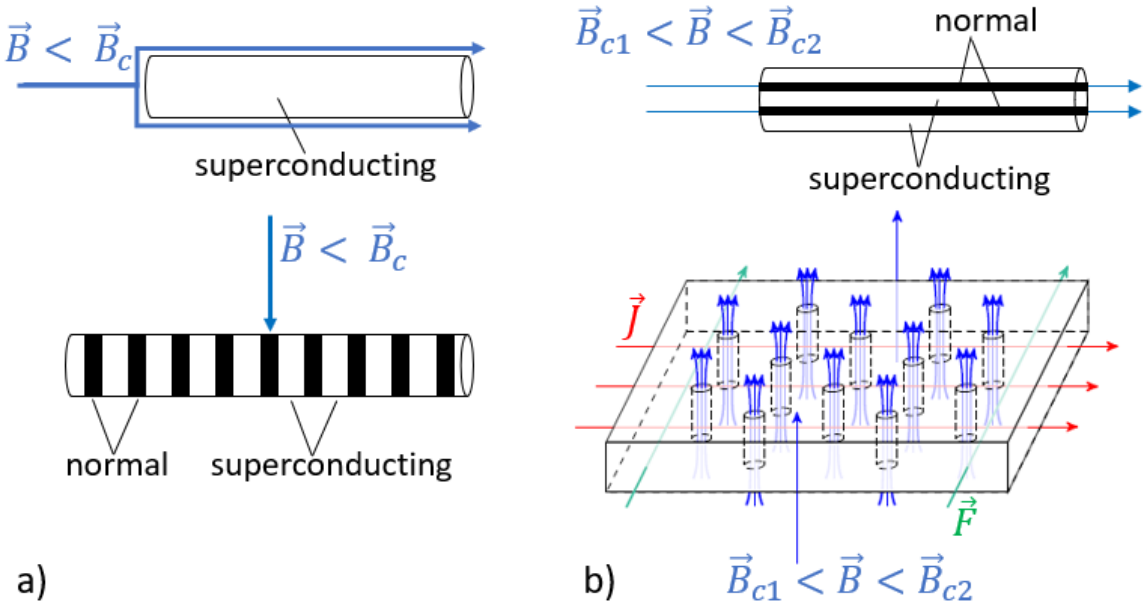

Figure 1.4: a) Shows the behaviour of a type-I superconductor when an external magnetic field below B_c is applied parallel or perpendicular to the conductor current.
b) Pictures a type-II superconductor for the case of an external applied magnetic field between B_{c1} and B_{c2} perpendicular and parallel to the conductor current [13].

For type-II superconductors the transition into the normal state is split into two phases. When applying an external field parallel to a cylinder below a certain strength B_{c1}, it behaves like a type-I superconductor under the same conditions. When exceeding B_{c1}, several cylindrical regions, so called normal cores, along its axis transition into the normal state, as shown in Figure 1.4 b) at the top. When increasing the field, the resistive regions get more and more packed and when the upper limit B_{c2} is reached the whole conductor transitions into the normal state. In the intermediate phase, the external field goes through the cylindrical regions, hence penetrates the conductor in several spots evenly distributed across the cross section of the conductor. Type-II superconductor behave in the case of a perpendicular applied magnetic field the same way as in case of a parallel applied magnetic field. Again evenly distributed normal cores emerge and the external field can pass through them. As shown in Figure 1.4 b) at the bottom the normal cores experience a force perpendicular to the field and to the direction of the current, as will be described more in detail in Superconductors in applications [11],[14].
So far superconductivity was considered to be a property of certain materials. On a quantum mechanical basis, superconductivity can be explained with the existence of cooper pairs included in the BCS-Theory. At low temperature, the thermal oscillation of the the crystal lattice of the superconductor gets negligible. In this state an electron in the lattice attracts the nuclei surrounding it. Another electron can get attracted to the area of deformation in the lattice, hence forming a cooper pair with the first

electron. The electrons in the pair always have opposing momentum and spin. The electron pair is no longer a fermion, as a single electron would be, but a boson, hence it can be seen as a single particle. The connecting force of a cooper pair is really week and can be broken by small thermal disturbances, therefore superconductivity mostly exists at low temperature. As cooper pairs are active over high distances all these connections are overlapping and are forming a large network which leads to no excitation of the lattice trough collisions of the electrons with the nuclei. Having no excitation of the crystal lattice of the conductor leads to no electrical resistance in the material. The cooper pairs in a conductor all have the same physical properties and the same movement of their center of gravity, thus forming a material wave which leads to the macroscopic behaviour of superconductors. The validity of the BCS-Theory is limited to type-I superconductors, while the explanation of the superconducting state in type-II superconductors is still not fully understood and part of scientific research [14].

1.2.2 Superconductors in applications

To use superconductors in applications several adjustments have to be considered. The high values of the upper critical field B_{c2} of type-II superconductors make them very attractive for winding coils and producing high magnetic fields. The electrons in the normal cores of type-II superconductors at high external fields experience a Lorentz force equal to $\vec{F} = q(\vec{l} \times \vec{B})$. Where $\vec{F}$ stands for the force on the electrons, q is the charge, $\vec{l}$ the direction of the current in the conductor and $\vec{B}$ the magnetic flux density in the the normal cores. Through the force on the electrons, the normal cores start to move as well as their associated magnetic flux, which leads to an eddy current inside the resistive parts of the conductor. Through the energy dissipated in the normal cores more and more parts of the conductor transition into the normal state until the superconducting state collapses. To mitigate the movement of the normal cores, defects are introduced in the conductor, which form a barrier against this movement. Superconductors used in applications always include intentionally placed impurities out of crystalline grains with different orientations to pin the normal cores [11].
The two main superconductors used in applications today are Nb-Ti[11] and Nb_3Sn[12]. Nb-Ti has a critical temperature of 9.6 K and a critical field of 14 T at 2 K and through thermo-mechanical treatment it is possible to introduce pinning centers. These pinning centers can be distributed similarly to the natural distribution of the normal cores, which improves the effect even further. Nb_3Sn has a critical temperature of 18 K and a critical field of 25 T at 4.2 K depending on the chemistry and microstructure. In the case of Nb_3Sn the pinning centers are the grain boundaries of the used materials, meaning a fine grained microstructure should be used [11].

[11] Niobium-titanium
[12] Niobium3-Tin

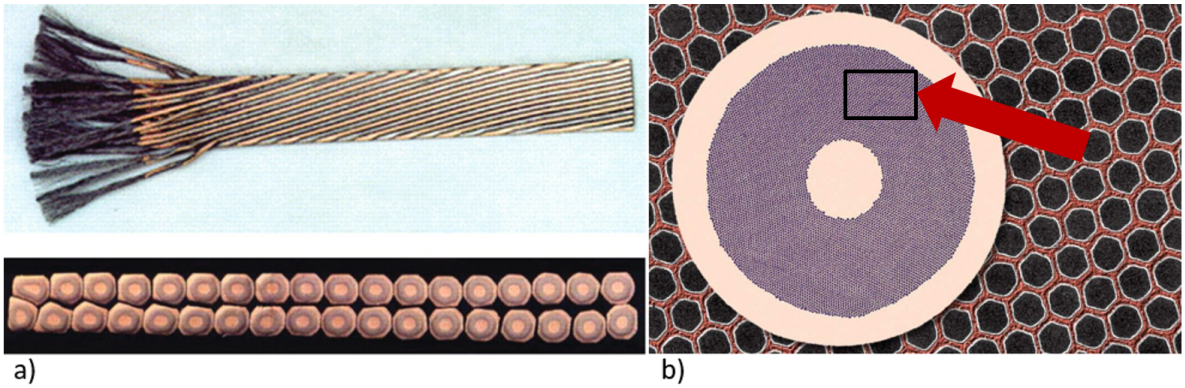

Figure 1.5: a) Top-view and cross-section of a Rutherford cable [15], b) Cross-section of a superconducting strand made of Nb-Ti filaments in black and copper in orange is shown in the foreground. The strand consists of a cooper core, copper coating and Nb-Ti filaments in a copper matrix. In the background a magnified illustration of the superconducting filaments (black) in a copper matrix are shown [16].

Superconducting cables consist mostly of superconducting filaments embedded in a normal conductor like copper, shown in Figure 1.5 b) in the background. The stabiliser acts as low resistivity path when the superconductor is in the normal state and as heat sink when the cable is superconducting to ensure constant temperatures as the stabilizer usually has a high thermal conductivity. Many filaments form a strand with a stabiliser core and coating shown in the foreground of Figure 1.5 b). The filaments in the strands are usually twisted to mitigate the impact of coupling currents in the superconductor. In the case of a strand they are called inter-filament coupling current (IFCC[13]) and occur due to field change which induces currents between filaments forming open loops. To finally form a cable and reach higher transport currents, tens of strands are put together, mostly in two layers as seen in Figure 1.5 a) at the bottom. The strands are then wound in a complex way to form a cable, e.g. a Rutherford cable like in Figure 1.5 a) at the top. The strands are wound in a way so that their relative position changes continuously along the length to achieve uniform current density in the cable. Furthermore the twist of the strands weakens the development of coupling currents, in this case inter-strand coupling currents (ISCC[14]). ISCC develop between strand contact points due to currents induced into open loops. Usually Rutherford cables are used in accelerator magnets, because of their good stack ability and high packing value [17],[18]. Superconducting cables can be wound to coils and then be used in medical applications, particle accelerators, detectors and other machines which need high magnetic fields. The obtained fields in superconducting magnets depends on the chosen geometry and coil layout. In high-energy physics, large scale machines composed of various superconducting magnets are used to study the interaction of particles. Synchrotron accelerators rely on multipole magnets to keep a particle beam on a circular track, collide the particles at specific interaction points and study the particle interactions with sophisticated detectors. The size of the accelerator depends on the energy of the particles and on the bending strength of the magnets to keep the beam on a circular

[13] Inter-filament coupling currents
[14] Inter-starnd coupling currents

track. Thus it is of high interest to achieve high magnetic fields which can only be achieved by superconducting magnets given the limited space of the underground areas where particle accelerators are usually placed [18]. At the same time it is energetically sensible to use superconducting magnets for high-energy physics as it would consume 22 times more energy to achieve the same particle energy in a accelerator with normal conducting magnets, which additionally would have a circumference of about 100 km compared to 27 km [19].
To reach high fields in superconducting accelerator magnets many cables have to be stacked. To achieve the desired field different layouts exist. Dipole magnets are used to bend the beam to keep it on the circular track of the accelerator. Quadrupole magnets are needed to compress and decompress the beam. To correct the non ideal behaviour of the mentioned magnets high-order multipole magnets are used [18].

1.2.3 Quench

To insure continuous operation of a superconducting magnet, all its current carrying parts have to full fill all criteria to superconduct. Sometimes it can happen that in a specific point in the magnet a small part of the conductor transitions into the normal state, this process is called quench. A quench can happen, because of unwanted movements of a cable due to Lorentz force, flux jumps, AC losses or heat leaks. The copper matrix around the quenched spot in the superconductor can take some of the heat from the hot-spot, but starts to conduct at the current sharing temperature (T_{cs}). The current in the cable gets redistributed, which is called the current sharing regime, and through the normal conduction of the copper more energy is dissipated in the area of the hot-spot [20]. Usually, accelerator magnets operate in a helium bath which is constant at a temperature level of either 4.2 K or 1.9 K in the case of LHC and HL-LHC respectively and acts as additional cooling of a quench hot-spot.

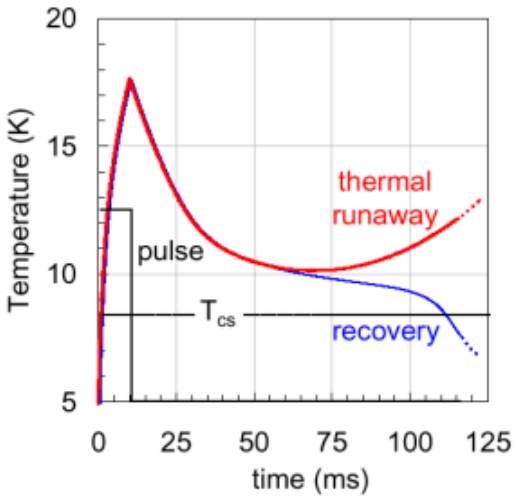

Figure 1.6: Qualitative comparison of temperature development in a quench hot-spot, initiated by a temperature pulse, just above and below the stability energy margin leading to either a thermal runaway or recovery by drooping below T_{cs} [20].

As helium at 1.9 K is in the super-fluid state (also called He II), it can penetrate a superconducting cable and fill even the smallest gaps. This phenomenon leads to even more cooling of a quench hot-spot as super-fluid helium has a very high thermal conductivity as well [21].
When the cooling of the hot-spot is not sufficient to restore superconductivity, the temperature of the spot increases and the quench propagates across the magnet, leading to the discharge of the whole magnet. Qualitatively this is illustrated by the red curve in Figure 1.6. This gets amplified by the fact that most materials have a very low heat capacity at low temperatures. If the quench energy is below a certain margin the cooling will be sufficient to recover the hot-spot and restore superconductivity in the whole magnet, as shown by the blue curve in Figure 1.6.
As superconducting magnets are operating at high fields and can store a lot of energy, the potential risk of damaging the magnet through overheating is quite high. If the heat which develops in the normal spot is not properly dissipated various damages can occur:

- The hot-spot temperature increases to a point where the insulation or even the conductor itself can be damaged.
- The thermal gradient between different regions can induce high mechanical stress, potentially leading to structural failure.
- High voltages between the coil and ground due to inhomogeneous transition into the normal state can lead to short circuits.
- Pressure increase due to evaporation of helium can again lead to structural damage.

As a quench happens, parts or all of the stored energy in the magnet gets transferred into heat deposited into the coil. The front of the developing quench is also called the normal zone, which travels through the coil with a certain velocity. It has to be distinguished between transversal propagation and longitudinal propagation of the quench. The transversal propagation from turn to turn and between layers of the coil are highly dependant on the insulation thickness of the cables. The longitudinal propagation v_q, however, is dependant on different conditions in the cable as shown in Equation 1.1 [22],[23]:

$$v_q = \frac{J}{\bar{c}} \left(\frac{p\kappa}{\frac{T_{cs}}{2} + \frac{T_c}{2} - T} \right)^{1/2} \tag{1.1}$$

J stands for the current density in the insulated cable, p represents its perimeter, κ its thermal conductivity, $\bar{c}$ is the volumetric heat capacity and T_{cs} and T_c the current sharing and critical temperature. Typical v_q at nominal current of the LHC magnets lie between 20 and 30 $\frac{\mathrm{m}}{\mathrm{s}}$ [24]. As v_q is linear dependant on J it follows that the lower the current the slower the quench propagates. This leads to a slower discharge of the magnet and can lead to recovery of the magnet even though the quench propagated already up to a certain point.

1.3 Quench protection of superconducting magnets

When a quench occurs, it has to be assured that the hot-spot of the magnet stays below a defined temperature at the end of the discharge. Giving an example, one can use 1 of the 8 LHC main dipole circuits with 154 magnets, an inductivity of 0.1 H for each magnet and an operating current of 11.85 kA [25]. The energy stored in the accelerator chain can be approximated as following:

$$E = \frac{n \cdot L \cdot I^2}{2} = \frac{154 \cdot 0.1\ \mathrm{H} \cdot (11.85\ \mathrm{kA})^2}{2} = 1.08\ \mathrm{GJ} \tag{1.2}$$

Dissipating this amount of energy in a limited region of a magnet can give very high hot-spot temperatures. An acceptable range for most superconducting magnets goes up to 300 K, which would be exceeded by far with the given example [21].
To guarantee the re-usability of the magnet, different precautions can be carried out. Some magnet layouts are self-protecting, hence the cooling effect of the stabilizing conductor in the cable and the helium is enough to prevent damage inside the magnet, as shown in Figure 1.7 a. This protection scheme is the fastest and most reliable, as there is no external system which needs to get triggered and could fail.

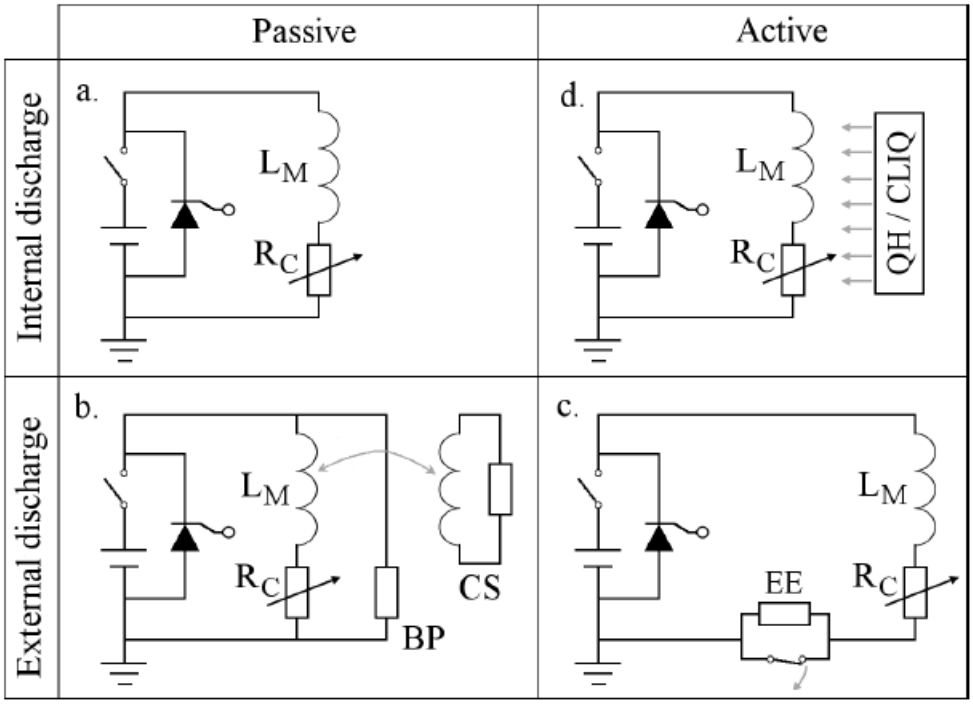

Figure 1.7: Different protection schemes of a superconducting magnet divided into internal or external discharges and passive or active protection systems. The power supply of the magnet consists of a voltage source a switch and a parallel diode. The magnet consists of a inductance (L_M) and a variable resistance (R_C); a. Self-protected magnet, b. By-passed (BP) magnet with coupled secondary coil (CS) c. Magnet protection with energy extraction (EE), d. External heating by CLIQ or QH [18].

If a magnet is not self-protecting there are three main options to protect it. Figure 1.7 b. shows an external protection system consisting of by-pass elements, which can be diodes, resistors or a combination of the two. When a quench occurs in the magnet and a resistance develops, parts of the current are forced through the by-pass. Thus, depending on the installed elements, a portion of the magnet energy is dissipated externally. An advantage of this system is that there is no need of a quench detection system as its protection is triggered by the quench itself. On the downside, this system is relatively slow and when ramping the magnet up or down leakage currents are always induced into the by-pass circuit and lead to unnecessary losses. Another external protection system consisting of an energy-extraction, which needs a detection of the quench, is shown in Figure 1.7 c. When a quench is detected a switch opens and the current gets forced through a resistor in series to the magnet. Depending on the size of the resistor more or less energy dissipates in it. With a well designed detection and triggering system this protection scheme is fast, but is heavily relying on the detection of the quench. The same accounts for the protection shown in Figure 1.7 d, which relies on active heating of the coil. When a quench is detected, a heat source gets triggered and distributes the heat input evenly across the magnet. By doing so not only the hot-spot quenches but bigger parts of the magnet and therefore the energy gets dissipated in a bigger volume. The heat source can be implemented in two different ways, one is a CLIQ-system which induces magnetic field oscillations into the main coil. This leads to high coupling currents, which furthermore lead to heating and quenching of notable parts of the coil. The second system consists of heating stations, also called quench heaters (QH), which are physically connected to the coil and heat up the conductor below the stations. Through heat diffusion, other parts of the coil heat up, hence quench. Through both active internal heating systems, a more uniform voltage and transition into the normal state of the whole magnet can be insured. Magnets with high field and stored energy are usually protected by QHs, but protection with CLIQ-systems are also possible [18].

1.4 Quench heaters

As described in the previous section, QHs consist of several heating stations which are glued to the surface of the coil and are evenly distributed across the magnet. QHs consist of stainless steel strips, which are copper plated in a specific pattern to form actual heating stations. The heating stations are a few tens of micrometers thick and glued into insulation foil. They are then fixed onto the insulation of the magnet coil. As shown in Figure 1.11 for the main dipole of LHC the QH strips are glued to the outside of the coil and are distributed in a way to insure the magnets safety [26]. Depending on the design, the QH strips are arranged in series or in parallel and connected to capacitor banks. When a quench is detected, the capacitor banks discharge into the QH circuit, which leads to ohmic loss in the stainless steel parts and through heat diffusion to heating of parts of the coil. The parts of the coil below the heating stations quench first and the normal zone of the quench will develop from there [18]. The thickness of the insulation of the heating stations and the coil is crucial to the protection of the magnet. A good compromise between a fast enough heat diffusion, which requires a

thin insulation, and a sufficient electrical robustness, which requires a thick insulation, must be found [27].

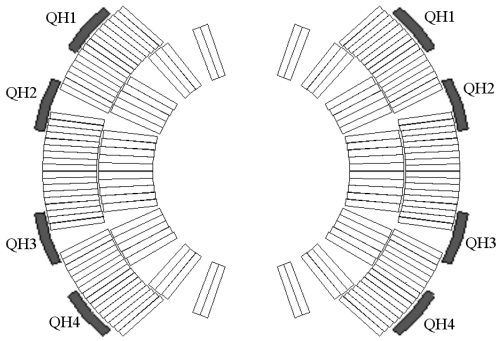

Figure 1.8: Cross section of one aperture of the LHC main dipole with 4 QH circuits. The QH strips are glued to the outside layer of the magnet coil [18].

The simplified characteristic of a QH based quench protection can be split into three phases. The first is given by the time until the quench is detected t_{QD}, the validation time t_v and the time it takes to trigger the protection t_{QH}. In this time period, the current in the magnet stays approximately constant, neglecting the effect of the developing resistivity in the hot-spot. The next phase is depending on the effectiveness of the protection system and the normal zone propagation in the magnet. Again it can be approximated that the current stays constant and the effects of transient losses through the discharge can be neglected. The last phase depends on the magnet characteristics like coil geometry, conductor properties and other used materials. This phase describes the actual discharge of the magnet as the current decreases rapidly and coupling currents, developing resistivity and normal zone propagation have to be taken into account.
Nb-Ti accelerator magnets have a time margin (i.e. the time in which the whole magnet must be quenched) of $50 - 200$ ms [31], while Nb_3Sn coils should be quenched in $10 - 50$ ms [31]. The QH delay represents the time until a normal zone develops after the QHs are triggered. Measured values for the QH delay lie at $10 - 30$ ms for Nb_3Sn magnets for the HL-LHC [28]. However, the QH delay only refers to the development of a normal zone near a heating stations and the time margin corresponds to the full discharge of the magnet. Taking this into account it is obvious that it is crucial to understand the development of the quench throughout the magnet and to potentially implement more advanced protection systems. This can for example be done by implementing QH strips in between coil layers. These systems can quench the magnet significantly faster, but are more complex to maintain as the inner QH strips are difficult to reach. Protection schemes based on CLIQ are also able to improve the protection and insure the safety also for Nb_3Sn magnets [18].
QH heating stations are not touching the whole length of a coil turn but only certain spots along the direction of the conductor. Taking this into account, the quench propagation velocity between the heating stations in the direction of the conductor, between adjacent turns and possibly from an outer to an inner coil-layer are important to understand. To calculate the quench propagation velocity in the direction of the conductor between heating stations, the following formula can be used [29]:

$$v_q^{QH} = 2 \cdot n_{QH,stations} \cdot v_q \tag{1.3}$$

v_q^{QH} giving the propagation velocity between heating stations, $n_{QH,stations}$ being the number of heating stations in one heater strip and v_q representing the adiabatic quench propagation velocity. The factor 2 used is due to the normal zone propagating in both directions along the magnet starting from a heating station. Figure 1.9 qualitatively shows the temperature profile in a coil turn touched by a QH. A quench hot-spot is developing in the part of the coil turn touched by a heating station and from there the normal zone propagates in both directions, represented by the developing temperature from dark purple to light green.

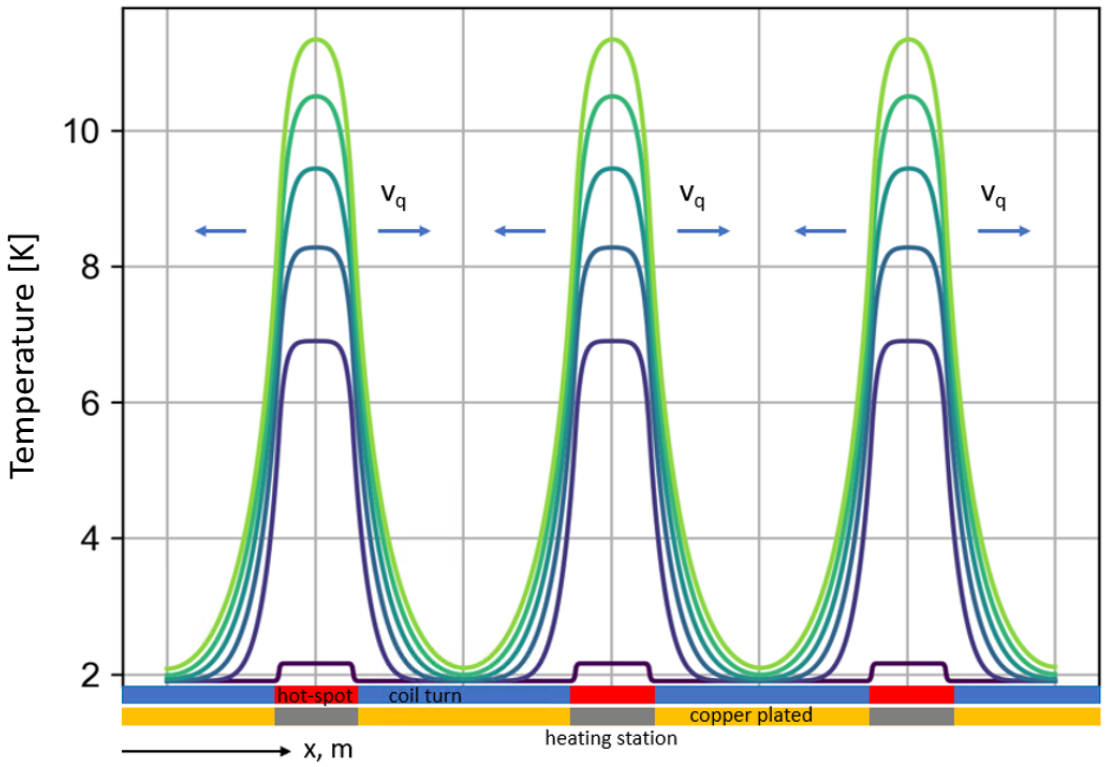

Figure 1.9: Qualitative temperature profile in between QH heating stations, obtained with PyBBQ [30], after the QH is fired. In yellow the copper plated parts and in grey the heating station of the QH are shown. The superconducting parts of a coil turn touched by the QH is illustrated in blue, whereas the quenched parts of the coil turn in contact to the heating stations are shown in red. The quench is propagating in both directions starting from the hot-spot in contact to a heating station shown for different times forming a developing temperature profile from dark purple to light green.

The time to quench a full coil turn in contact to a QH, as shown in Figure 1.9, using Equation 1.3, assuming 20 $\frac{\text{m}}{\text{s}}$ as v_q and a length of 40 mm for the copper plated parts between heating stations, is 8.5 ms. The heat diffusion through the insulation in between turns takes about 10 ms per turn [31]. Another $30 - 50$ ms have to be taken

into account for magnets with multiple coil-layers for the heat diffusion between them [32]. That means that the best case scenario for magnets with multiple coil-layers and a high coverage of QHs is that it takes approximately 60 ms to quench the whole magnet, starting from the triggering of the heaters. When including t_{QD}, t_v and t_{QH} the time from the quench start to the transition of the whole magnet will reach values above 60 ms, which is low enough to protect most magnets safely considering the time margin for Nb-Ti magnets but is above the highest margin for Nb_3Sn magnets.
Considering the dependence of v_q on the current, higher discharge times of the magnet can be reached at lower currents. In fact, the example above was given for nominal current, but lower currents have to be taken into account too to assess the safety of the magnet. Indeed, already at half of the nominal current, v_q decreased considerably and will lead to even more critical discharge times.

1.5 Recombination dipole magnet

The recombination dipole magnet MBRD for the HL-LHC upgrade will be placed near the interaction regions of ATLAS and CMS and will replace the old recombination dipole (MBRC) of the LHC [8]. The replacement is necessary due to the reduction of space between MBRD and the separation dipole magnet MBXF. There are also other space constraints due to protection devices and the crab cavities. The double aperture MBRD dipole deflects the two beams in order to make them recombined before entering the single aperture MBXF dipole. Between MBXF and the interaction point the beams are getting further squeezed and corrected by various high order correctors and quardupoles [8].

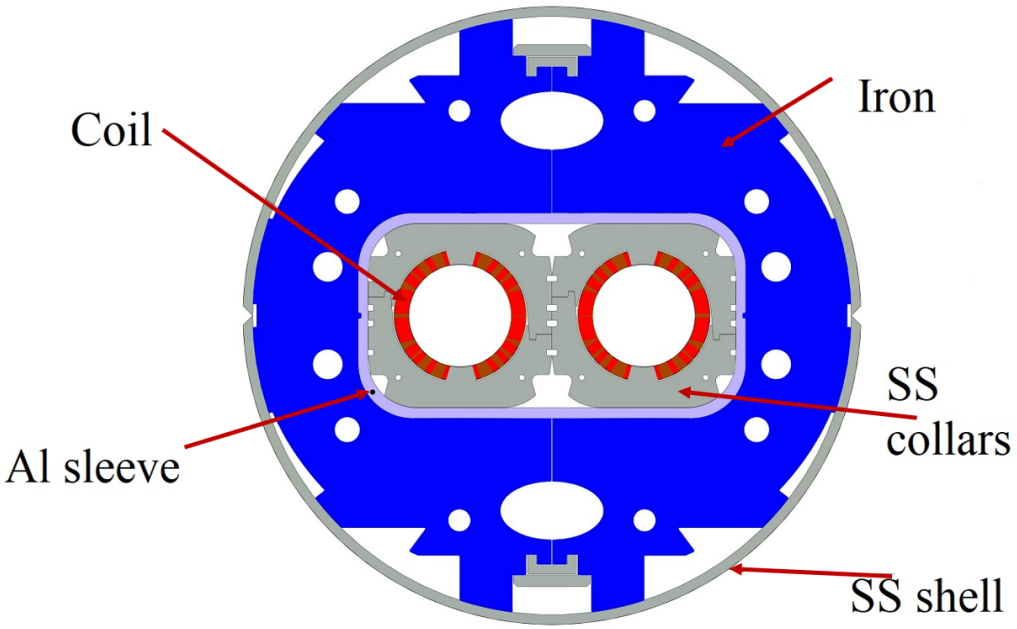

Figure 1.10: Cross-section of the MBRD magnet including both apertures and coils (red), iron yoke (blue), stainless steel collars (grey), aluminum rings (violet) to support the structure and stainless steel shell (grey) [35].

As the main task of MBRD is the recombination of the beams its field lines have the same direction in both apertures, causing high cross-talk between them. This is mitigated through an asymmetry of the two apertures, by slightly tilting the coil blocks in each pole as one can see in Figure 1.11. Furthermore, having the two apertures with the same polarity induce repulsive Lorentz forces between them when the magnet is energized. To support the structure of the magnet, aluminium rings are implemented around both individually collared apertures [33]. Aluminium has a larger thermal contraction as the apertures, so at cryogenic temperatures the rings shrink more than the collared aperture, helping to compensate the Lorentz forces and keep the structure in place [34]. Surrounding the aluminium rings the, iron yoke including the heat extraction and the final shell of the accelerator are placed. The layout of MBRD is shown in Figure 1.10 including the coils, stainless steel collars, aluminium rings, surrounding iron yoke and accelerator shell [35].
Each aperture of MBRD is composed of two single layer coils consisting of 31 turns. The turns are arranged in 5 blocks of which the nearest to the mid plane has 15, the next 6, the two following 4 each and the last 2 turns. The same Rutherford cable as in the outer layer of the LHC main dipole is used here to reduce the risks which can occur when implementing a new cable [8],[33].
MBRD is operating at a bore magnetic field of 4.5 T and a peak field of 5.28 T. The lower field values compared to MBXF (peak field: 5.6 T) although having the same cable and similar current are due to losses created through cross-talk and less impact of the iron [34]. The magnet has a magnetic length of 7.78 m and an actual length of 8.5 m. The nominal current I_{nom} and ultimate current I_{ult} are 12340 A and 13357 A, respectively. The stored energy at I_{nom} totals 2.28 MJ. The operating temperature lies at 1.9 K and is provided by a static bath of He II. The key design figures of MBRD are summarized in Table 1.1 [33].

Key design features of the MBRD magnet

Design feature	**Unit**	**Value**
Bore magnetic field / Peak magnetic field	T	4.5 / 5.28
I_{nom} / I_{ult}	A	12340 / 13357
Stored energy at I_{nom}	MJ	2.2
Magnetic length / Aperture length	m	7.78 / 8.5
Number of blocks		5
Number of turns per coil		31

Table 1.1: Summary of key figures of the MBRD magnet

As protection for the MBRD magnet QHs are chosen over an energy extraction, for cost reasons [35]. 8 QHs are placed on the outside of the coils with 16 strips in total, two per each half-coil. Figure 1.11 shows the QH setup, naming and placement of the strips. As the magnet is not symmetric, the QH strips are touching different turns depending on the pole they are glued on. The blue strips in Figure 1.11 are touching the same amount and pattern of turns of block 1, counting from the midplane, for each pole. For the red strips that is not true anymore, as there is a difference in the distance between block two and three depending on the pole.

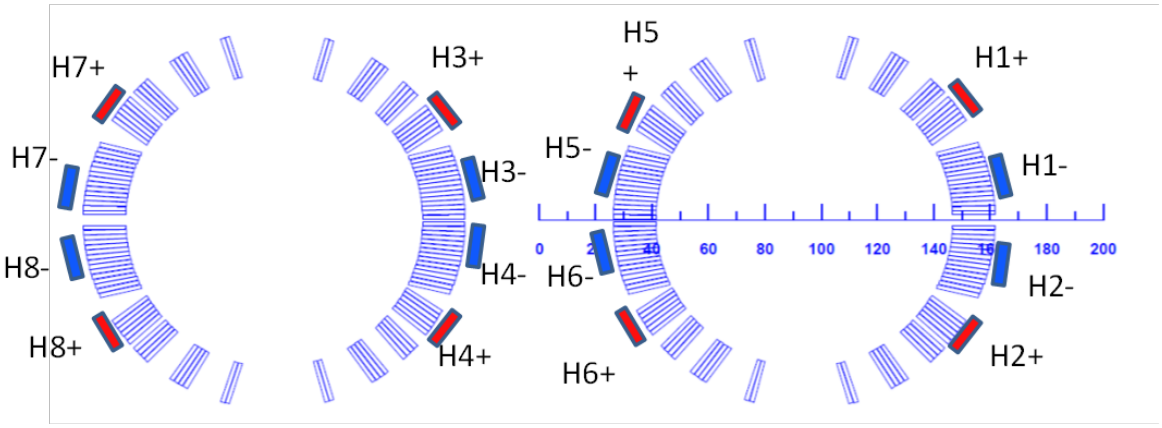

Figure 1.11: Quench protection scheme of the MBRD magnet including positive and negative leads of the QH strips shown for both apertures [36].

It is important to note that all heating strips shown in blue are only in contact to one block of the magnet, but the heater strips in red are touching two. This design feature is very important to take note of as the quench propagation from one block to another is relatively slow as there is extra insulation and a copper wedge between the blocks. Insuring the heat input into a block with a QH can be crucial for the protection of the magnet. In the case of MBRD, the protection scheme also relies on coupling loss to induce enough energy into the two blocks further away from the midplane to quench the turns fast enough to prevent damage. Also the protection baseline does not include all QH but half of them. In the original protection scheme only QH 1, 3, 6 and 8 should be triggered and the rest would be left as spares in case of damage of another heater during operation.
INFN[15]-Genoa is in charge of the design, engineering and construction of the MBRD magnet and assigned the manufacturing to ASG Superconductors (Italy). The cooperation includes one short-model, one prototype and six series magnets of which two are left as spares. At CERN, extensive tests had been carried out with the short-model which were partly accompanied by quench simulations from my side. This thesis will focus on the modelling of quench behaviour of the MBRD magnet using mainly two in-house simulation tools in a consecutive simulation to enhance the ability to model longitudinal quench propagation. The model will be validated and discussed using the performed measurements. Furthermore, improvements to the automated setup for a simulation of various superconducting magnets will be implemented and the results will be shown.

[15] National Institute for Nuclear Physics

2 Modelling of transients in superconducting magnets

Modeling superconducting magnets is a challenging task. The models need to be accurate in different physical domains as well as in various time- and spacial scales. Usually finite-element or finite-difference modeling is used to tackle such problems. But either of them can require high computational effort, hence become inefficient and time consuming.

2.1 STEAM-Framework

The STEAM[1]-Framework tries to "achieve specialized, trusted, consistent, repeatable and sustainable software tools and models for rapid Simulation of Transient Effects in Accelerator superconducting Magnet circuits" [39]. It consists of different tools, which are developed to simulate transients or phenomena in different scopes of a superconducting magnet circuit. These tools and models are validated and maintained by the STEAM-Team at CERN. Furthermore, they are also open to the community and available to be customized for specific user cases, which helps to continuously improve the framework.

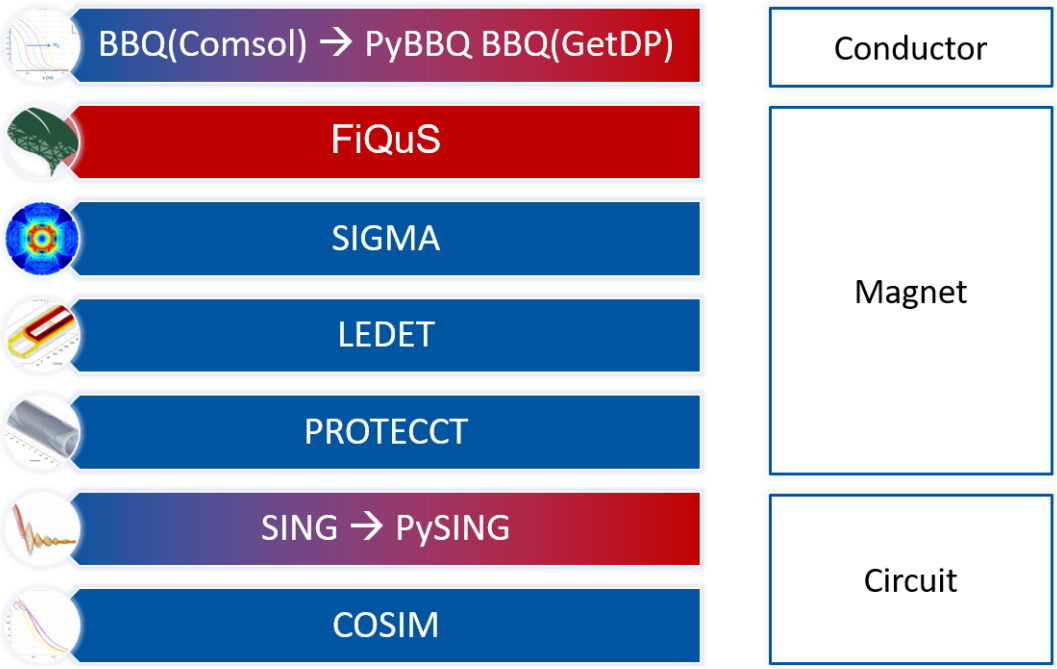

Figure 2.1: Overview of the tools of the STEAM-Framework and the domains in which they are mainly used currently (2022) [39].

[1] Simulation of Transient Effects in Accelerator Magnets

The simulation tools allow simulating transients in three different level of detail: Conductor, Magnet and Circuit, as summarized in Figure 2.1. BBQ[2] [40] is used for simulating quench propagation in superconducting busbars. It is based on COMSOL and follows a 1D+1D modeling approach by considering heat flow along the conductor and through the insulation at certain nodes. At the moment it is considered to complement it with a new tool written in Python, named PyBBQ[3] [30] to improve compatibility with other tools. FiQuS[4] [41] is under development as well and will be able to perform finite-element calculations for various transients in superconducting magnets. SIGMA[5] [42] is used to generate 2D finite-element COMSOL models to simulate electro-magnetic and thermal transients in superconducting magnets. LEDET[6] [43], [40] models electro-magnetic and thermal transients in a 2D and 3D [45] geometry in superconducting magnets based on the finite-difference method using Matlab. ProteCCT[7] [46] simulates electro-magnetic and thermal transients in CCT[8] magnets, based on the finite-difference method using Matlab. SING[9] [47] automatically generates PSPICE and LTSPICE circuit models relying on shared sub-components which is now done in Python. COSIM[10] [48] is used to run co-operative simulations developed in different programs.

2.2 Lumped element modelling

In order to describe and simulate complex physical problems they are usually broken down into manageable parts. The commonly known finite-element method can be used for discretization of domains into a finite number of elements. This method can be inefficient for non-linear behaviour in superconducting magnets with a high number of turns due to high computational effort. Alternatively the finite-difference method can be introduced partially using a network of non-linear lumped-elements to simplify the physical problem. This network consists of discrete chunks to which one can apply approximate physical behaviour in form of physical assumptions. Various sub-systems can be combined into a single system under certain assumptions. Thus the state-space model of the global system, meaning the time domain and the space model, is transformed into ordinary differential equations with a low number of parameters. Lumped-element modeling is always an approximation of the physical system, while the level of accuracy can be defined by the amount of lumped-elements. If the behaviour of interest is not yet sufficiently captured, the physical problem can be broken down into smaller parts until it fits satisfactorily [49].

[2] Bus Bar Quench
[3] Python based Bus Bar Quench
[4] Finite Elements Quench Simulator
[5] STEAM Integrated Generator of Magnets for Accelerators
[6] Lumped-Element Dynamic Electro-Thermal
[7] Protection of Canted Cosine Theta
[8] Canted Cosine Theta
[9] STEAM Integrated Network Generator
[10] Co-operative Simulation

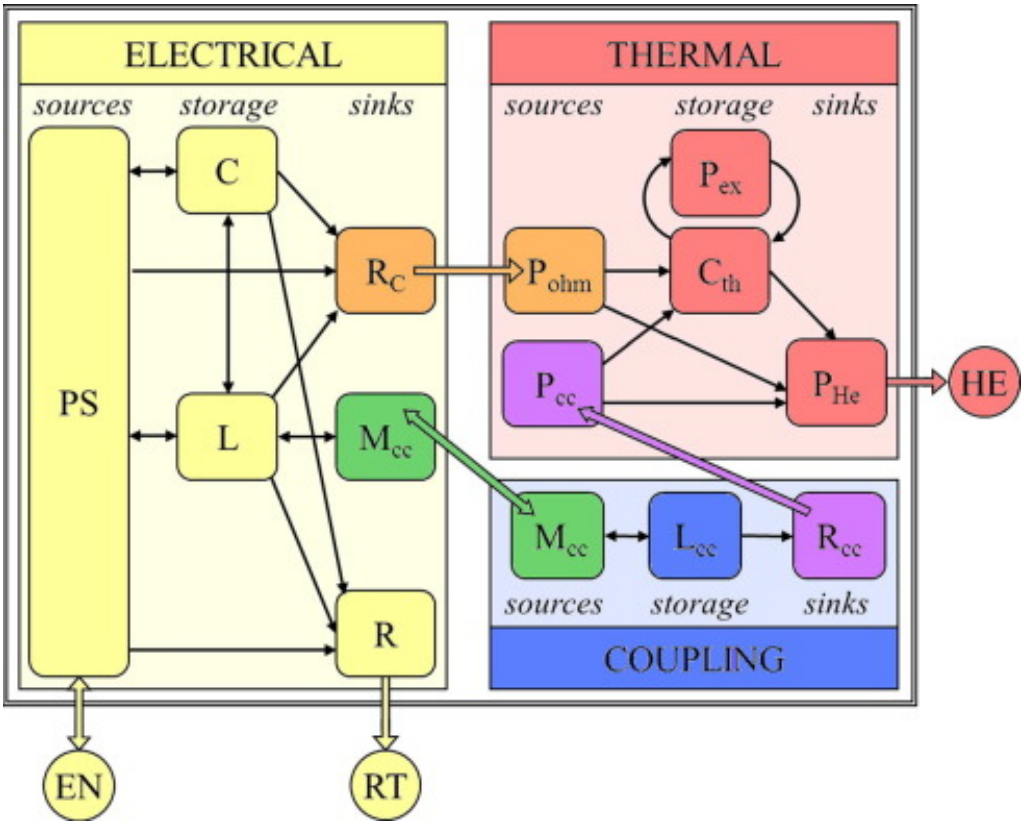

Figure 2.2: Mutual coupling and energy exchange of the the electrical, thermal and transitory coupling domains in a LEDET model [43]. The electrical network consists of a power source (PS) connected to the main electrical network (EN), storage elements (L and C) and sinks. These are split into connecting elements to the thermal network (R_c) and coupling network (M_{cc}) and an infinite sink at room-temperature represented by R and RT. The sources of the thermal network are P_{ohm} and P_{cc} powered by coupling and ohmic loss. The storage elements are C_{th} and P_{ex} representing the heat exchange with other thermal elements. The only thermal sink is the helium bath (HE). The source of the coupling network is M_{cc} powered by coupling currents. The storage is the inductance of the coupling circuit L_{cc}. The coupling sink is R_{cc} which represents the ohmic loss in the coupling network and powers P_{cc} in the thermal network.

A big advantage of the lumped-element method is that it is possible to picture the mutual influences of different physical domains by coupling the lumped elements together. Concerning LEDET this is achieved by coupling the following three sub-networks, electro-magnetic, thermal and transitory coupling. In Figure 2.2 the coupling and energy exchange of these networks is shown [43]. By doing so, LEDET is able to model various transient events in superconducting magnets and circuits. The sub-networks and important parameters for the validation of the MBRD magnet will be discussed in the coming chapters.

2.2.1 Dynamic electro-thermal model

A simplified electrical sub-network of a LEDET model consists of a power source (PS) exchanging or storing energy with capacitive (C) and inductive (L) elements. The energy can then be dissipated in resistive components (R). The network can exchange energy with the outside via two interfaces: the main electric network (EN) and the room-temperature environment as an infinite sink (RT). The electrical network models all conventional electric components like resistors, capacitors, self- and mutual-inductances, diodes, thyristors and switches. The parameters can change due to variation of magnetic field, temperature or transport current. Usually, a superconducting magnet consists of a series of elements which are represented by a self-inductance coupled to other self-inductances and resistances which are non zero when coil parts transition into the normal state. The self-inductance can change with the transport current due to iron yoke saturation. The number of elements which represents a magnet depends on its design and type. For a 2D model of a accelerator magnet, it usually corresponds to the number of coil half-turns.

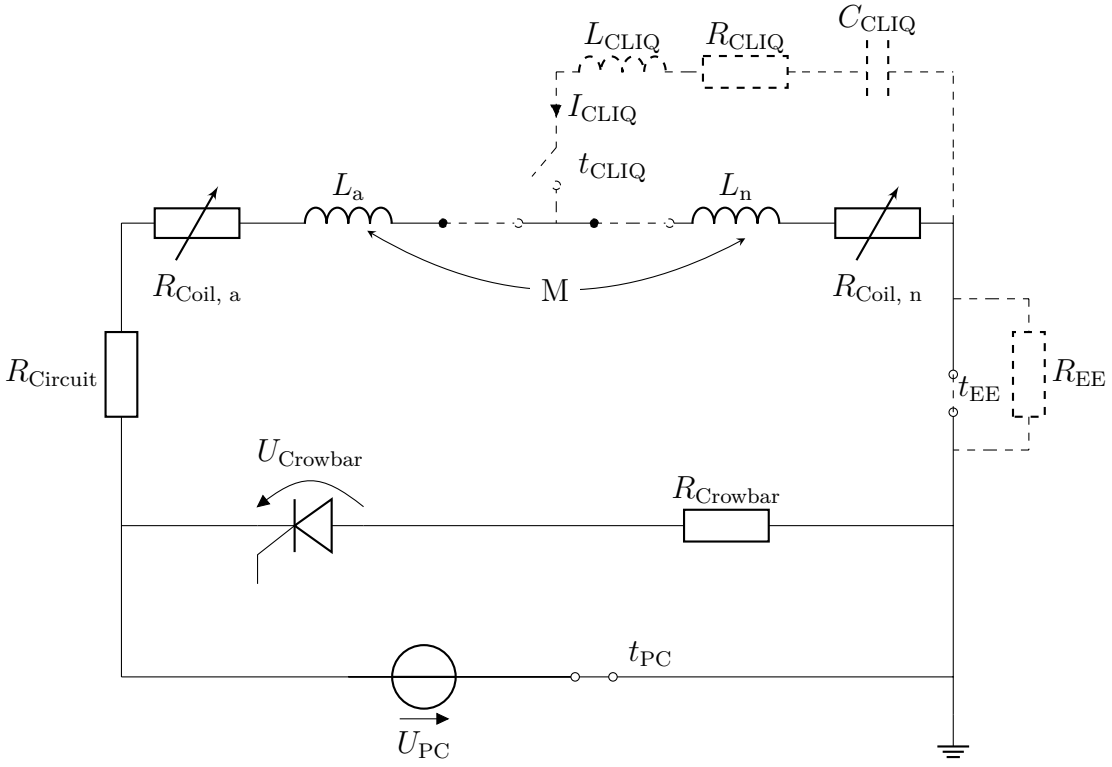

Figure 2.3: Electric network used in LEDET to reproduce the electro-dynamic behaviour of a superconducting magnet and its surrounding components. Dashed elements can be optionally included [49].

Figure 2.3 shows the electric network used in LEDET to model a superconducting magnet and its surrounding electric components more in detail. The model includes the power supply U_{PC} and its switch t_{PC}. $R_{Circuit}$, $R_{Coil,a}$ and $R_{Coil,n}$ represent the electric resistance of the warm parts of the circuit and the coil section, depending

on their physical state, respectively. L_a and L_n correspond to a series of included self-inductances which are mutually coupled by M. When a quench is detected, the power supply switches off and the magnet discharges through an alternative branch with a diode represented by $U_{Crowbar}$ and its corresponding resistance $R_{Crowbar}$. Additionally external quench protection devices are optionally included in the model. t_{EE} and R_{EE} depict an energy extraction system through which the discharge current can decay faster. Also a CLIQ-system [18] can be included which is represented through t_{CLIQ}, I_{CLIQ}, L_{CLIQ}, R_{CLIQ} and C_{CLIQ}.
On a higher level, the interaction with the thermal sub-network is implemented by using a resistor (R_c) simulating the internal ohmic loss per unit volume of a conductor represented as P_{ohm}, as shown in Figure 2.2. The thermal domain again includes storage components (C_{th}) which can exchange heat with each other (P_{ex}). P_{He} represents the heat sink of the sub-network and connects to a helium bath (HE) with a constant temperature.
In the modeling process, the thermal sub-network of a LEDET model is split into a series of thermal elements. Each thermal element represents a certain volume of conductor over which a thermal balance is introduced. The thermal balance in each element (in 2D, corresponding to a half-turn) can be written as follows [43]:

$$P_{if} + P_{is} + P_{ohm} + P_{ex} + P_{sink} = \bar{c}(T)\frac{d(T - T_{He})}{dt} \tag{2.1}$$

P_{if}, P_{is} and P_{ohm} stand for the heat sources of inter filament, inter strand and ohmic loss. P_{ex} represents the heat exchanged with other thermal elements and P_{sink} is the heat flow to the helium bath. $\bar{c}$ corresponds to the heat capacity and T to the average temperature of the thermal element. T_{He} represents the temperature of the thermal sink.
By translating a thermal element into a analogous electrical network, the heat flow would be an electrical current and the temperature gradient would be a voltage potential. Modeling the mutual coupling of the sub-networks gets far simpler by introducing this analogy. One analogous electrical network is shown in Figure 2.4.

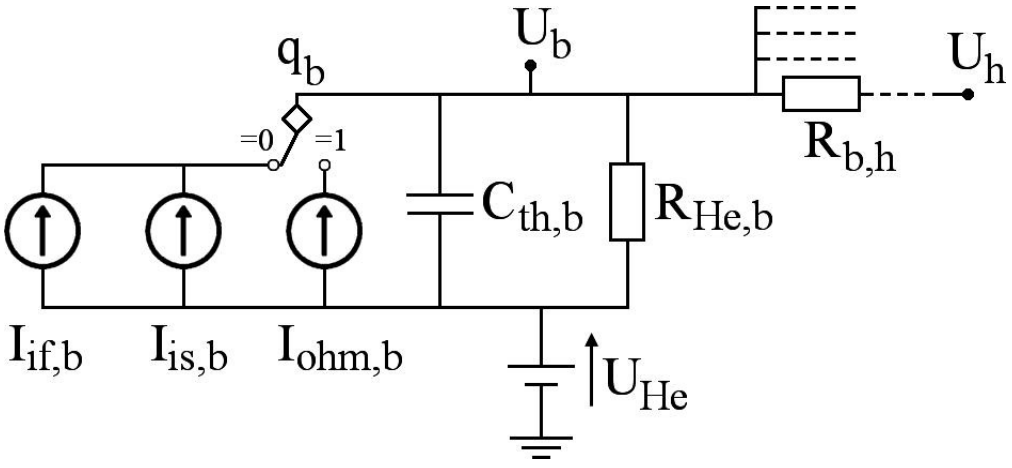

Figure 2.4: Analog electrical network representing one thermal element of the thermal sub-network in LEDET including all inputs, storages and outputs [43].

$I_{if,b}$, $I_{is,b}$ and $I_{ohm,b}$ are corresponding to the before described heat sources. By introducing the switch q_b, it is possible to only include ohmic loss in a thermal element when a quench occurs. $C_{th,b}$ corresponds to the heat capacity of the block, U_b and $U_{He,b}$ represent the temperature of the block and the thermal sink and $R_{He,b}$ and R_b represent the resistance of the insulation layers between the conductor, the helium bath and other blocks, respectively. By giving the possibility to introduce parallel resistances to R_b, the insulation between blocks can be subdivided into layers, thus enhancing the simulation of the heat flow. U_h stands for the temperature of any other thermal element in series to the pictured block. The link of the thermal element to the corresponding electrical sub-network is done via P_{ohm} calculated by $P_{ohm} = R_e \cdot {I_e}^2$. Where R_e represents the sum of all electric elements corresponding to the thermal element in which P_{ohm} acts as ohmic heating, while I_e corresponds to the current flowing in the electrical sub-network. When a quench occurs in the magnet, R_e develops in the electrical domain and q_b switches in the thermal one, thus $I_{ohm,b}$ is active and the magnet heats up.
As superconducting magnets are exposed to field variations coupling currents are developing in the conductor [50],[51]. Coupling currents can flow in loops closed by the contacts of the transposed strands and filaments of the cable [50]. To simulate this behaviour a coupling network is introduced, which is connected to the electrical and thermal networks with dedicated links [43]. A simplified coupling network consists of a coupling element (M_{cc}) which enables energy exchange between the magnet inductance, a storage component (L_{cc}) and a sink (R_{cc}). In the sink energy can be lost as it is connected to the thermal network via the element P_{cc}, shown in figure Figure 2.2.

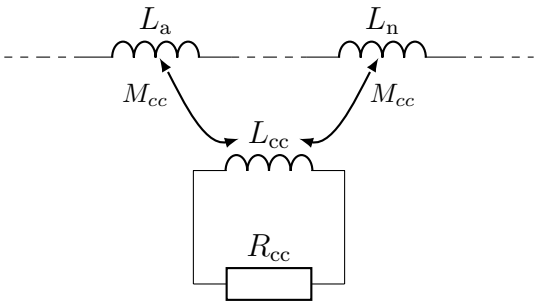

Figure 2.5: Coupling network used in LEDET to reproduce the coupling currents in a superconducting cable.

There are two different coupling currents included in a LEDET model: the inter-filament coupling currents IFCC and the inter-strand coupling currents ISCC. These two cases are covered by a series of two electrical sub-networks which are mutually coupled to the to the coil sections. To be precise, IFCC are split into two sub-networks representing the coupling currents in the two perpendicular directions to the transport current. IFCC are mainly determined by the effective transverse resistivity f_{eff} of the strand, which depends on the type of superconductor and used stabilizer matrix and the filament twist pitch, which determines the size of the IFCC loops. ISCC depend on the cross contact resistance R_c, which determines the resistance of each contact point of the strands, the strand-twist pitch of the cable and the number of strands [18].
All coupling phenomena are modeled with the same setup of electrical sub-network

pictured in Figure 2.5 and are introduced for each coupling phenomena with the same number of elements as thermal elements. The coupling network consists of the self-inductance elements of the magnet L_a to L_n, which are coupled to an external circuit via the mutual inductance M_{cc}. The external coupling circuit consists of an inductance L_{cc} and a resistor R_{cc}, thus this circuit is able to store energy, re-introduce it to the main electrical sub-network and to dissipate it to the thermal sub-network with the before introduced P_{if} and P_{is} as follows [18], [43]:

$$P_{if} = R_{if,x} {I_{if,x}}^2 + R_{if,y} {I_{if,y}}^2 \tag{2.2}$$

$$P_{is} = R_{is} {I_{is,b}}^2 \tag{2.3}$$

By changing the parameters of the coupling circuits the model is capable of simulating the various phenomena of coupling currents in superconducting cables which are exposed to field variations.

2.2.2 Helium cooling

Superconducting magnets used in the accelerators at CERN mostly operate at cryogenic temperatures [12]. The two used superconductors for the HL-LHC have a critical temperature of 18.1 K (Nb_3Sn) and 9.2 K (Nb-Ti), respectively. To be able to withstand thermal variations and further enhance the performance of the magnets used in the LHC and HL-LHC a temperature of 1.9 K is adopted. To ensure this temperature level, the magnets operate in a bath of super-fluid helium [21]. Super-fluid helium has very special characteristics: it possesses frictionless flow and has a thermal conductivity and volumetric heat capacity an order of magnitude higher compared to metals at this temperature. Thanks to its flowing characteristics, He II is able to creep into small voids between strands of a superconducting cable. Sometimes the cable insulation is arranged in such a way that more helium can penetrate the cable [21], so that the heat exchange between cable and helium is further amplified. When the helium liquefies, it loses its near infinite thermal conductivity and in case of evaporation the volumetric heat capacity is negligible, thus the cooling of the cable is dominated by the stabilizer. In Figure 2.6 a simplified insulated cable cross section is shown in which helium penetrates in different amounts.

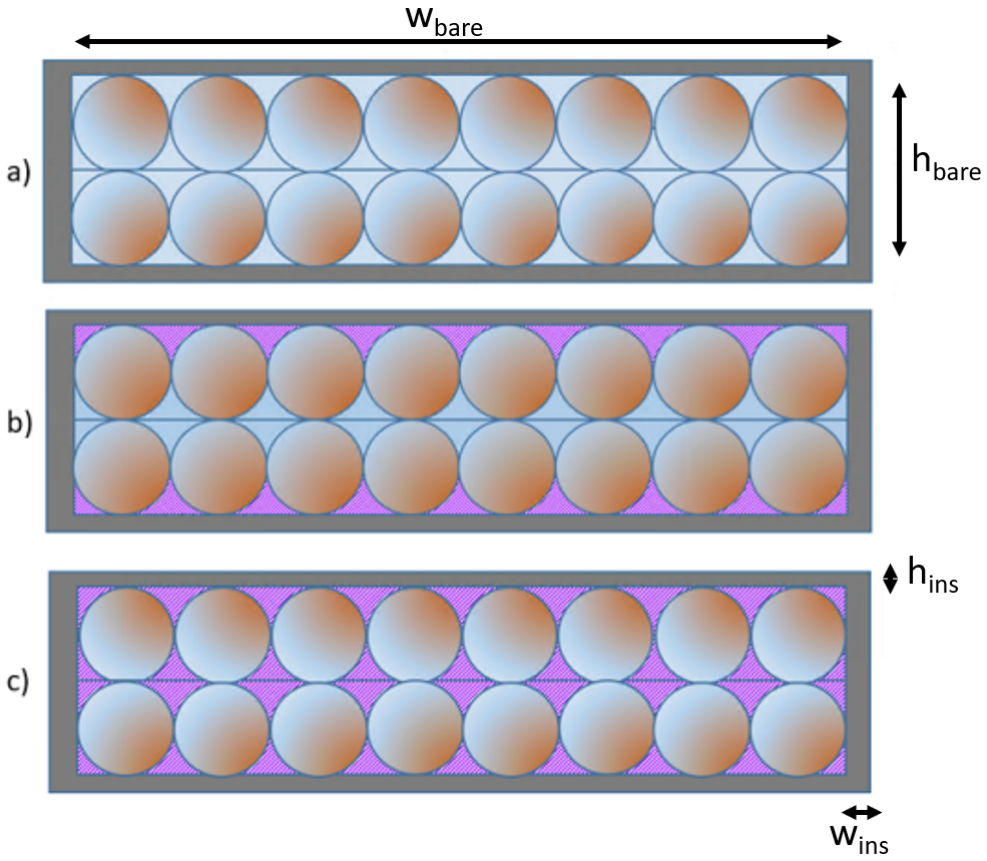

Figure 2.6: Simplified representation of a cable including different states of penetration by super-fluid helium. a) All voids of the cable are filled with helium. b) The outer voids of the cable are filled with insulation. c) No helium inside the cable, all voids are filled with insulation [52]. The width and height of the bare cable and the insulation are illustrated as well.

In a) all the voids of the cable are filled with helium (grey), in b) only about half of the voids are filled with helium and the rest is filled with insulation (magenta) and in c) no void includes helium as the cable is fully impregnated with insulation [52]. The exact amount of helium which penetrates the cable is not easily determinable, but at the same time it is important to include its cooling effect. As the heat capacity and especially heat conductivity of super-fluid helium lies well above the one of the insulation, a small difference in the fraction of helium can make a large difference in the quench margin of the conductor [21]. In LEDET the fraction of helium can be used as fitting parameter, hence it can only be determined with measurements.
In LEDET, the effect of helium cooling inside the cable can be taken into account by introducing two parameters $f_{internal,voids}$ and $f_{external,voids}$. $f_{internal,voids}$ represents the parts of the cable cross-section which are not filled with insulation and lie between the strands. Usually, it is assumed that the internal voids are filled with helium. $f_{external,voids}$ represents the voids between the strands and the insulation around the cable. It can be assumed that these parts are filled with insulation as the cable gets compressed and the insulation deforms into the gaps [12]. The whole cross-section of the cable is composed by the cross-section of the strands the voids and the insulation.

These relative fractions have to fullfill the following:

$$f_{strands} + f_{insulation} + f_{external,voids} + f_{internal,voids} = 1 \tag{2.4}$$

The strands are represented by $f_{strands}$ and the insulation by $f_{insulation}$. As already described, the actual area of the internal voids can not be measured, but a rough approximation can be made as follow, assuming a rectangular cable:

$$A_{bare} = w_{bare} \cdot h_{bare} \tag{2.5}$$

$$A_{insulated} = (w_{bare} + 2w_{ins}) \cdot (h_{bare} + 2h_{ins}) \tag{2.6}$$

Where w_{bare} and w_{ins} are the width of the bare cable and the insulation and h_{bare} and h_{ins} the (average) hights, respectively. The area of round strands is calculated by:

$$A_{strands} = n_{strands} \cdot \pi \cdot \frac{{d_{strands}}^2}{4} \tag{2.7}$$

Where $n_{strands}$ is the number of strands in the cable and $d_{strands}$ their diameter. The fraction of all voids in the cable accumulates to [53]:

$$f_{voids} = \frac{A_{bare} - A_{strands}}{A_{insulated}} \tag{2.8}$$

The internal and external voids can be calculated with:

$$f_{internal,voids} = \frac{(n_{s,l} - 1)(n_l - 1)}{n_{s,l} \cdot n_l} \cdot f_{voids} \tag{2.9}$$

$$f_{external,voids} = f_{voids} - f_{internal,voids} \tag{2.10}$$

$n_{s,l}$ represents the number of strands in one layer and n_l the number of layers. The parameter of helium fraction in the cable $f_{internal,voids}$ can be adjusted between 0 and f_{voids} during the validation of a model to account to the fact that the real amount of helium in the cable is not known.

2.2.3 Quench modeling

When using LEDET in its 2D configuration only the cross-section of the magnet is considered with the possibility of additionally including v_q in the third dimension. To model the closed coil turns of the magnet the concept of half-turns is introduced. The cross-section of a coil turn in the cross-section of the whole magnet represents one half-turn. The half-turns are numbered following the poles of the magnet in geometrical order. The correct electrical order of the half-turns is given as an input by the user.
Introducing heat into a thermal element of a LEDET model, due to IFCL, ISCL or

heat exchange leads to a temperature increase in that element. If the energy entering the element exceeds the energy transferred to the neighbouring half-turns or to the thermal sink, the temperature increases. If the temperature exceeds T_{cs}, part of the current starts flowing in the conductor normal matrix and ohmic loss is generated. If the temperature exceeds T_c, superconductivity is not present and all current flows in the normal conductor. The transition to the normal state can happen not only because the temperature exceeds T_c, but also when B_c or J_c are reached. For example to model the case of sudden quench in a coil spot, the user can set the flag q_b to 1. This can be done in a dedicated time step as well as in a certain turn and in a specific volume of conductor.
A LEDET model comes with two different 2D options. One is solely 2D and simulates all effects in the cross-section of a the magnet. When a quench occurs it assumes the whole turn to be quenched, which is only correct for a quench initiated through IFCC and ISCC. On the other hand, it is possible to introduce a 2D+1D option [54], which includes the following quench settings for every turn of the magnet:

- Time in which a quench will occur in the turn t_{qs}
- Length of the initially quenched conductor l_q
- Scaling factor to manipulate the quench propagation velocity in the direction of the conductor f_{vq}

The 2D+1D option allows to include the longitudinal quench propagation in a half-turn as well as the propagation between half-turns following their electrical connection, though keeping the computational efficiency of a 2D simulation. These settings allow the user to reproduce the quench behaviour in the magnet more effectively [52],[53],[54]. Through t_{qs} it is possible to include time delays caused by t_{QD}+t_v and eventual failure of the quench protection into the model. The length of the initial hot-spot can be set using the parameter l_q, which influences its initial behaviour. Another important parameter to simulate the propagation of the quench in the direction of the conductor is f_{vq}, whose optimization allows the improvement of the transient behaviour of the magnet. As described in section 1.4, v_q is scaled in the half-turns touched by QH due to multiple heating stations. Meaning, f_{vq} has to only be set for the half-turns touched by active heating stations and those in close contact to them. The remaining half-turns will quench by coupling loss, transverse heat diffusion and longitudinal quench propagation in which the inclusion of f_{vq} is not necessary.
Using f_{vq} it is possible to manipulate the adiabatic quench propagation velocity calculated by LEDET with an analytical formula, which does not account for heating stations. Another phenomenon not captured by the analytic formula is the deceleration of the quench propagation due to cooling from the helium which penetrated the cable and from the thermal sink outside the cable. This effect is particularly important at low currents as the cooling effect of the helium is not negligible compared to the ohmic loss in the conductor [29]. At higher currents this effect becomes less noticeable, as the heating through the magnet current is far higher than the cooling effect of the helium [29]. In order to match the lower v_q and the resulting slower discharge of the magnet at low currents $f_{vq} < 1$ can be used. As the corrected quench propagation velocity $v_{q,corrected} = f_{vq} \cdot v_q$ will be used, f_{vq} needs to be calculated and writes as follows:

$$f_{vq} = 2 \cdot \frac{n_{QH,stations} \cdot v'_q}{v_q} \tag{2.11}$$

$n_{QH,stations}$ represents the number of heating stations in one heater strip, which is calculated with Equation 2.12, while the factor two accounts for the two propagating quench fronts to both sides of a heating station.

$$n_{QH,stations} = ROUND(\frac{l_{magnet}}{l_{QH} + l_{cu}}) \tag{2.12}$$

l_{magnet} represents the length of the QH strip, l_{cu} is the length of a copper plated part of the strip and l_{QH} is the length of one heating station. By rounding the equation an integer number for $n_{QH,stations}$ is obtained. v'_q in Equation 2.11 stands for the quench propagation velocity provided by a program including helium cooling inside the cable. In a first step the calculation of v'_q STEAM-BBQ is going to be used. The implementation of a STEAM-BBQ model will be discussed in section 2.3.
The time when the quench occurs in a turn in thermal contact to heaters is calculated by LEDET depending on the conductor parameters and is mainly determined by the time of the thermal diffusion from the QH strips to the coil turns. The half-turns not in contact with active heaters will quench through transient losses and transverse heat diffusion, which is both modelled by LEDET internally and is not set by the user. The half-turns which are in contact to active QH will initially only quench in the longitudinal sections in direct contact with them. Thus, a certain fraction l_q of these half-turns needs to be set to initially quench depending on the amount and length of the heating stations. This can be calculated as follows:

$$l_q = l_{magnet} \cdot \frac{l_{QH}}{l_{QH} + l_{cu}} \tag{2.13}$$

The parts of the half-turns not in contact to heating stations will quench due to the longitudinal propagating quench now depending on f_{vq}.

2.3 BBQ model of quench propagation in superconducting strands

BBQ is a FEM-based model implemented in COMSOL-Multiphysics. It can be used to simulate the behaviour of a single superconducting cable and in particular to calculate properties, such as the quench propagation velocity, hot-spot temperature and voltage across the conductor. The model includes heat transfer calculated by COMSOL, material properties from the STEAM library implemented as C-functions and manually implemented functions taking into the superconducting regime into account. BBQ is able to model the cooling through He II inside and outside of the cable and thereby it can be used to improve the simulation of the behaviour during a quench.

2.3.1 Thermal implementation

The thermal implementation of a BBQ model has a dimensionality of 1D+1D, which means that the heat flow is calculated along the conductor center and transversely through the insulation. The longitudinal propagation is calculated from node to node inside the conductor. From each of these nodes transverse propagation through the insulation, which is subdivided into six layers, is calculated. The longitudinal heat flow in the insulation is not taken into account as it is negligible with respect to that in the conductor. The outermost node of the insulation has an optional link to the thermal bath which enables the model to include cooling by helium. The described thermal structure of the model is shown in Figure 2.7. While the first layer of insulation is isothermal to the busbar, the thermal resistance between each insulation layer is given by the material properties. The heat flow to the thermal bath is calculated including Kapitza cooling and film-boiling as this models the behaviour of He II sufficiently well [40], [55].
The current flowing in the busbar is fixed to an initial value and can decrease from that after reaching a set voltage threshold to simulate triggering of the quench protection. As the model is mainly used to investigate a quenching conductor, a Gaussian temperature profile is set in a specific point of the busbar. The initial temperature, width and location of the profile can be given by the user. The heat corresponding to the initial temperature profile will travel along the conductor and result into a propagating quench if the ohmic loss is higher than the cooling. The quench propagation velocity is calculated from comparing the time when the quench passes to specific points. For the sake of simplicity, a fixed temperature threshold of 8 K is selected for the calculation of the normal-zone propagation velocity. The calculation can be written as follows [55]:

$$vq_{BBQ} = (T_{p2} > 8\ \mathrm{K}) \cdot \frac{p_2 - p_1}{t_{p2}} \tag{2.14}$$

The main parameters and settings for a BBQ simulation can be given in the basic COMSOL interface for user input. The key parameters of a BBQ simulation are given in Table 2.1.

Key parameters of a BBQ simulation

Parameter name	Unit
Current	A
Busbar length	m
RRR	
Magnetic field scaling	$\frac{T}{A}$
Fraction of superconductor	
Mesh size	m
Diameter strand	m
Number of strands	
Insulation thickness	m
Cable width	m
Cable height	m
$wetted_p$	

Table 2.1: Parameters of a BBQ simulation, which can be accessed and changed from the COMSOL interface [55]. The RRR is given as the ratio of the cable resistivity at 10 K and 295 K. The magnetic field scaling has to be calculated in a known point of operation and is then used for all current levels. $wetted_p$ is used to include helium cooling inside a multi-strand cable and is introduced in subsection 2.3.2.

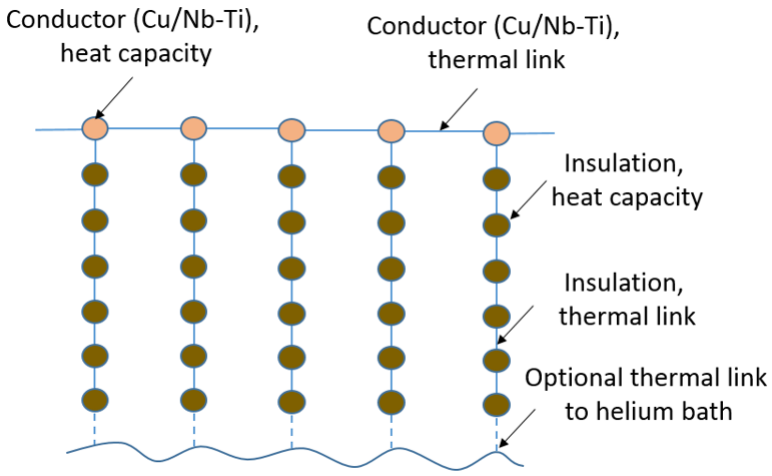

Figure 2.7: Thermal structure of a BBQ model with a 1D+1D dimensionality. In orange the subdivision of the busbar is shown including the heat capacity of the conductor depending on its composition. In brown the subdevision of the conductor insulation are shown including their heat capacity. All nodes are connected through thermal links shown represented by blue lines. The last node of the insulation has an optional link to a helium bath to include external cooling [55].

It is important to note that BBQ always expects a round conductor with just one strand. Hence, to implement a rectangular Rutherford cable with multiple strands the inputs have to be converted. To calculate the cross section of all strands Equation 2.7 is used and serves as input for BBQ.

The circumference of the cable used in BBQ corresponds to the perimeter of the rectangular cable, as follows:

$$per_{total} = 2 \cdot w_{bare} + 2 \cdot h_{bare} \tag{2.15}$$

per_{total} is used by the model to calculate the heat propagation through the insulation and eventually to the thermal bath.

2.3.2 Adaption of BBQ to include internal cooling

The previously described BBQ model includes the possibility to consider external cooling from a thermal bath outside the cable. To include helium cooling from inside the cable, as described in subsection 2.2.2, another path for the heat flow to propagate needs to be implemented. In Figure 2.8, the additional heat path directly connecting the conductor to the helium bath is shown in red and the original path via the insulation is highlighted in green. As the cooling effect of the internal helium is highly dependant on how much of the circumferences of the strands are in direct contact to the helium, a scaling parameter $wetted_p$ is introduced. Like the external, the internal helium is suggested to be a thermal sink at constant temperature. Thus only the circumference of the strands which is not in contact to helium should be taken into account for the heat flow through the insulation. The dedicated formulas to calculate the relevant perimeters for both heat flows are shown in Equation 2.16 and Equation 2.17.

$$per_{internal} = wetted_p \cdot \pi \cdot n_{strands} \cdot d_{strands} \tag{2.16}$$

$$per_{external} = (1 - wetted_p) \cdot \pi \cdot n_{strands} \cdot d_{strands} \tag{2.17}$$

In the BBQ model the heat flow to the internal helium includes Kapitza cooling and film-boiling and uses the busbar domain as input to calculate the cooling [40], [55].

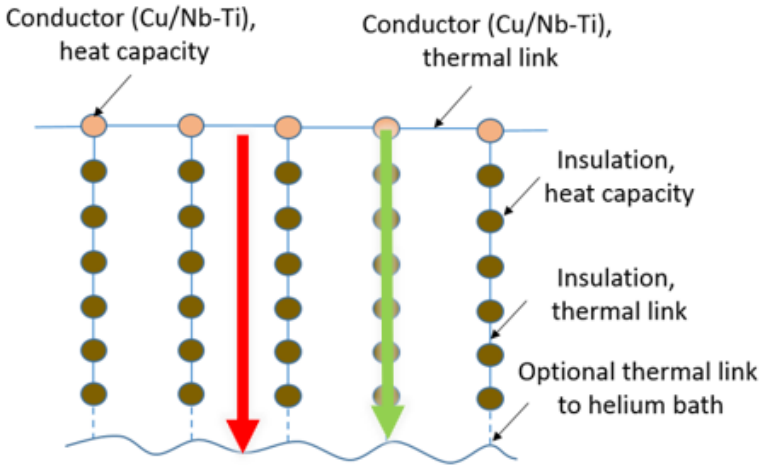

Figure 2.8: Original thermal structure of a BBQ model, enhanced with a thermal path directly to the thermal bath to include helium cooling inside the cable in red and the original path via the insulation in green [55].

The implementation of BBQ in COMSOL-Multiphysics limits the use of the model as stand alone and it is time consuming to use in a consecutive simulation as it involves transferring the outputs by hand. Thus, it is of great interest to implement a similar model in Python and automatise a consecutive simulation with LEDET.

2.3.3 Benchmarking of PyBBQ

PyBBQ is a newly implemented tool in Python and can be used to simulate quenches in a superconducting conductor and can be included in consecutive simulations in the STEAM framework. PyBBQ uses a 1D+1D approach for the thermal implementation and is in many ways comparable to BBQ but uses a finite difference nodal network model [40],[30],[55]. As PyBBQ is not yet validated for multi-strand cables, this work was performed as part of this thesis. To simplify the benchmarking process results of PyBBQ were compared to results obtained by BBQ, LEDET used in its 3D configuration [45] and an analytical equation for the adiabatic normal-zone propagation velocity [56], which is the one implemented in LEDET when run in the 2D+1D configuration. First the analytical equation and LEDET 3D will be described briefly before the benchmarking process will be shown.

Implementation of LEDET 3D for single conductors

LEDET 3D [45] comes with an automatic way to produce 3D-geometries such as magnets, coils and conductors. In the described case of calculating v_q, only the straight part of a conductor is needed, which simplifies the simulation by a wide margin. Simplifications done in LEDET 3D are that material- and physical properties are uniform within each element, heat diffusion along the direction of the conductor is considered only through the stabilizer and heat is generated due to ohmic loss and IFCL. External cooling can be included while internal cooling is neglected for multi-strand cables. As LEDET 3D does not have a v_q calculation included, since the quench propagation is calculated as a result of the 3D thermal diffusion and superconductor state, this is done in post processing by applying the same assumptions as in BBQ and PyBBQ.

Analytical calculation

The analytical function used to validate PyBBQ is the same used internally by LEDET and is described more in detail in [56]. The calculation depends on the conductor cross-section and composition, its magnetic field and current density, and the thermal-sink temperature. The impact of cooling and of the insulation layer is neglected. The calculation allows Nb-Ti or Nb_3Sn as superconducting materials. The material properties like heat capacity and thermal conductivity are taken from the STEAM material library [57],[58].

Benchmarking

To simplify the simulation and limit the amount of parameters PyBBQ will first be validated using a short, single strand conductor without insulation and cooling. The

conductor chosen is used in the MQSX magnet [59] and its parameters are shown in Table 2.2.
In Figure 2.9 the comparison of PyBBQ, BBQ, LEDET 3D and the analytical calculated curve are shown. The simulated values of the three software agree very well for most current levels. At high current PyBBQ simulates 10 % lower values than BBQ and LEDET 3D. The analytical calculation lies 30-40 % below the simulated values, which is not fully understood yet and will be part of further research. The analytically calculated curve will still be shown as comparison in the future plots of the benchmarking process as it is used in LEDET 2D+1D.

Key parameters of the MQSX strand [59] used for benchmarking

Parameter name	**Unit**	**Value**
Current	A	50 - 650
Busbar length	m	0.223
RRR		100
Magnetic field transfer function	$\frac{T}{A}$	$7.16 \cdot 10^{-3}$
Fraction of superconductor		0.385
Mesh size	m	< 0.001
Diameter strand	μm	937
Number of strands		1
Insulation thickness	μm	0.0 / 60
Cable width	μm	1130
Cable height	μm	610
$wetted_p$		0.0

Table 2.2: Values of the key parameters for the PyBBQ benchmarking. The current range chosen reaches from low current to a 20 % over-current in respect to the nominal current of this magnet. The busbar length of 0.223 m is used as it is sufficient to avoid end effects during the considered transient. The insulation thickness of 0.0 m is used in case of a simulation without insulation.

Figure 2.10 shows the simulation results for the MQSX strand including insulation and cooling from a helium bath at 1.9 K for PyBBQ, BBQ, LEDET 3D. The inclusion of cooling shows its main effect at currents lower than 300 A where it has a bigger influence as the power produced in the hot-spot is lower and the cooling effect by the helium bath has a higher impact. As LEDET 3D has a limited ability to include cooling by a helium bath PyBBQ and BBQ show lower values for v_q below 300 A. The analytical calculation also does not include cooling, which leads to lower values for PyBBQ and BBQ below 150 A. It is important to note that an insulation around the simulated cable was taken into account for the mentioned simulations, which made less than 1 % difference in v_q compared to the case without insulation shown in Figure 2.9 if cooling is neglected. As for both simulated cases PyBBQ showed good agreement with other software and showed the expected behavior at low currents when including cooling, further simulations with multi-strand cables can be carried out.

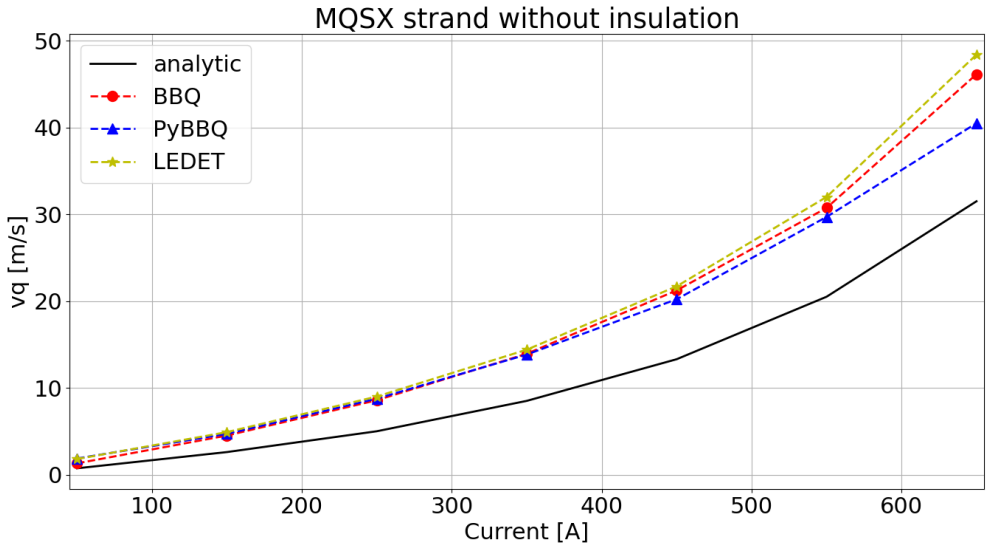

Figure 2.9: Comparison of simulation results of PyBBQ, BBQ, LEDET 3D and analytical calculation of v_q for the MQSX strand without insulation. The dashed blue, red and yellow curves represent PyBBQ, BBQ and LEDET, while the black curve shows the results of the analytical calculation.

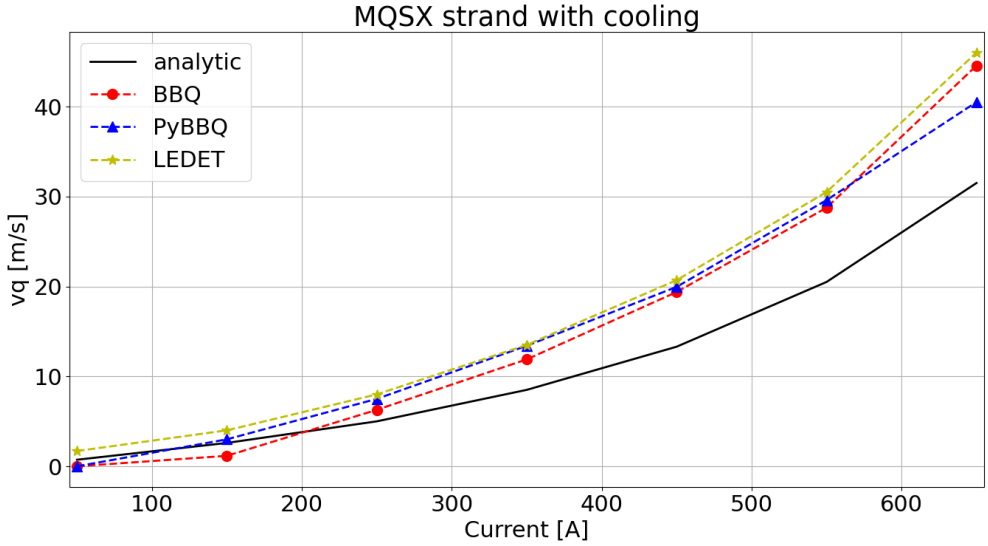

Figure 2.10: Comparison of simulation results of PyBBQ, BBQ and LEDET 3D for v_q for the MQSX strand including insulation and cooling from a helium bath at 1.9 K. The dashed blue, red and yellow curves represent PyBBQ, BBQ and LEDET, while the black curve shows the results of the analytical calculation not including cooling and insulation as reference.

In a second study, simulation results and analytical formula will be compared using a multi-strand Rutherford cable. The cable chosen is used in the MBRD magnet and its key parameters are shown in the following table [8].

Values of the key parameters of the MBRD [8] cable used for PyBBQ benchmarking

Parameter name	Unit	Value
Current	A	2000 - 13300
Busbar length	m	0.1925
RRR		197
Magnetic field transfer function	$\frac{T}{A}$	$244 \cdot 10^{-6}$
Fraction of superconductor		0.384
Mesh size	m	< 0.001
Diameter strand	μm	825
Number of strands		36
Insulation thickness	μm	123
Cable width	mm	15.1
Cable height	mm	1.48
$wetted_p$		0.0 / 0.5

Table 2.3: Values of the key parameters for the PyBBQ benchmarking. The current range goes from low current to ultimate current in respect to this magnet. The length of the busbar is chosen as half of the length between heating stations of the QH of the MBRD magnet. For the inclusion of cooling inside a multi-strand cable $wetted_p$ has to be included and is chosen at 0.5 as a reasonable first guess.

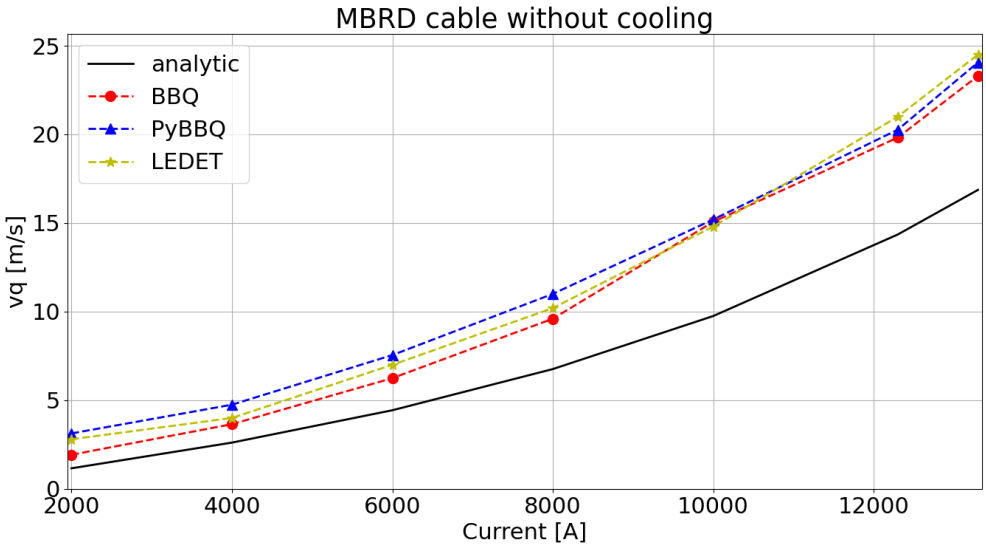

Figure 2.11: Comparison of simulation results of PyBBQ, BBQ, LEDET 3D and the analytical calculation of v_q for the MBRD cable without cooling. The dashed blue, red and yellow curves represent PyBBQ, BBQ and LEDET, while the black curve shows the results of the analytical calculation without insulation.

The simulation results for the MBRD cable excluding cooling are shown in Figure 2.11 for the three programs and the analytical formula. Like for the MQSX strand, the

simulated values of the three software lie in the same range of v_q and the analytical curve suggests lower values.
As the results of the PyBBQ simulations are consistent for two different conductors and for single- and multi-strand cables, PyBBQ is considered to be validated for similar conductors and operating conditions. The effect of helium cooling inside the cable can be investigated in the next step.
Figure 2.12 shows simulation results of PyBBQ and BBQ for the MBRD cable including external and internal helium cooling at 1.9 K. As LEDET 3D does not offer the option to include cooling from the interior of the cable, it is not used in the shown case. As reference the analytical calculation is also plotted. The value of $wetted_p$ is in this case chosen to be 0.5 as this can be a good first approximation taking the geometric properties of the used Rutherford cable into account. This value needs to be confirmed by later simulations and comparison to measurements (see section 4.3). For low currents, the power deposited in the hot-spot is not enough to propagate the normal zone through the cable as the cooling provided by helium, which penetrated the cable, is high enough that the cable recovers the superconducting state. When increasing the current the quench starts propagating at a specific current level after which the helium cooling is not sufficient to recover the superconducting state. The rather sharp rise of v_q can be observed for PyBBQ and BBQ at different current levels. PyBBQ simulates an earlier normal-zone propagation condition at 4800 A compared to 5200 A simulated by BBQ. The qualitatively different behaviour of the analytical calculation at low currents is due to neglecting any cooling effect of the helium inside and outside of the cable. As it is quite difficult to simulate the exact point when the quench starts propagating and PyBBQ and BBQ show similar overall behavior, one can conclude the two programs yield compatible results. Given that PyBBQ is freeware and is easier to integrate in the STEAM framework, it is very convenient to use it in future simulations as an effective alternative to BBQ.
The matching results of the used software are extremely relevant for any LEDET 2D+1D simulation for quench protected magnets with multi-strand Rutherford cables at low currents. By implementing a consecutive simulation of PyBBQ and LEDET the effect of helium cooling inside the cable can be taken into account and an improvement in simulating magnet discharges can be achieved, especially at low currents.
To quantify the effect of helium cooling on v_q the ratio between v_q simulated by PyBBQ and the analytical calculated value is shown in Figure 2.13. From a current level of 4800 A the ratio develops fast to a constant plateau around 1.2. This ratio indicates the required scaling of v_q for a LEDET simulation of the MBRD magnet.

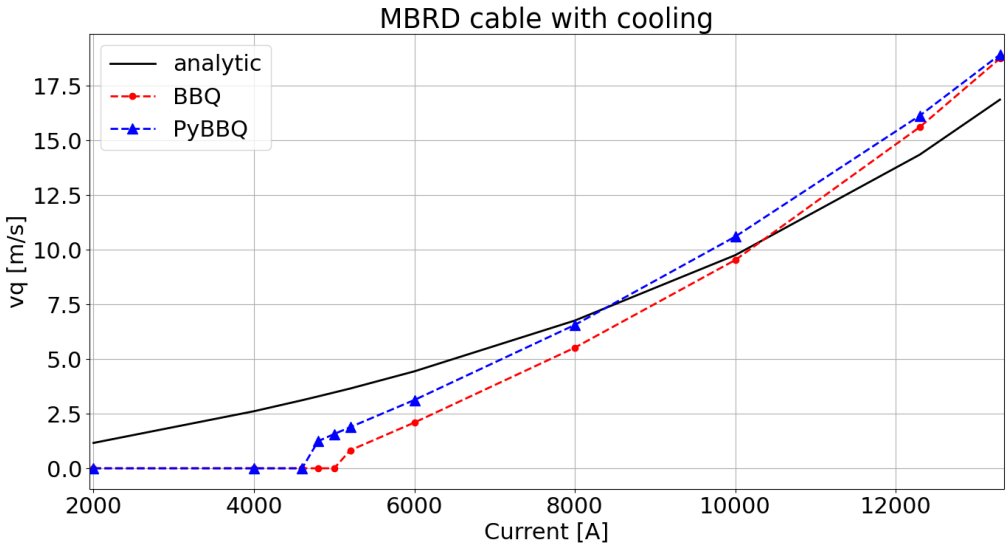

Figure 2.12: Comparison of simulation results of PyBBQ and BBQ of v_q for the MBRD cable with cooling. The simulation results shown in blue and red include external as well as internal helium cooling while the analytical calculation in black does not include insulation and cooling of the cable.

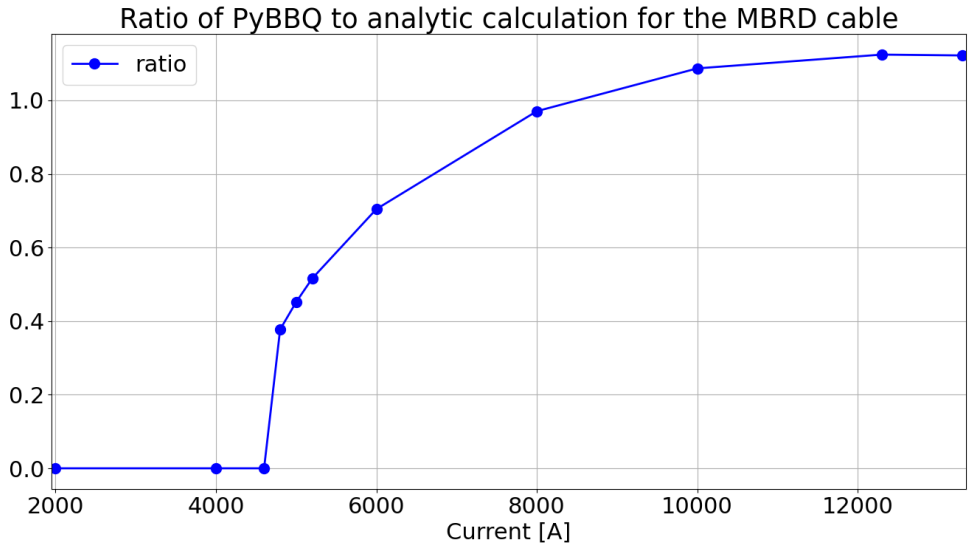

Figure 2.13: Ratio of v_q simulated by PyBBQ and the analytical calculation for the MBRD cable.

3 Python based framework for model generation

The STEAM framework was recently restructured in order to improve the performance and integration of the STEAM-Framework and at the same time improving user friendliness. Originally based on various stand-alone programs with different input files, the goal is to have only one standardized type of input file which can be used for all the tools included in the framework. Co-simulation, post processing and plotting were standardized and included as well. Repeatability of simulations and analysis were ensured by coding pre-defined actions that can be performed automatically in a sequential analysis. The newly restructured framework STEAM-SDK[1] [37], [38] was developed in Python and utilizes standardized YAML[2] input files.

3.1 STEAM-SDK

STEAM-SDK is a Python based framework including all the tools of the STEAM-Framework. Its tools are under permanent development and new tools can be added if needed.

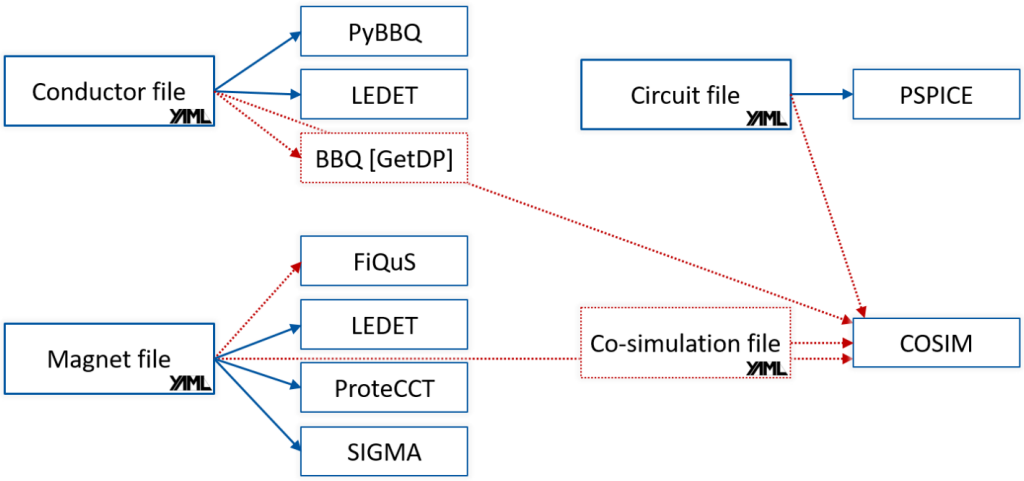

Figure 3.1: Current tools of STEAM-SDK, their inputs and interconnection are shown in blue. The red tools and connections still need to be implemented and are shown for completeness [39].

The structure of how a simulation tool of the STEAM-Framework can be used is given in Figure 3.1. A YAML file is given as input. This change was introduced in the beginning of 2022. Before the change, the model inputs were mainly provided as Excel files and Jupyter notebooks encapsulating model parameters. From an input file of a

[1] Software Development Kit
[2] Yet Another Markup Language

conductor, which can be created from scratch or taken from the model library, various simulations with PyBBQ and LEDET can be carried out. Circuit input files can be used solely in PSPICE (SING). For magnet files more options with FiQuS, LEDET, ProteCCT and SIGMA are included.
The simulations described in this thesis were performed in the framework of the STEAM-SDK. To enhance the accuracy of a simulation of quench behaviour of a magnet PyBBQ and LEDET were used in a consecutive simulation. In the process of implementing the consecutive simulation a script was developed, which structures the simulation process and automatizes it as much as possible. PyBBQ is used to calculate the scaling factor for the normal-zone propagation velocity, including cooling, and this information is passed to the LEDET model, which is used to simulate the transient of the magnet during the discharge.

3.2 Simulation structure

Performing an analysis of a magnet, conductor or circuit in the STEAM-SDK framework is structured in the following way: From a main Python script an analysis function is called using an input file, which structures the whole simulation process as a series of pre-defined, sequential steps. The same function also uses the dedicated magnet data from a library of conductor, magnet, and circuit models. An example for a simulation of the MBRD magnet using LEDET is given in Figure 3.2.

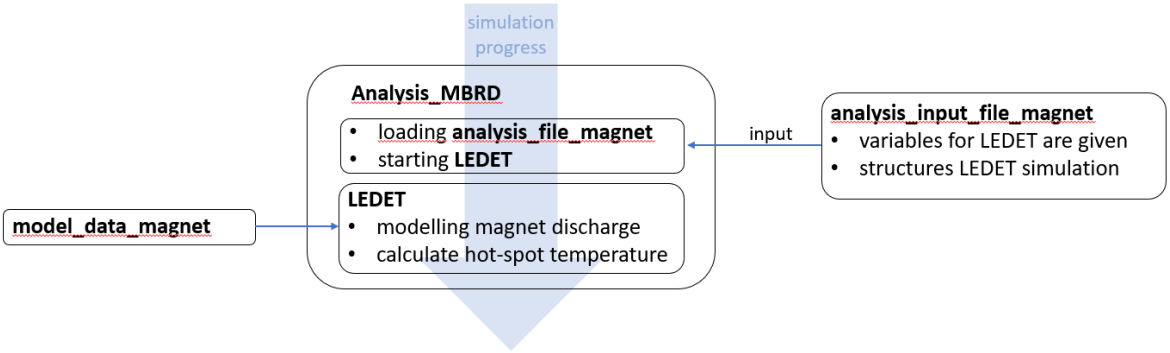

Figure 3.2: Structure and inputs of a simulation script, which runs a LEDET simulation using STEAM-SDK.

The model data of the magnet contains all the relevant inputs to describe the magnet and its conductor, its initial conditions, quench protection elements, and simulation options, such as geometry details, quench protection and flags defining which physics apply. The analysis file consists of five main parts:

- General Parameters
- Permanent Settings
- Working Folders

- Analysis Step Definition
- Analysis Step Sequence

In General Parameters the magnet name and file name are set. The Permanent Settings contain necessary paths to the programs used in the simulation. This guarantees that a trace of the software version used for the analysis is recorded. The output and input folders are defined in Working Folders. Analysis Step Definition is divided into three parts. First, setting up the working folder and making a reference model using the input from the magnet model data. Second, modifying selected variables of the magnet model data to carry out multiple simulations. Third, defining which simulations should run by listing the desired simulation numbers.
One step to modify the magnet model data consist of the following entries:

- step name
- type
- variable to change
- variable value
- simulation number
- simulation name
- software

The step name structures the simulation process and will be used by the program to conduct the defined steps after each other. The type defines the purpose of the current step, e.g. modifying one or multiple input parameters. The input parameters to be modified and their related values are given under the steps variable to change and variable value. To specify the current simulation and output folder the simulation number, simulation name and used software are given in the last three steps.
In Analysis Step Sequence all steps, which should be carried out and where before defined in Analysis Step Definition, are listed.

3.3 Consecutive simulation of LEDET and PyBBQ

In order to perform a consecutive simulation of PyBBQ and LEDET a main Python script, one analysis file and two model data files are needed. An example of such a consecutive simulation is given in Figure 3.3. The analysis file in this case is used in a different way than described before. It contains relevant inputs provided by the user to run an external Python function which executes the actual simulation. In contrast to a single software simulation the main Python script ("Analysis_MBRD_co_simulation") reads the "analysis_file_co_simulation" and at the same time calls "Custom_function_QH_PyBBQ_LEDET" while providing the necessary inputs [30],[37],[38],[60],[61]. For the described consecutive simulation following inputs are given in "analysis_file_co_simulation":

- magnet_name
- conductor_name
- trigger_time_QH
- QH_strips_active
- turn_number_quench
- quench_time
- length_initial_hotSpot
- scaling_vq_initial_hotSpot
- start_adiabatic_calculation
- file_name_analysis_cond
- file_name_analysis_mag
- current_level
- wetted_p
- f_inner_voids
- f_outer_voids
- software
- flag_run_PyBBQ
- flag_run_LEDET
- simulation_numbers

With “magnet_name” and “conductor_name” the used magnet and its conductor are defined. “trigger_time_QH” defines at which time all QH strips set in “QH_strips_active” are fired. To be able to set a quench in a specific turn and time “turn_number_quench”, “quench_time”, “length_initial_hotSpot” and “scaling_vq_initial_hotSpot” need to be set. The names of the analysis files structuring the PyBBQ and LEDET simulations are given with “file_name_analysis_cond” and “file_name_analysis_mag”. With the provided consecutive simulation parametric sweeps are possible for the current level of the magnet, helium cooling inside the cable, fraction of the inner and outer voids of the cable by setting “current_level”, “wetted_p”, “f_inner_voids” and “f_outer_voids”. To save simulation time and increase flexibility the used software can be adapted and either PyBBQ or LEDET simulations can be skipped by setting the dedicated flags “flag_run_PyBBQ” and “flag_run_LEDET”. In order to specify the simulation name the simulation numbers can be provided under the input “simulation_numbers”.
When “Custom_function_QH_PyBBQ_LEDET” is called it automatically creates another analysis file (“analysis_file_conductor”) by using some of the above described inputs which structures the PyBBQ simulation and is saved in an assigned output folder. As PyBBQ is used to calculate the quench propagation velocity in the conductor, specific inputs (“model_data_conductor”) have to be given in addition to the magnet specific inputs (“model_data_magnet”). These contain the length

of the conductor between heating stations, the insulation thickness, the current and magnetic field in the conductor and inputs related to the helium cooling. Included in "Custom_function_QH_PyBBQ_LEDET" the quench propagation scaling f_{vq}, described in subsection 2.2.3, is calculated under the simulation step "Calculating_scaling_vq".

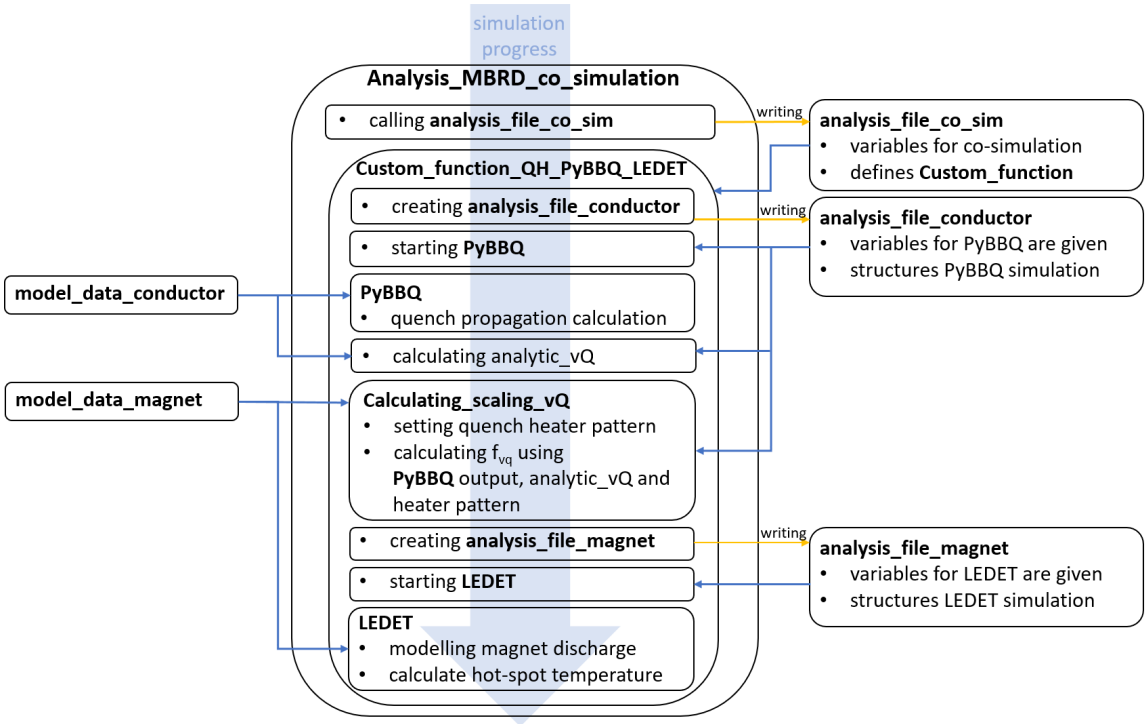

Figure 3.3: Structure and inputs of a consecutive simulation script, which combines a PyBBQ and LEDET simulation. The consecutive simulation includes the calculation of v_q' using PyBBQ and implementing f_{vq} in the LEDET input.

To calculate f_{vq}, the QH setup of the magnet needs to be considered, which is taken from "model_data_magnet". In addition the output of the PyBBQ simulation is used as well as the internally calculated analytical quench propagation velocity. To only implement f_{vq} for half-turns in contact to active QH and half-turns close to them, the active heater strips need to be considered. A second analysis file ("analysis_file_magnet") is created in which f_{vq}, current levels and other inputs necessary for the current use case and a complete LEDET simulation are set. The output of the LEDET simulation is provided in the usual report and Matlab files and are written in the assigned output folder. By defining further steps in the "analysis_file_magnet" comparison to measurements and metrics can be conducted to support the validation process of a magnet model.

4 Model validation

To validate the consecutive simulation model of PyBBQ and LEDET, measurements of the short model of the MBRD magnet are used. The main difference between the short model and the baseline magnet is the length of 1.378 m compared to 7.78 m. All other features are either irrelevant for quench protection or similar and are given in Table 4.1. Parameters which can be adapted for validation are listed in Table 4.2. As no measurements for the baseline magnet exist and only minor differences and the length variation exist the consecutive simulation validated with the short magnet model will be used for the baseline version as well. The key parameters for the baseline magnet will be discussed in chapter 5.
During the validation process, parameters of the magnet can be changed to better fit the measurements. For a LEDET simulation these usually are the RRR if it is unknown and f_{eff} and R_c to adapt the transient losses. Additionally $f_{internal,voids}$ can be adapted to meet the measured quench start with the simulation and in a consecutive simulation with PyBBQ $wetted_p$ can be changed to account to cooling in the cable.
For this particular magnet the measured RRR is 197 as the ratio of the resistances at the temperatures of 10 K and 295 K. In LEDET it is calculated between 10 K and 273 K as it relies on the NIST[1] fit for the conductivity of copper. PyBBQ uses the same temperatures as the measurement. For the variation of $wetted_p$ a range of 0.3-0.7 is used as these are reasonable values for the amount of strand surface which can be in contact with helium, due to geometry restrictions. $f_{internal,voids}$ can vary from 0 % to the value of 11.86 % corresponding to all voids of the cable. It varies between 1 and 3 % in this validation. These values provided better agreement with the measurement but are very low for multi-strand Rutherford cables. f_{eff} and R_c will be used later to fine tune the simulation. For the measurements conducted on the MBRD short model the impact of coupling loss is expected to be low until triggering of the EE.

Known design features and parameters of the short model of the MBRD magnet [8] and its circuit

Parameter	Unit	Value
Bore / Peak magnetic field at I_{nom}	T	4.5 / 5.28
I_{nom} / I_{ult}	A	12300 / 13300
Magnetic length	m	1.378
Number of: apertures / coils blocks per coil / turns per coil		2 / 4 5 / 31
$R_{Circuit}$	$\mu\Omega$	36
$U_{Crowbar}$	V	1.28
RRR		182 / 197

Table 4.1: Known design features and parameters of the MBRD short model. $R_{Circuit}$ and $U_{Crowbar}$ are calculated and the RRR is measured, thus, these parameters will not change during validation.

[1] National Institute of Standards and Technology

Variable parameters of the short model of the MBRD magnet [8]

f_{eff}		1-2
R_c	$\mu\Omega$	$\sim$100
$wetted_p$		0.3-0.7
$f_{internal,voids}$	%	1-3

Table 4.2: Variable parameters of the MBRD short model. These parameters will be investigated and might change in the validation process.

4.1 Measurements

The current levels of the measured discharges of the MBRD short model lie between 2000 A and 13300 A and are divided into six steps. The measurements were carried out at the CERN magnet test facility [62]. The test plan and the key parameters are shown in Table 4.3. The low current tests are taken first to confirm the functionality of the magnet after which the current level increased steadily. The two highest tests in current level are 12300 A and 13300 A, which represent the nominal and ultimate current of the magnet. In all cases an energy extraction EE is used with decreasing delay while increasing the current, with the exception being the 10000 A case with a delay of 240 ms.

Test plan of the MBRD magnet

Current [A]	**EE delay [ms]**	**R_EE [Ω]**	**QH delay [ms]**	**Temperature [K]**
2000	1000	0.04	-90	1.9
4000	1000	0.04	-70	1.9
6000	140	0.04	-54	1.9
10000	240	0.04	-39	1.9
12300	130	0.04	-32	1.9
13300	100	0.04	-30	1.9

Table 4.3: Key parameters for all discharges performed for the MBRD magnet. All tests were performed with energy extraction at different trigger times. The quench was in all cases triggered by QH firing. The temperature and resistance of the energy extraction where fixed at 1.9 K and 40 mΩ, respectively.

Figure 4.1 represents the cross-section of the MBRD short model, including the naming of the apertures, coils, coil blocks, QHs and QH strips. Aperture 1 lies on the left and aperture 2 on the right. Coil A is placed on the bottom in aperture 1 while it is placed on the top in aperture 2. Coil B complements each aperture on the opposite side to coil A. For all coils the coil block nearest to the mid-plane is block 1 and the other blocks are numbered in ascending order. The QHs are ordered as follows: QH1, QH2, QH5 and QH6 placed on aperture 2 and QH3, QH4, QH7 and QH8 placed on aperture 1. The QH strip closer to the mid-plane is named a, while the other is b.
Due to damage during the assembly of the magnet, only QHs in aperture 2 are usable. The used QHs in the tests to first trigger the quench are QH5 and QH2. This means

that aperture 1 is not influenced by direct heating from QHs during the tests. The parameters and exact placement of the two triggered QHs are described in section 4.2.

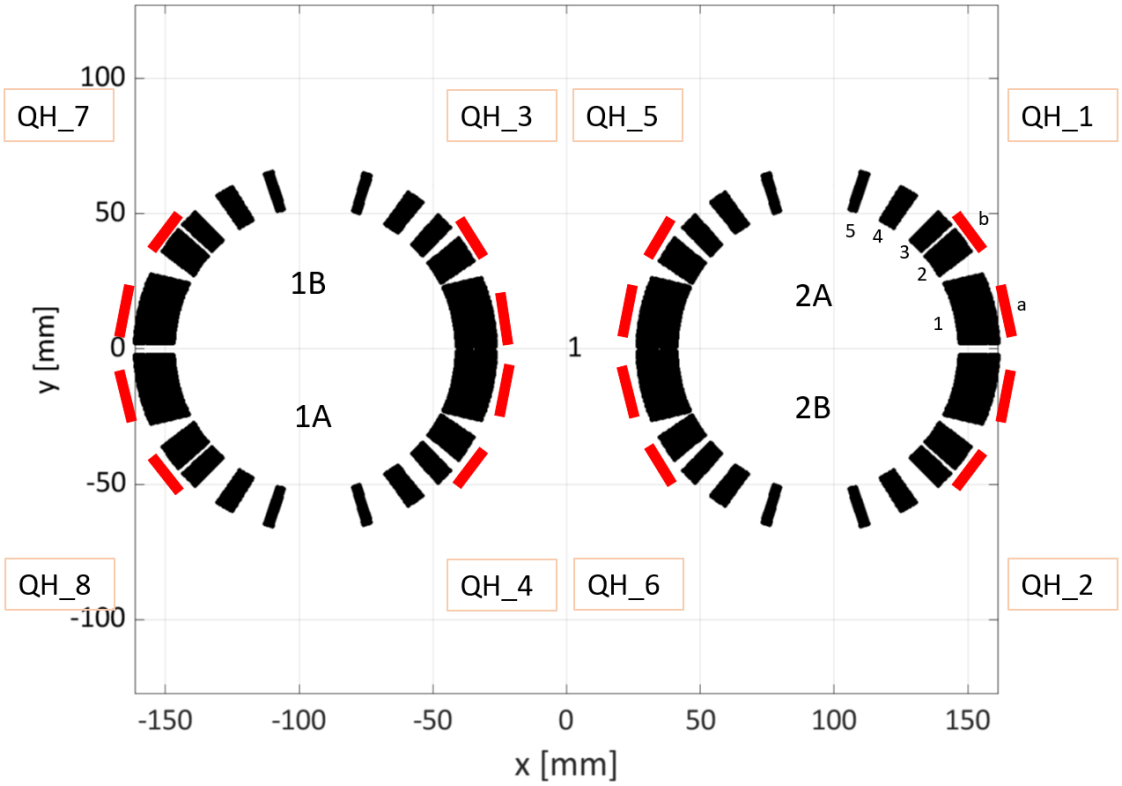

Figure 4.1: Cross-section of the MBRD short model, showing the 8 existing QHs (QH1, QH2, QH3, QH4, QH5, QH6, QH7 and QH8) in their order including the two strips (a and b). The two apertures and four different coils (1A, 1B, 2A and 2B) are indicated as well as the 5 blocks (1, 2, 3, 4, 5) per coil.

The measurements taken during the magnet test and used for the validation process are the magnet current I_{meas}, the currents through the active heaters I_{QH2} and I_{QH5}, the four coil voltages V_{1A}, V_{2A}, V_{1B} and V_{2B} and the voltages for each coil block of coil 2A V_{b1}, V_{b2}, V_{b3},V_{b4} and V_{b5}. All measured and used signals are summarized in Table 4.4.

Measured signals

Signal	Unit	Abbreviation
Magnet current	A	I_{meas}
QH2 current	A	I_{QH2}
QH5 current	A	I_{QH5}
Voltage coil 1A	V	V_{1A}
Voltage coil 2A	V	V_{2A}
Voltage coil 1B	V	V_{1B}
Voltage coil 2B	V	V_{2B}
Voltage block 1	V	V_{b1}
Voltage block 2	V	V_{b2}
Voltage block 3	V	V_{b3}
Voltage block 4	V	V_{b4}
Voltage block 5	V	V_{b5}

Table 4.4: Measured signals and their names for MBRD, which are used for the validation process.

In all tests a quench is induced by firing the quench heaters, which leads to a decreasing time period between QH triggering and quench detection with increasing current, as it takes less external energy at high currents to quench the magnet. The resistance of the EE and operating temperature stay constant at 40 mΩ and 1.9 K, respectively.

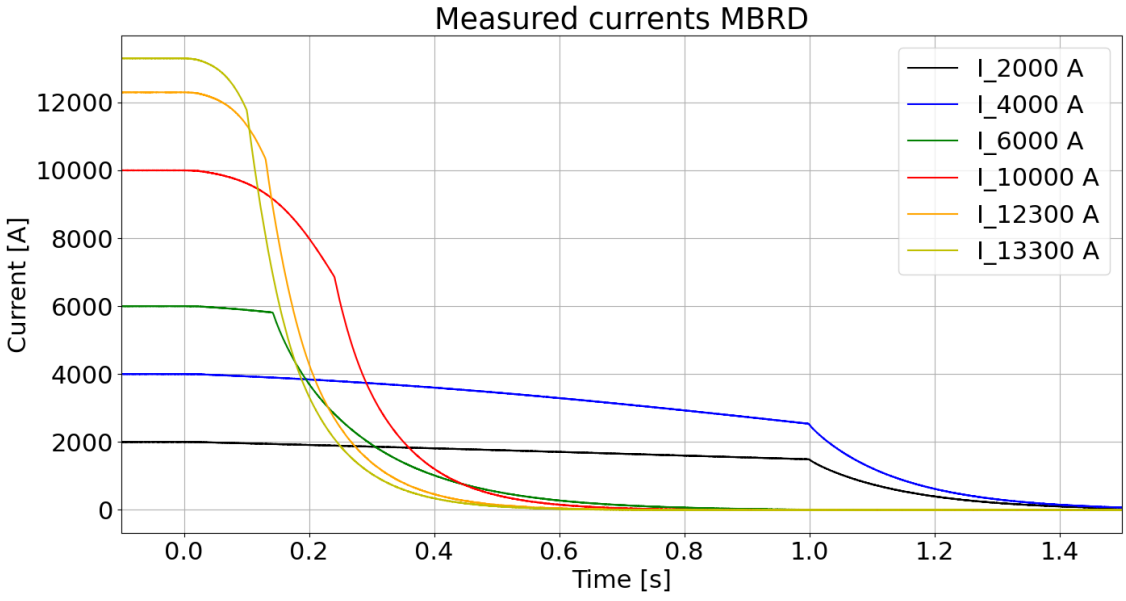

Figure 4.2: Measured currents for all discharges performed for the MBRD magnet. The lowest current lies at 2000 A while the highest currents are 12300 A and 13300 A, which are the nominal and ultimate current of the magnet, respectively. An EE is triggered for every current level at different times, as shown in Table 4.3. After the EE is triggered the speed of the current discharge increases dramatically.

While the currents between 2000 A and 10000 A increase in steps of 2000 A, a test with 8000 A has not been performed. All measured currents are shown in Figure 4.2.

4.2 Adaptation of the model

Before starting to vary the previously described parameters, the circuit of the magnet and the QH circuits need to be adapted to the measurements. In Figure 4.3 the measurement of the voltage across the magnet circuit is shown, not showing the voltage across the power supply and the magnet. A detailed representation of the circuit is shown in Figure 2.3. During operation the power supply applies a voltage aimed at maintaining a constant current through the magnet. When a quench is detected, the power supply switches off and the current commutes to the crowbar in parallel to the power supply. Thus, the measured voltage consists of the resistive voltage across the warm parts of the circuit $R_{Circuit}$, the resistive voltage across the crowbar resistance $R_{Crowbar}$, and the voltage drop across the crowbar diode $U_{Crowbar}$. $R_{Crowbar}$ is very small compared to $R_{Circuit}$ for this magnet and can be neglected. The dashed red line in Figure 4.3 shows the expected behaviour if the power supply switches off when the quench is detected at 0 s. In the case of the measurements for the MBRD short model, the power supply got switched off 20 ms after the quench detection leading to the shown black curve. Thus, the power supply is switched off with a 20 ms delay in the simulation as well. A maximum power supply voltage of 5 V is set between 0 s and 20 ms to simulate the fact that the power supply voltage is not updated instantaneously, and remains unchanged during the $0 < t < 20$ ms time window. As a result, the magnet current decreases during this part of the transient.

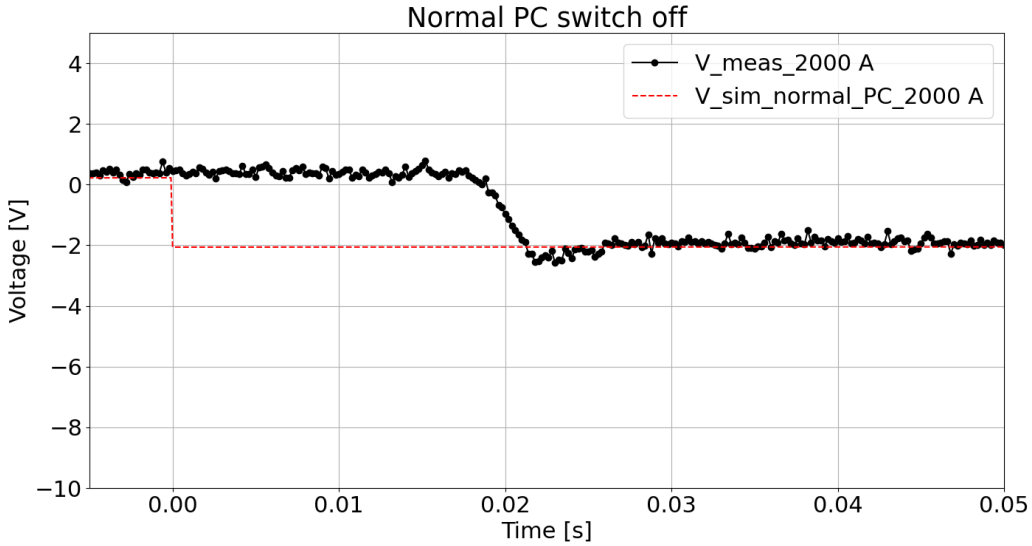

Figure 4.3: In black the measured voltage across the magnet is shown. In red the simulated voltage is shown for the case of the usual switch off of the power supply at 0 s.

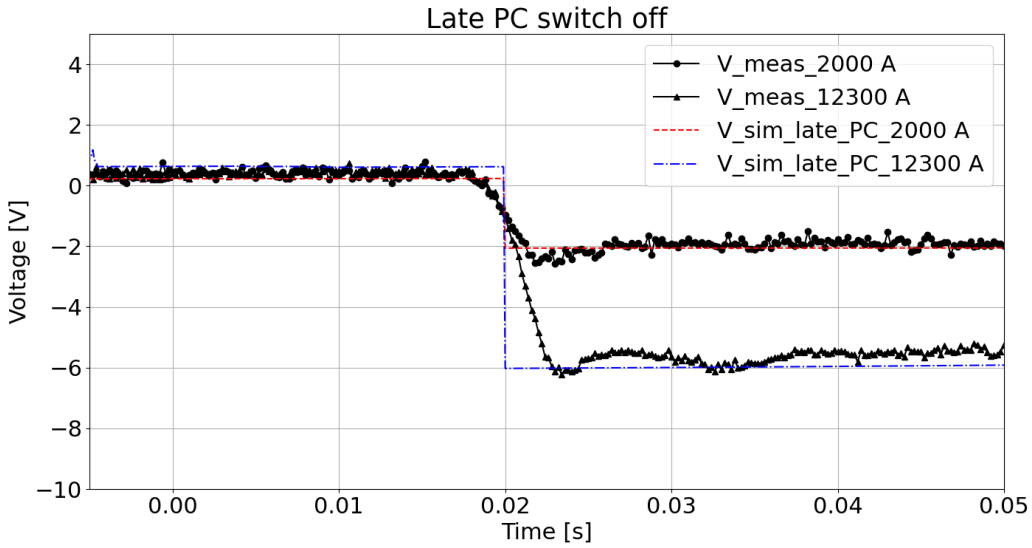

Figure 4.4: In black the measured voltage across the magnet at 2000 A and 12300 A are shown. The red curve shows the simulated voltage at 2000 A and the blue accounts for the voltage at 12300 A, both with a power supply switch off at 20 ms.

To also match the voltage after switching off the power supply, $R_{Circuit}$ and $U_{Crowbar}$ need to be set correctly. Using the measured voltages for 2000 A and 12300 A after the power supply switch off shown in Figure 4.4 and following equations the values for $R_{Circuit}$ and $U_{Crowbar}$ can be calculated:

$$U_{measured1} = U_{Crowbar} + I_1 \cdot R_{Circuit} \tag{4.1}$$

$$U_{measured2} = U_{Crowbar} + I_2 \cdot R_{Circuit} \tag{4.2}$$

With $U_{measured1}$ and $U_{measured2}$ at 2 V and 5.7 V, respectively, $U_{Crowbar}$ of 1.28 V and $R_{Circuit}$ of 360 $\mu\Omega$ can be found. The simulated voltages obtained with these values are also shown in Figure 4.4.
For the correct design of the QHs, different parameters have to be known. All parameters of the QHs used for the MBRD short model are given in Table 4.5. While the capacitance of the capacitor bank connected to the heaters, the width, height, length, insulation thickness and amount of heating stations are known, the QH voltage and current slightly deviate from the baseline values and need to be measured.

QH parameters of the MBRD short model

Parameter	Unit	Value
QH voltage per strip	V	460
Peak current QH 2 / 5	A	159 / 148
QH capacitor	F	0.0141
Resistance of warm parts of QH 2a / 2b / 5a / 5b	Ω	2.46 / 2.43 / 2.61 / 2.58
Width of QH strip a / b	m	0.02 / 0.015
QH height	μm	25
QH length	m	1.378
QH heating stations		3
QH insulation thickness	μm	100

Table 4.5: Parameters of the QHs used for the MBRD short model. Most are known or measured, but the warm resistance of the QH circuit needs to be calculated.

From the known and measured parameters, the resistance of the warm parts of the heater circuit R_{warm} for each heater strip can be calculated with following equation:

$$I_{QH} = \frac{U_{QH}}{R_{geom} + R_{warm}} \tag{4.3}$$

With U_{QH} being the voltage across one heater strip, I_{QH} representing the current through one QH and R_{geom} being the resistance of the stainless steel parts of the heater depending on their geometry, while neglecting the copper parts of the QH. The warm parts of the QH circuit are those not in contact with the magnet and therefore not cooled to 1.9 K. The two strip types a and b of the QHs have different geometries and the measured peak current varies between the two used heaters. R_{warm} of each strip is different and given in Table 4.5.
When using the calculated and known parameters in a LEDET simulation, the discharge of the capacitor bank through the QH strips can be simulated and is shown in Figure 4.5 for QH2 and in Figure 4.6 for QH5. In both cases the peak current and the discharge is simulated sufficiently well. Technically the current through strips a and b are separately simulated in LEDET and could differ from each other. In the shown cases the difference is negligible and only one QH current is shown.

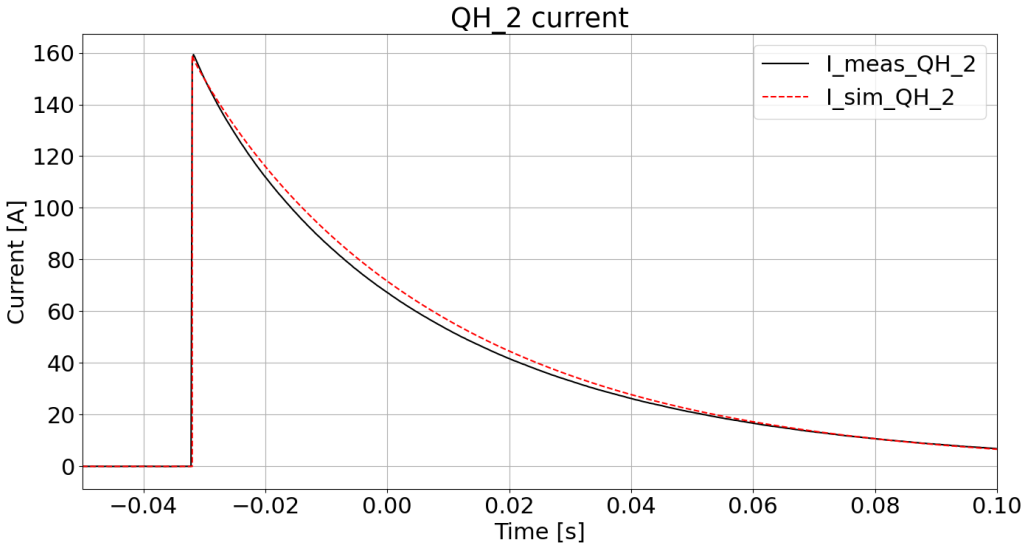

Figure 4.5: The black curve shows the measured current through QH2. In red the simulated current through strip a of QH2 are shown.

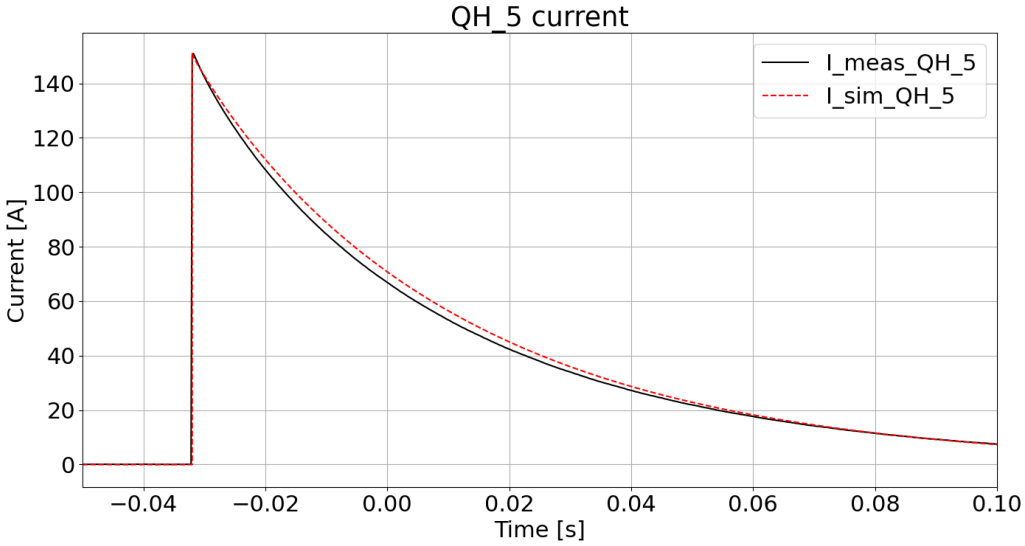

Figure 4.6: The black curve shows the measured current through QH5. In red the simulated current through strip a of QH5 are shown.

An information of paramount importance regarding the QHs is their placement and most importantly which exact half-turns are in thermal contact with the QH strips. The placement highly influences the magnet discharge, especially in the moment just after triggering the QHs, as it induces enough heat to quench all half-turns which are touched in a relatively short time period. To distribute the heat of the QHs as evenly as possible across the magnet in order protect it efficiently, as many separate blocks of the coils as possible should be in contact with a heater strip. The turns of each block

that are in thermal contact with QH strips are listed in Table 4.6. The information about which half-turn is placed in which block of the magnet is given in the Annex in section 6.1 in Figure 6.1 and Table 6.1.
For the MBRD short model, strip a of QH 1 and 2 is in contact with 11 half-turns of block 1. In case of QH 5 and 6 only 10 half-turns of block 1 are touched by strip a. Strip b of all QHs are in contact with blocks 2 and 3. Due to the asymmetry of the magnet strips b of QH 1 and 2 touch six and one half-turns in block 2 and 3, respectively. Strips b of QH 5 and 6 in comparison touch four and two half-turns in block 2 and 3, respectively.

QH placement for aperture 2

QH strip	Block 1	Block 2	Block 3
QH 1a	4, 5, 6, 7, 8, 9, 10, 11 12, 13, 14		
QH 1b		16, 17, 18, 19, 20, 21	22
QH 2a	159, 160, 161, 162, 163, 164 165, 167, 168, 169		
QH 2b		171, 172, 173, 174, 175, 176	177
QH 5a	129, 130, 131, 132, 134, 135 136, 137, 138, 139		
QH 5b		142, 143, 144, 145	146, 147
QH 6a	37, 38, 39, 40, 41, 42 43, 44, 45, 46		
QH 6b		49, 50, 51, 52	53, 54

Table 4.6: Half-turns and blocks of the MBRD short model, which are in contact with one of the heater strips. Through its asymmetry, depending on which coil they are placed the QHs are in contact with a different amount and pattern of half-turns.

4.3 Parameter variation

With the geometric parameters of the magnet, the previously described circuit, the known EE and QH parameters, the magnet transient can be simulated. A few parameters still remain unknown and need to be found through a validation process. As the consecutive simulation of PyBBQ and LEDET allows considering the longitudinal quench propagation velocity v_q, influencing the speed of the discharge, the best guess for the $wetted_p$ in the PyBBQ simulations needs to be found. To determine v_q an average velocity between two points along the conductor is taken. In this thesis these points lie at 50 and 51 % of the conductor length. At 50 % of the conductor length a stable v_q is simulated in the considered current range and a reasonable simulation time can be achieved by setting the second point at 51 %.
Another crucial, unknown parameter is $f_{internal,voids}$, which strongly influences when a quench starts in the cable, due to the high heat capacity of the helium. $f_{internal,voids}$ also influences the speed of the discharge, since it also affects how quickly the turns that are not in contact with QH are transferred to the normal state. As block 4 and 5

of each coil are not touched by QHs, the main driver to their normal-state transition are coupling losses during the discharge. The parameters R_c (influencing ISCC) and f_{eff} (influencing IFCC) can be adapted to obtain the desired behaviour concerning the coupling losses.
In order to find the best fitting $wetted_p$ a variation between 0.3 and 0.7 is carried out for the current levels 4000 A, 6000 A and 10000 A. These values for $wetted_p$ are chosen as, due to geometry restrictions of a Rutherford cable, only a certain amount of strand surface can either be touched by helium or insulation. The chosen current levels represent the middle range of the magnet current, as previous simulations had shown the largest impact of $wetted_p$ at these current levels. To simulate v_q in PyBBQ a power pulse at one end of the conductor is induced. This approach is the easiest to implement and is adequate to simulate v_q at most current levels.
In Figure 4.7 the measured and simulated discharge currents for the 4000 A case are shown. The used values of $wetted_p$ higher than 0.3 lead to the same simulated discharge, which is significantly slower than the measured one. PyBBQ simulates $v_q > 0$ for $wetted_p$ at 0.3 and $v_q <= 0$ for all cases above 0.3. At 4000 A the simulated curve in red fits the measurement very well. In Figure 4.8 the measured and simulated differential voltage U_{diff} between aperture 2 and 1 is shown. U_{diff} develops from the moment when a quench occurs in aperture 2. As at the beginning of the discharge no quench is developing in aperture 1, it develops inductive voltages of equal polarity to aperture 2 and discharges through the developing resistance in aperture 2. U_{diff} increases until the EE is triggered, after which it decreases sharply for discharges at low currents. For discharges at higher currents a voltage jump occurs when EE is triggered and thereafter U_{diff} can still increase slightly before it decreases less sharply than for discharges at low currents. U_{diff} is very sensitive in displaying the start of the quench and can be used as another indication that the simulation models the behavior of the magnet well. For the case of the 4000 A discharge, again no visible change in the behavior of the simulated U_{diff} can be seen for $wetted_p$ above 0.3, while the simulation indicates a very slow voltage increase compared to the measured voltage. For $wetted_p$ at 0.3 a slight overestimation of U_{diff} can be seen.

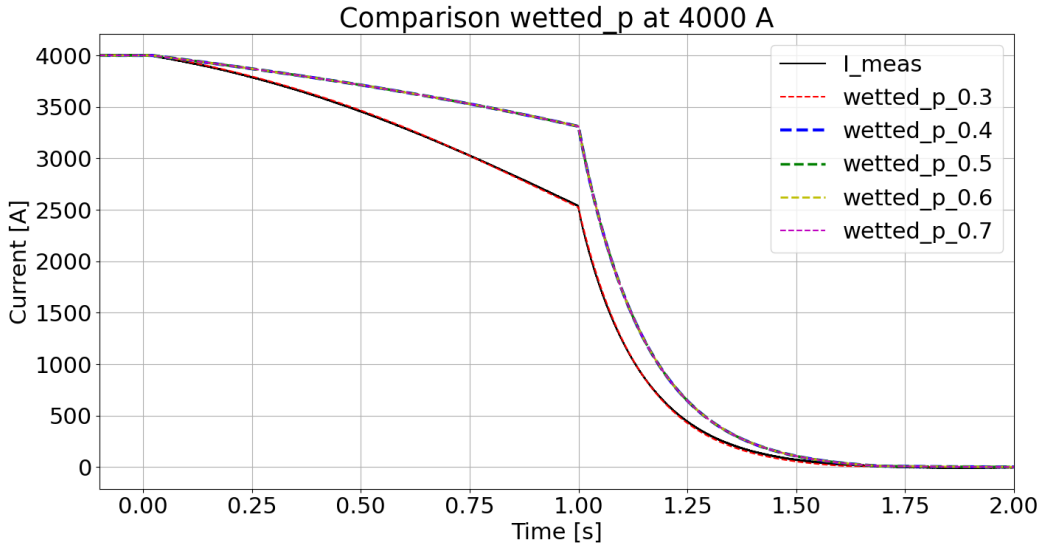

Figure 4.7: Comparison of the measured magnet current for an initial current of 4000 A in solid black and a simulated sweep over $wetted_p$ from 0.3-0.7 shown as dashed colored curves.

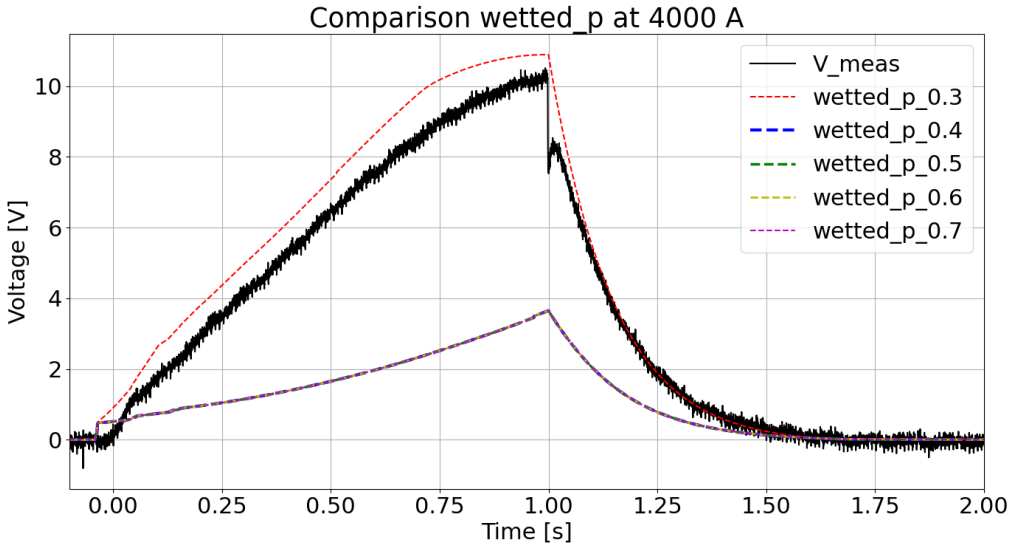

Figure 4.8: Comparison of the measured differential voltage for an initial current of 4000 A in solid black and a simulated sweep over $wetted_p$ from 0.3-0.7 shown as dashed colored curves.

Figure 4.9 shows the measured and simulated discharge at 6000 A varying $wetted_p$ in the simulation. For decreasing $wetted_p$ v_q increases and the simulated discharge accelerates as well. For all values below 0.7 for $wetted_p$ a faster discharge compared to the measurement can be seen, while the curve using 0.7 matches the measured curve very well. The same pattern is visible in Figure 4.10 showing U_{diff} for different values

of $wetted_p$. With the lower values leading to high simulated voltages the simulation using 0.7 for $wetted_p$ fits the best, but still overestimates the voltage.

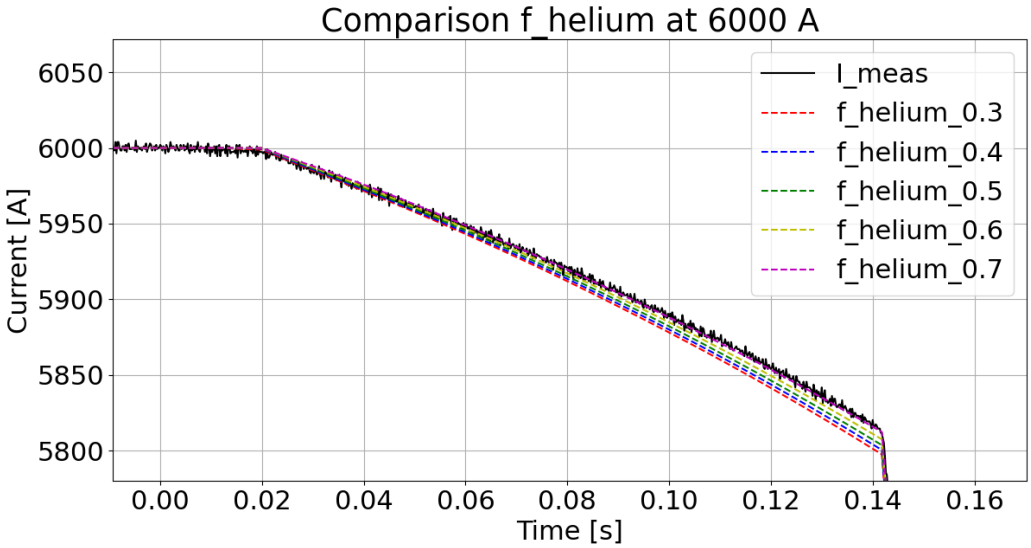

Figure 4.9: Comparison of the measured current for an initial current of 6000 A in solid black and a simulated sweep over $wetted_p$ from 0.3-0.7 as dashed colored curves.

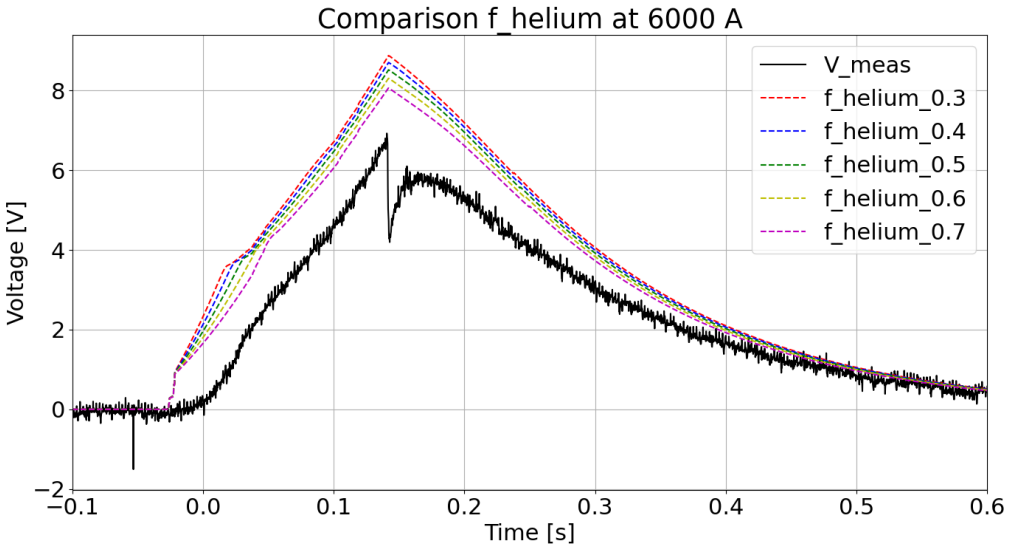

Figure 4.10: Comparison of the measured differential voltage for an initial current of 6000 A in solid black and a simulated sweep over $wetted_p$ from 0.3-0.7 as dashed colored curves.

For the discharge at 10000 A, the variation of $wetted_p$ has virtually no impact on the behavior of the simulated discharge shown in Figure 4.11 as well as on U_{diff} shown in Figure 4.12.

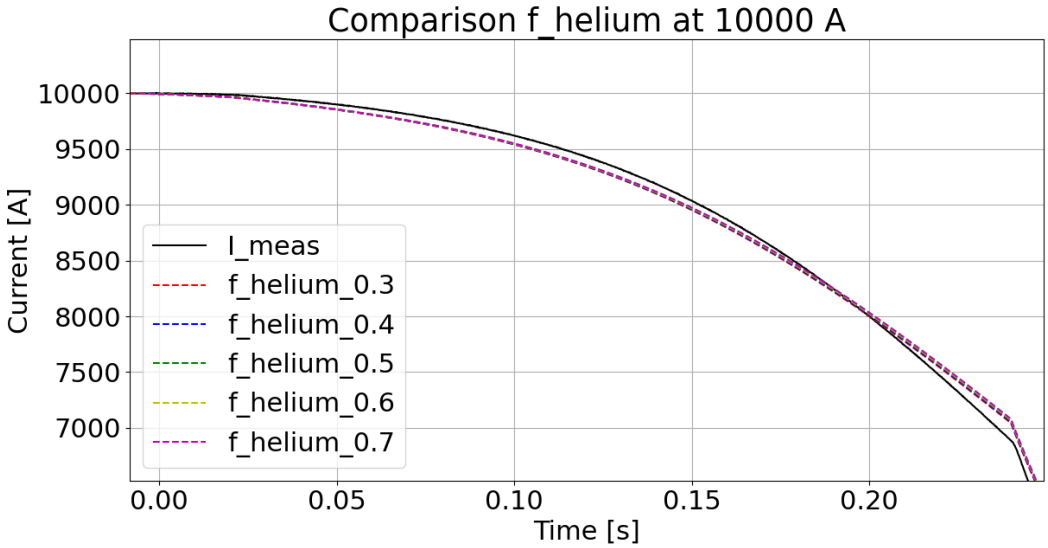

Figure 4.11: Comparison of the measured current for an initial current of 10000 A in solid black and a simulated sweep over $wetted_p$ from 0.3-0.7 as dashed colored curves

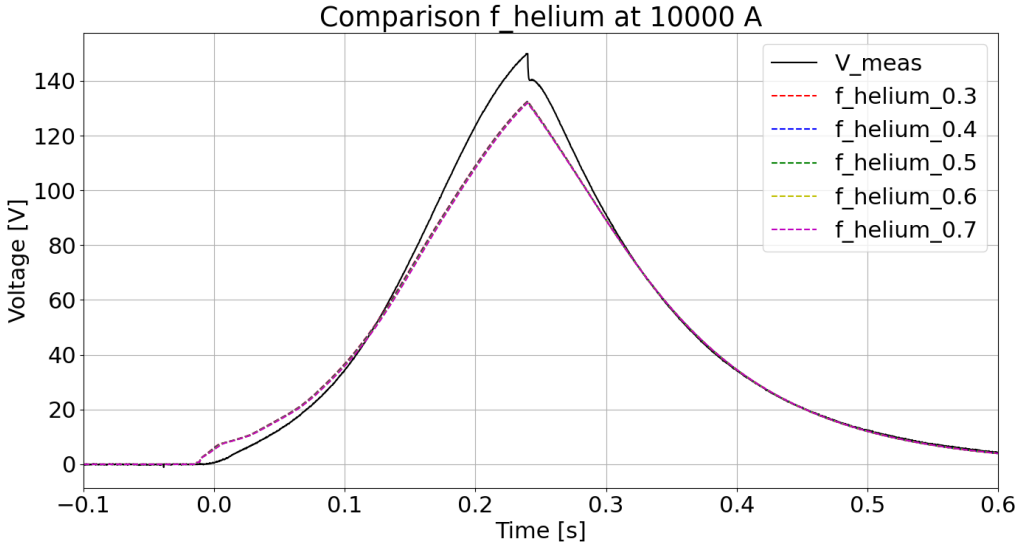

Figure 4.12: Comparison of the measured differential voltage for an initial current of 10000 A in solid black and a simulated sweep over $wetted_p$ from 0.3-0.7 as dashed colored curves.

As simulations at 4000 A suggest significantly lower values for $wetted_p$ than at 6000 A the low current cases need to be investigated more. This is supported by the fact that no v_q is simulated at 4000 A for a wide range of values for $wetted_p$. As the impact of $wetted_p$ is negligible at high currents the final value can be chosen based on the discharges shown in Figure 4.9, but needs to be confirmed by further simulations at low currents. This leads to a preliminary fixed value of 0.7 for $wetted_p$.
As shown in Figure 2.12 a value of 0.7 for $wetted_p$ at 4000 A leads to PyBBQ simulating

$v_q <= 0$. This only changes with very low values for $wetted_p$. Taking into account the poor fit for most values and the fact that the simulation of v_q is the most challenging at the edge between a quench in the cable and recovery of the superconducting state, v_q needs to be investigated more at low currents. When the induced power pulse in PyBBQ is not sufficient to initiate a propagating quench, no v_q is calculated. The temperature profile along the conductor at certain time steps is shown in Figure 4.13 for an operating current of 4000 A. Figure 4.13a shows the profile for the case of a power pulse at the beginning of the conductor for a simulation time of 80 ms. First the quench starts propagating up to 0.075 m, indicated by the dark purple lines, after which the cable recovers with decreasing temperature to end at 1.9 K, indicated by the yellow line. This leads to a simulated $v_q <= 0$. Figure 4.13b shows the temperature profile for a conductor with an active QH heating station in contact with the first 0.0675 m of the conductor for a simulation time of 300 ms. After the QH is triggered, the same discharge process described in section 4.2 is implemented, with an exponentially decreasing power deposited into the conductor. To keep the same conductor length where the quench propagates, the length of the heating station is added to the total length of the simulated conductor. By doing so the temperature profile changes and it can be seen that the quench is propagating significantly further than with using a power pulse, which leads to a simulated $v_q > 0$. The energy transferred to the conductor is 16.2 $\frac{\mathrm{J}}{\mathrm{cm}^3}$ when implementing the QH in a time-period of 100 ms, while the power pulse only deposits 3.88 $\frac{\mathrm{J}}{\mathrm{cm}^3}$ in a time-period of 15 ms. The area where the QH is in thermal contact to the conductor also exceeds the area where the power pulse is initiated. The larger and wider heat input through a QH can lead to increasing temperature along the conductor. This means that a quench is propagating through the cable not only driven by ohmic loss but also by heat diffusing from the QHs. The improved quench-initiation assumptions result in a better fit between simulated and measured results at low currents.

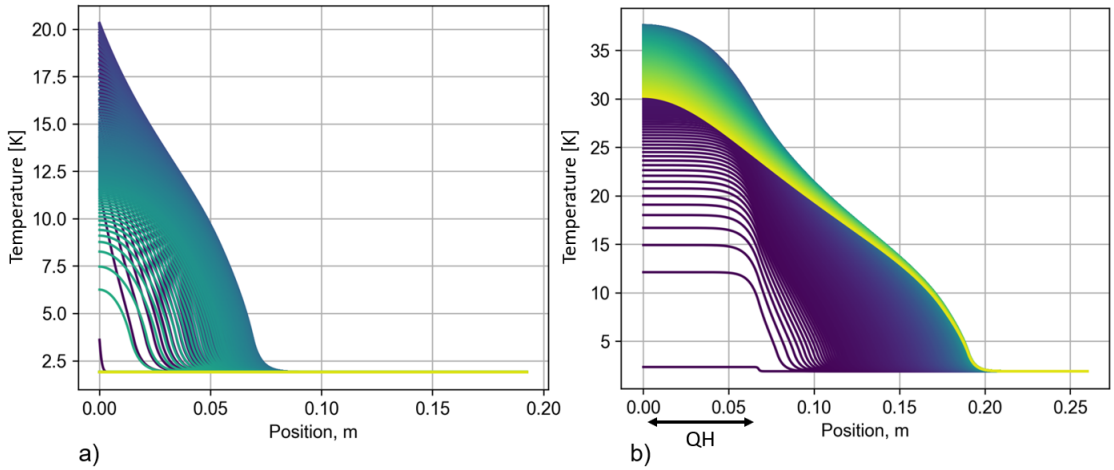

Figure 4.13: Temperature profile along a part of the conductor of the MBRD magnet at a current of 4000 A simulated with PyBBQ [30]. a) shows the temperature profile when a power pulse at the beginning of the conductor is induced. b) shows the temperature profile when a heating station of a QH is implemented. The length of the heating station is added to the total length of the simulated conductor. The temperature profile is taken for certain time steps during the simulation, which is indicated by the color change from dark purple to yellow.

To further support the selection of the value 0.7 for $wetted_p$ Figure 4.14 shows the discharge at 4000 A with $wetted_p$ between 0.6 and 0.8. The previously chosen value of $wetted_p$=0.7 at 6000 A leads again to the best fit. The implementation of heating stations in PyBBQ only has an effect on the low current cases. Already at 6000 A the effect is negligible, hence the simulations shown before for current levels above 4000 A are still valid.

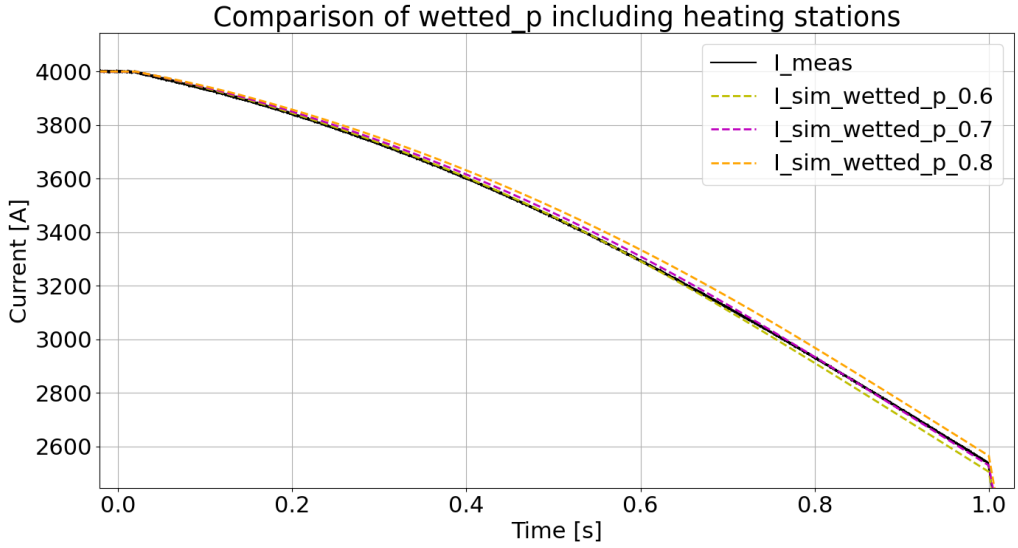

Figure 4.14: The plot shows the impact of $wetted_p$ for the 4000 A discharge including heating stations in the PyBBQ simulation.

To show the positive effect of the resulting low, but non zero, v_q at low currents the 2000 A and 4000 A discharges are shown in Figure 4.15. The simulated curves, shown in Figure 4.15 and Figure 4.16, fit very well to the measured current and U_{diff}. As reference, the simulated curves with $v_q = 0$ are shown in both plots in dashed orange and green. As both simulations use a value of 0.7 for $wetted_p$, which is considered as confirmed and will be used in all future simulations in this thesis.

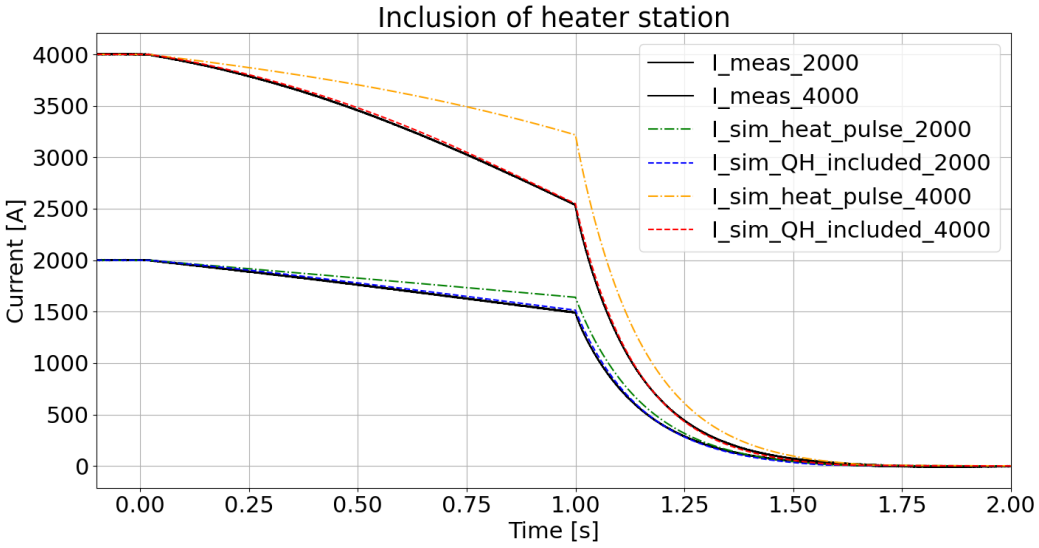

Figure 4.15: In solid black the measured currents for the initial currents of 2000 A and 4000 A are shown. The dashed yellow and green curves show the simulated discharge currents using LEDET taking into account no v_q at low currents as calculated by PyBBQ initially. The dashed red and blue curves show the magnet current including the effect of heat diffusion along the cable simulated by PyBBQ.

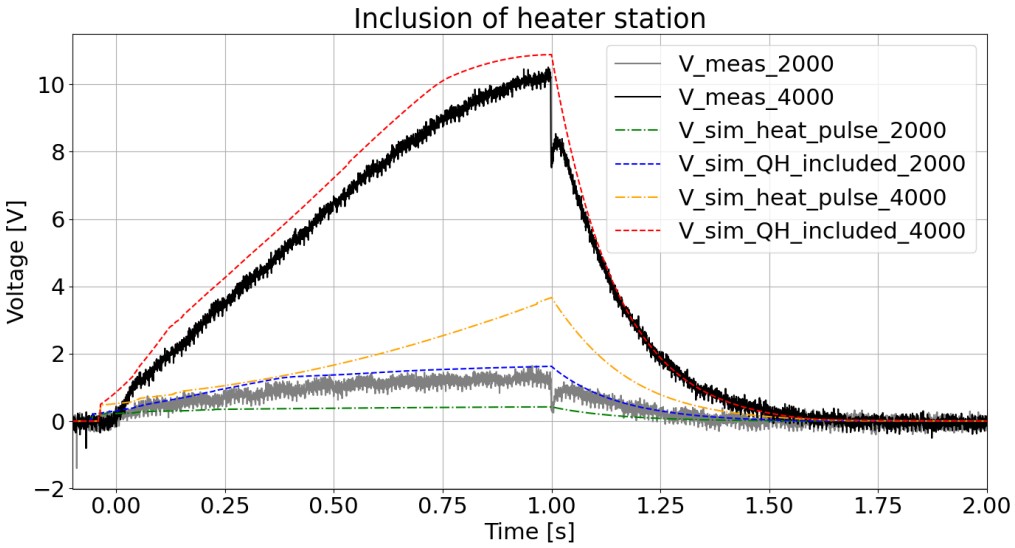

Figure 4.16: In solid grey the measured differential voltage for the initial current of 2000 A and in black for 4000 A are shown. The dashed yellow and green curves show the simulated differential voltages using LEDET taking into account no v_q at low currents as calculated by PyBBQ initially. The dashed red and blue curves show the differential voltage including the effect of heat diffusion along the cable simulated by PyBBQ.

The v_q for all current levels simulated by PyBBQ including a QH and with a power pulse as well as the v_q calculated by the analytical formula included in LEDET are given in Table 4.7. The shown values are obtained with $wetted_p$ at 0.7.

Comparison of simulated and calculated v_q

Current level [A]	**Including QH $[\frac{m}{s}]$**	**Power pulse $[\frac{m}{s}]$**	**Analytical calculation $[\frac{m}{s}]$**
2000	0.39	0	1.16
4000	0.94	0	2.61
6000	2.24	2.24	4.44
10000	9.64	9.64	9.75
12300	15.1	15.1	14.35
13300	17.86	17.86	16.87

Table 4.7: The values of v_q simulated by PyBBQ including the QHs or a power pulse are given in the second and third column for each current level. v_q calculated with the analytical formula included in LEDET is given in the last column.

To highlight the improvements which can be achieved by including a 2D+1D feature and furthermore including PyBBQ into a consecutive simulation a 2D, 2D+1D and consecutive simulation results are compared to measurement in Figure 4.17 for the 4000 A case. The dotted red line shows a simple 2D approach, which simulates the discharge significantly too slow. In comparison the 2D+1D approach, simulates a faster discharge compared to the measurement. The 2D+1D LEDET simulation that adopts the v_q calculated with PyBBQ leads to an excellent fit with the measurement.

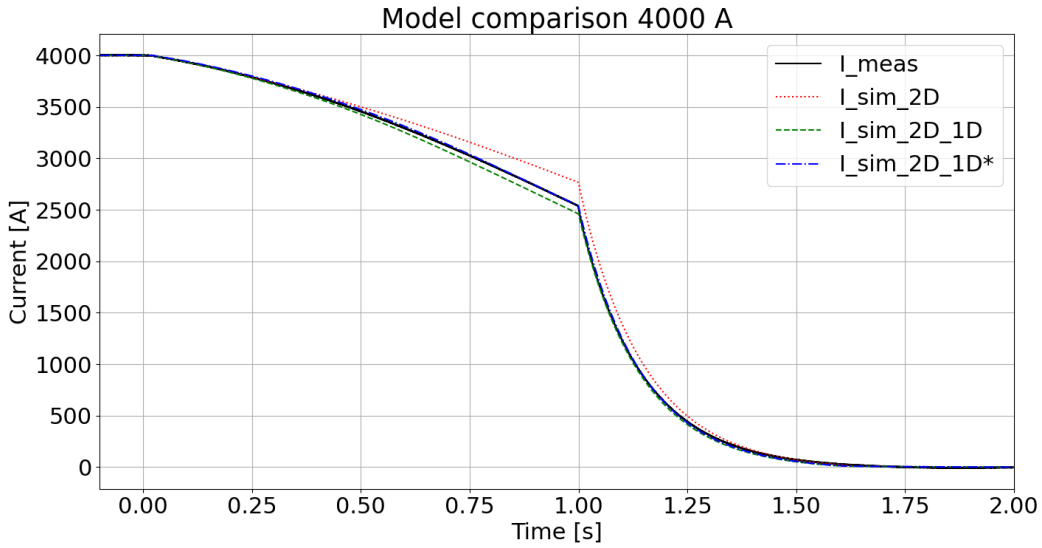

Figure 4.17: The black curve shows the measured discharge current for an initial current of 4000 A. The red dotted line shows the current simulated with a 2D LEDET model. In green (dashed) a 2D+1D extension is introduced, which takes longitudinal quench propagation into account. The blue curve also includes the 2D+1D extension, but includes the effect of helium cooling inside the cable, which decreases the speed of the discharge.

To further improve the simulation of the discharges of the MBRD short model, $f_{internal,voids}$ can be adapted to match the simulated start of the quench in the magnet to the measurements. The currents chosen for the validation are the nominal 12300 A and 4000 A. The signal used to determine the start of the quench is U_{diff} as it is the most sensitive to the quench onset. The criterion to determine the quench onset uses the first time step when U_{diff} reaches 20 mV as this voltage lies above the observed fluctuations of the measurement. To support the found value for a matching quench start, the current discharge and the peak value of U_{diff} are used. Three simulations with $f_{internal,voids}$ at 1, 2 and 3 % were performed, these values are low for a Rutherford cable but showed the best agreement in the shown validation process.
In Figure 4.18 the three simulation cases are shown. For the nominal current a measured quench start is found at -8 ms. For a value of 1 % for $f_{internal,voids}$ the quench start is simulated at -13 ms. In case of $f_{internal,voids}$ at 2 %, the start of the quench is matched, while for 3 % it is simulated at -4 ms. As it can be seen for all the simulations, the simulated voltage increase in the first 15 ms of the quench is too fast. Also the shape is more stepped compared to the measured steady increase. The strong increase and the voltage steps of the simulation can be explained by the perfect and uniform contact of the QHs to the half-turns, which is assumed in the simulation and can not be guaranteed during the assembly of the magnet. This leads to a quench of all half-turns in the same coil block in contact to the same heater strip at the same time generating the shown voltage steps. The three pronounced voltage steps at the beginning of the simulated voltage increase in Figure 4.18 are due to the voltages of block 1, 2, and 3, which are in contact to the QHs. One could manipulate the contact area between the

QH and the half-turns to improve the behavior of the simulation, but this would lead to an arbitrary process of choosing which turn should have which contact area.
In order to investigate the impact of varying $f_{internal,voids}$ on the discharge at 12300 A, the previously applied values are used and the results are shown in Figure 4.19. It can be noted that 1 % and 3 % for $f_{internal,voids}$ lead to a faster and slower discharge compared to the measured values, respectively. As already identified for the quench start, the case with 2 % for $f_{internal,voids}$ is the best fit with an RMS error in relation to the peak value of the current (RMS_relative_current) of 2 % for the discharge as well. In case of the global behavior of U_{diff} shown in Figure 4.20, a value of 1 % for $f_{internal,voids}$ leads to the simulation closest to the measurement, especially at the maximum. While U_{diff} is increasing from the quench start to the point when the EE is triggered, the voltage is overestimated around the quench start, but also does not reach the measured peak value of 193 V around the EE triggering. The slope of the discharge after triggering the EE fits considerably better to the measurements than leading up to it.

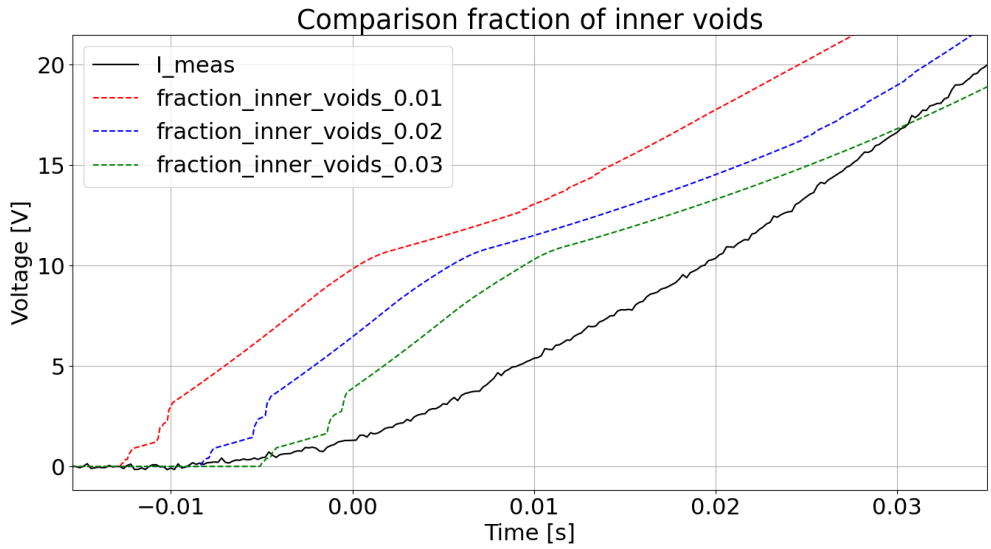

Figure 4.18: In solid black the measured differential voltage for the 12300 A discharge in the time range where it starts increasing as the quench in the magnet develops. The dashed red, blue and green curves show the simulated voltages for 1, 2 and 3 % $f_{internal,voids}$ around the simulated quench start.

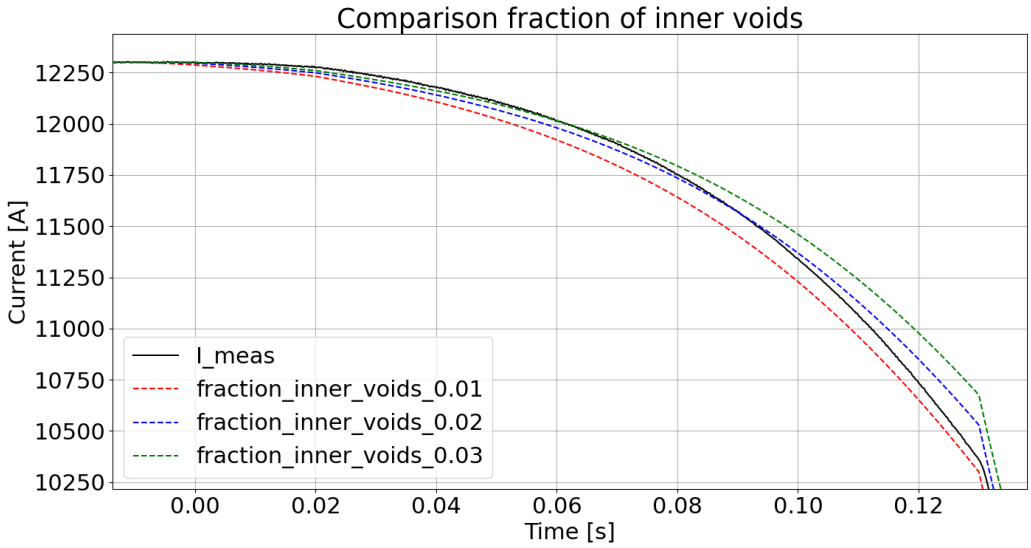

Figure 4.19: Measured discharge at 12300 A in solid black. In dashed red, green and blue simulated discharges at the same current with 1, 2 and 3 % $f_{internal,voids}$, respectively, which influences the speed of the discharge.

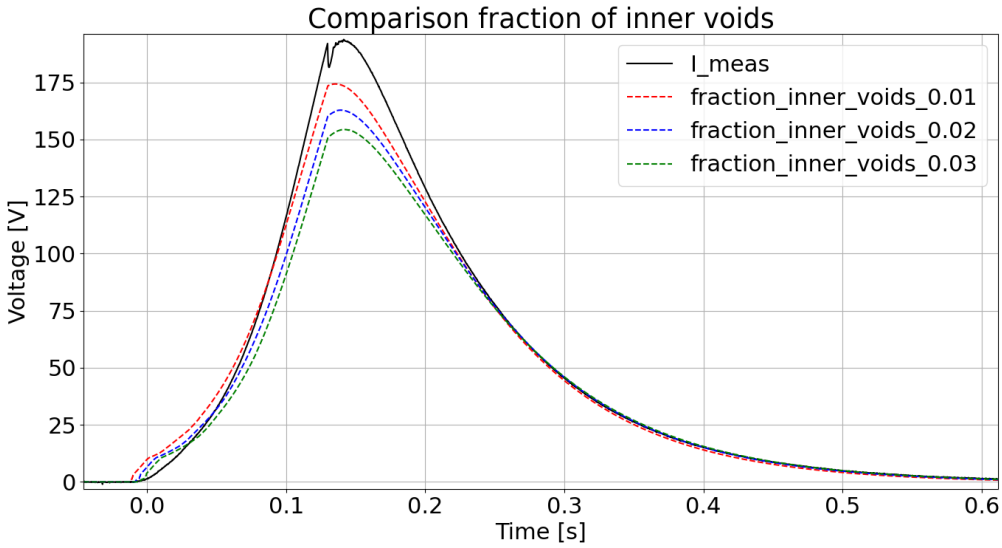

Figure 4.20: The solid black curve shows the measured differential voltage for 12300 A over the full length of the discharge. The dashed red, blue and green curves show the simulated voltages for 1, 2 and 3 % $f_{internal,voids}$, respectively.

Figure 4.21 shows the simulated and measured onset of the quench for the 4000 A discharge. All simulations model the quench too early compared to the measurement while the case with $f_{internal,voids}$ at 3 % being the closest one. Since $f_{internal,voids}$ has a minor impact on the discharge at shown in Figure 4.22 and on the peak differential voltage at 4000 A, the value for $f_{internal,voids}$ can be chosen based on the 12300 A

discharge. With $f_{internal,voids}$ at 2 % the simulation matches best the quench start and fits the discharge sufficiently well This value is chosen for all future simulations in this thesis. Still U_{diff} does not fit well for high current levels. This issue is going to be discussed in section 4.4.

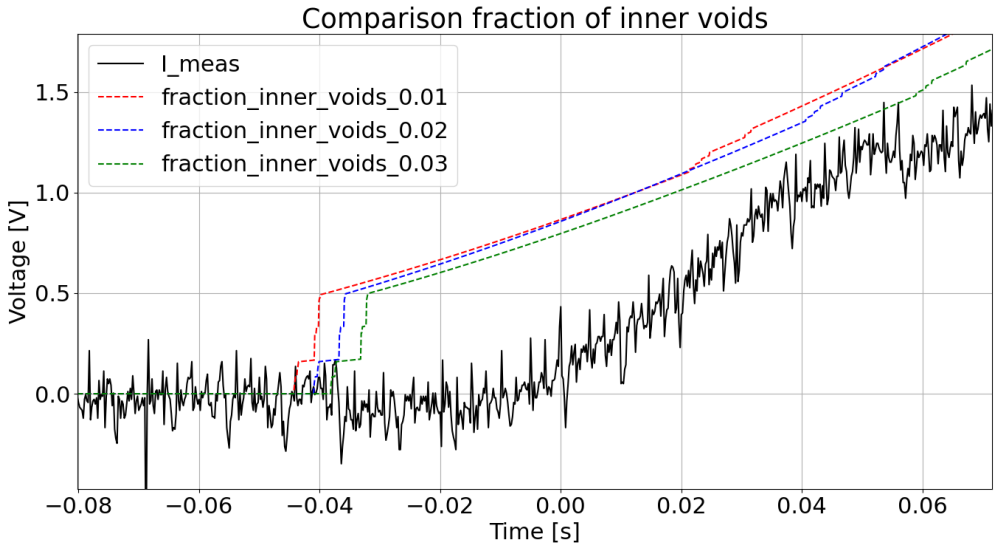

Figure 4.21: In solid black the measured differential voltage for the 4000 A discharge in the time range where it starts increasing as the quench in the magnet develops. The dashed red, blue and green curves show the simulated voltages for 1, 2 and 3 % $f_{internal,voids}$ around the simulated quench start.

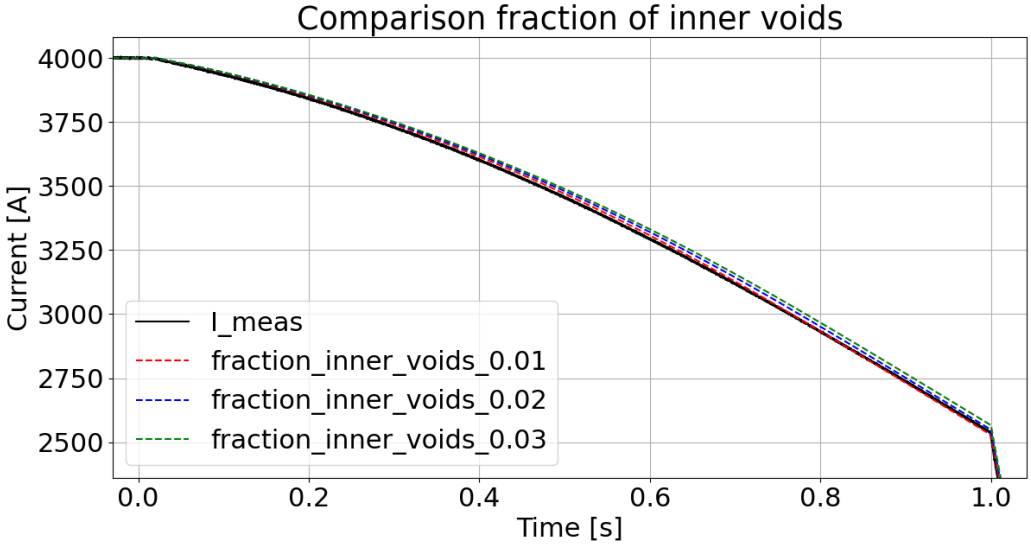

Figure 4.22: Measured discharge at 4000 A in solid black. In dashed red, green and blue simulated discharges at the same current with 1, 2 and 3 % $f_{internal,voids}$, showing minor impact of $f_{internal,voids}$ on the discharge at low currents.

The simulated quench for low currents starts too early compared to the experimental

data. This could be explained by the lack of the third dimension in the LEDET simulation concerning the induced heat of the QHs [54]. The 2D+1D LEDET model does not allow the heat to propagate in the longitudinal direction of the magnet, leading to an overestimation of the temperature in the half-turns in thermal contact with the QH before a quench occurs. Especially at low currents this makes a significant difference in the simulated quench start in the half-turns in thermal contact with the QH. This limitation of LEDET is known and will be addressed in the future. The measured and simulated time difference between quench initiation and quench start in the magnet is shown in Table 4.8, where the divergence for lower currents is clearly visible.

Time difference between QH trigger and quench

Current level [A]	**Simulated difference [ms]**	**Measured difference [ms]**
2000	31	74
4000	29	63
6000	27	43
10000	25	31
12300	24	23
13300	23	20

Table 4.8: Simulated and measured time difference between the QH triggering and the start of the quench in the magnet for each current level.

In the time period between quench onset and EE triggering, coupling currents do not have a big impact on the simulated discharge. After the triggering of the EE, the development of ISCC and especially IFCC can be observed. As the discharge is then dominated by the EE resistance, the variation of f_{eff} and R_c will have a minor impact. A slight improvement of the simulated discharge can be achieved by setting f_{eff} to a value of 2, rather than the default 1. This value is going to be used as R_c stays at its original value of 100 $\mu\Omega$.

4.4 Coil voltage analysis

To analyse the difference between the measured and simulated values for U_{diff} the voltage of each coil of the magnet is shown in Figure 4.23 for the 12300 A discharge. As seen before in Figure 4.20 the voltage is overestimated by the simulation in the beginning, while it underestimates it right before the EE triggering. It is understood that the overestimation at the quench start comes from the QHs but the underestimation can not be explained yet. In Figure 4.24 the coil voltages for the 4000 A discharge are shown. As the simulated coil voltages and U_{diff} for low currents fit quite well to the measurements only the voltages of higher current cases must be analysed.

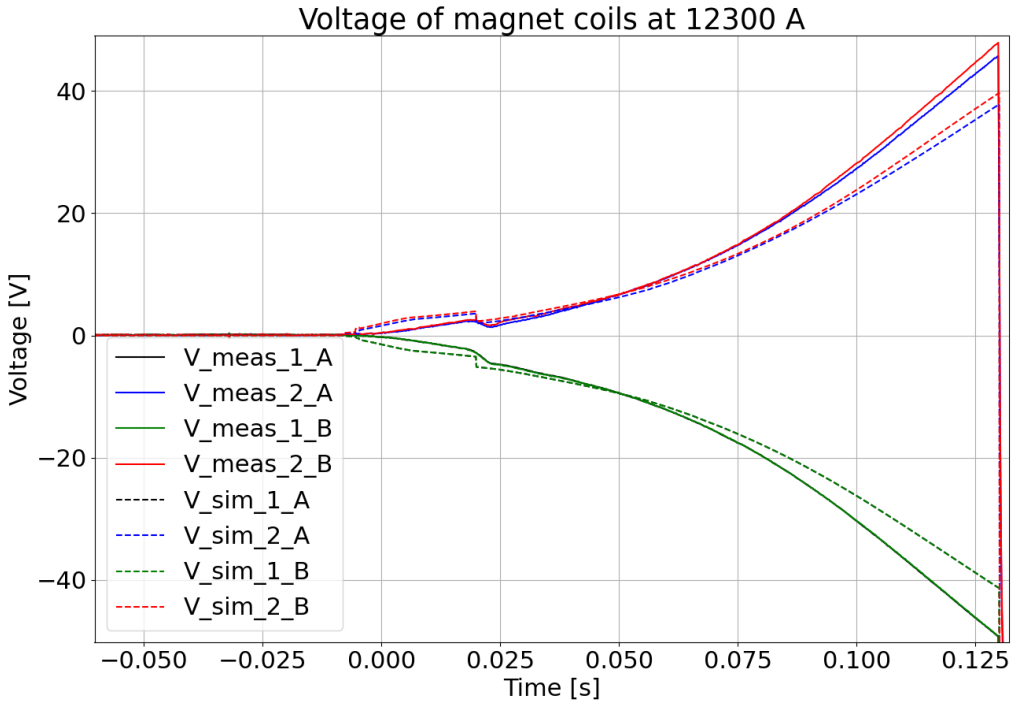

Figure 4.23: The solid blue curve represents the measured voltage across the magnet coil 2A for the 12300 A discharge and the dashed blue line is the simulated voltage for 2A, respectively. In red, black and green the measured voltages for the coils 1A, 1B and 2B are shown, with their simulated counterparts in dashed lines with the same color. The green and black lines lie exactly on top of each other.

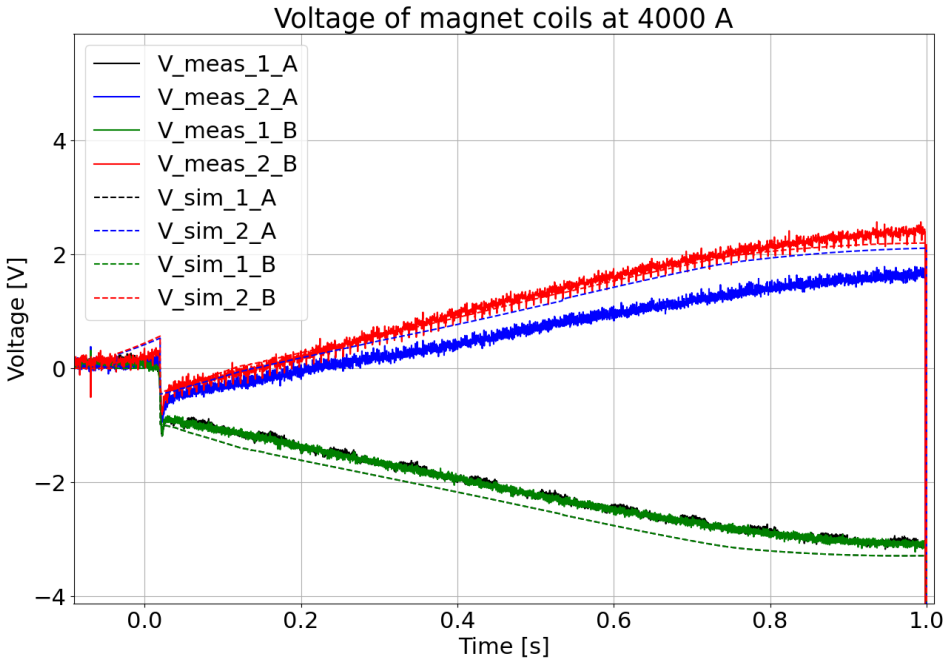

Figure 4.24: The solid blue curve represents the measured voltage across the magnet coil 2A for the 4000 A and the dashed blue line is the simulated voltage for 2A, respectively. In red, black and green the measured voltages for the coils 1A, 1B and 2B are shown, with their simulated counterparts in dashed lines with the same color. The green and black lines lie exactly on top of each other.

To further investigate the difference especially around the EE triggering, the block voltages of coil 2A for the 12300 A discharge are shown in Figure 4.25. For block 1 a strong overestimation of the voltage can be seen at the start of the quench, which then continues less pronounced after the voltage drop due to the power supply switch off. The simulated voltage of block 3 lies below the measurement for the larger part of the discharge, while a small overestimation around the quench start can be noticed. Concerning block 2 a voltage above the measurement is simulated for all time steps until the EE triggering. All described blocks are in contact to the QHs, which explains the overestimation of the voltages in the beginning of the quench. As the developing voltage depends on the temperature increase in each blocks it seems that the temperature in blocks 1 and 2 is increasing too quickly, while it is too slow for block 3. This can be tolerated as the voltage shows similar behaviour as the measurement, but as internal voltages have strong impact on the voltage to ground of the magnet this discrepancy should be kept in mind.
The simulated voltages of blocks 4 and 5 behave very differently compared to the measurements. The simulation models decreasing negative voltages, meaning the quench is not arriving in these blocks and they develop inductive voltages. The measured curves for blocks 4 and 5 suggest increasing voltages at 25 ms and 35 ms which leads to the assumption of the quench arriving in these blocks at the mentioned times.

As blocks 4 and 5 are not in thermal contact to QH they are either quenched by heat transfer from other blocks or by coupling loss. The heat transfer between blocks is mitigated due to extra insulation and copper wedges stabilizing the magnet. Thus, the main course of quench in the blocks 4 and 5 is likely to be coupling loss. Conducted simulations, applying different assumptions concerning the coupling loss in blocks 4 and 5, did not lead to acceptable results. This issue can be addressed in the future to further improve the consecutive simulation model of the MBRD dipole magnet. For the following simulations in this thesis the original model without specific assumptions concerning the coupling loss in blocks 4 and 5 will be used.

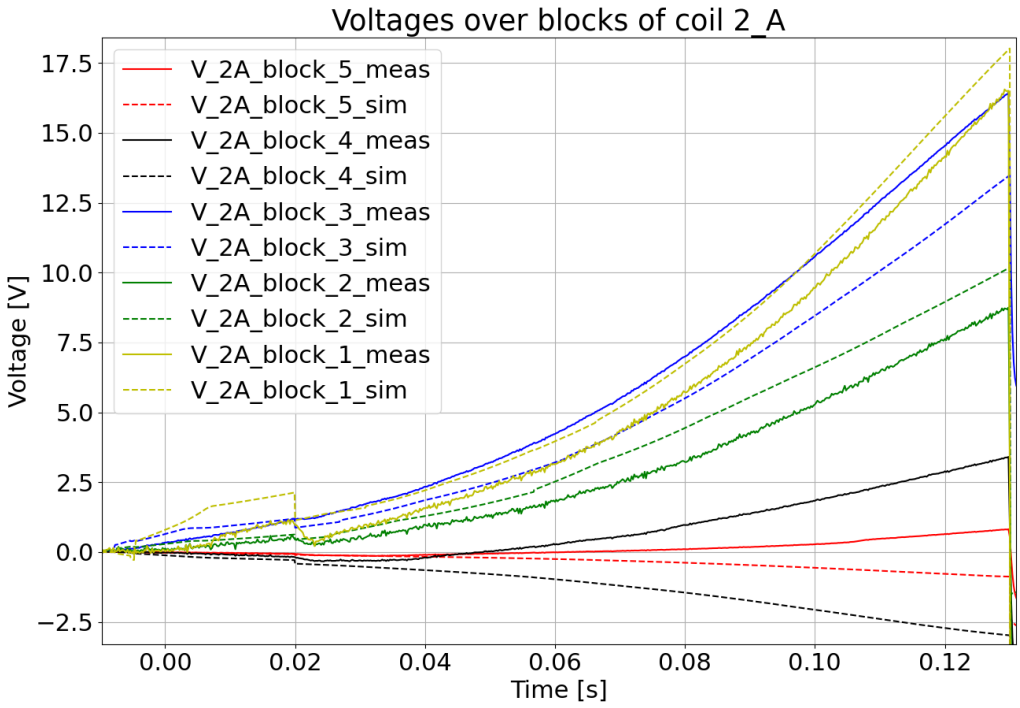

Figure 4.25: In solid yellow the measured voltage across block 1 of coil 2A for the 12300 A discharge is shown. The dashed yellow line represents the simulated voltage for the same block. The green, blue, black and red curves show the measured voltages for block 2, 3, 4 and 5, respectively. The equally colored dashed lines show the associated simulated voltages.

4.5 Summary

An overview of all simulated and measured discharges is given in Figure 4.26 for the MBRD short model. For the three low current cases the simulation and measurement match very well with an average relative RMS_relative_current error of about 1 %. The three high current cases are simulated sufficiently well, while the largest discrepancy occurs shortly before the EE triggering, due to the underestimation of quench in the blocks 4 and 5. The average RMS_relative_current error of the transient is about 2 %.

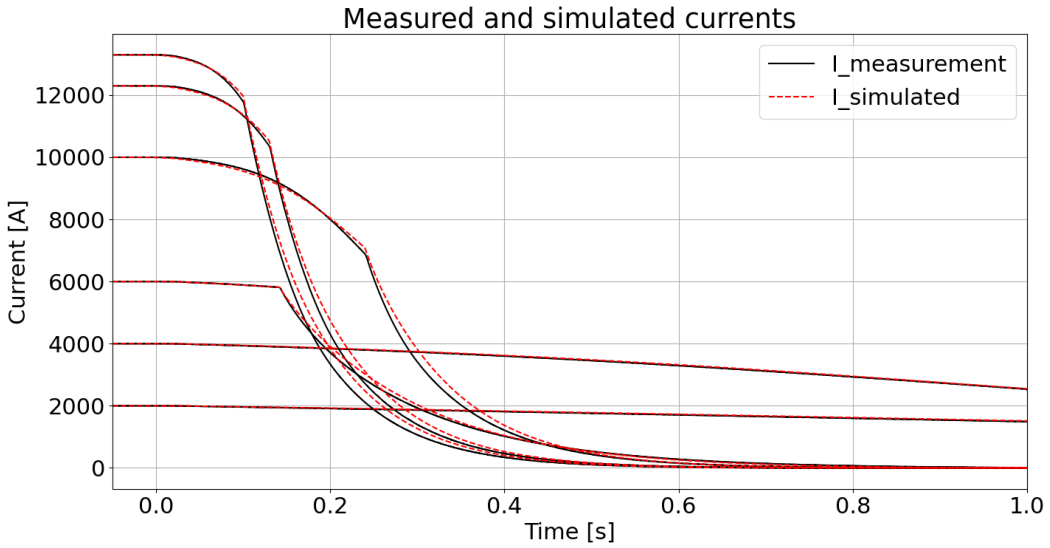

Figure 4.26: Overview of the measured, in solid black, and simulated, in dashed red, discharges at all current levels.

The measured and simulated U_{diff} are shown for the three low current cases in Figure 4.27. In all cases the voltage is slightly overestimated by the simulation with an average RMS_relative_voltage error of about 1 %.
U_{diff} for the three high current cases is shown in Figure 4.28. For high currents the voltage is underestimated, due to no quenches in blocks 4 and 5 of each coil. The average relative RMS_relative_voltage error lies between 5 and 15 %.

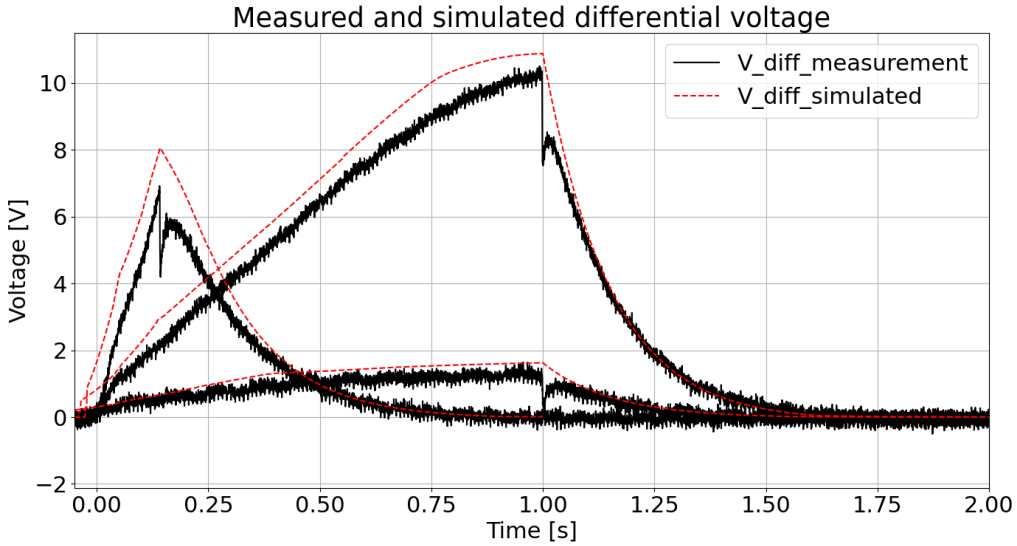

Figure 4.27: Measured and simulated differential voltage for the three low current cases represented in solid black and dashed red curves, respectively.

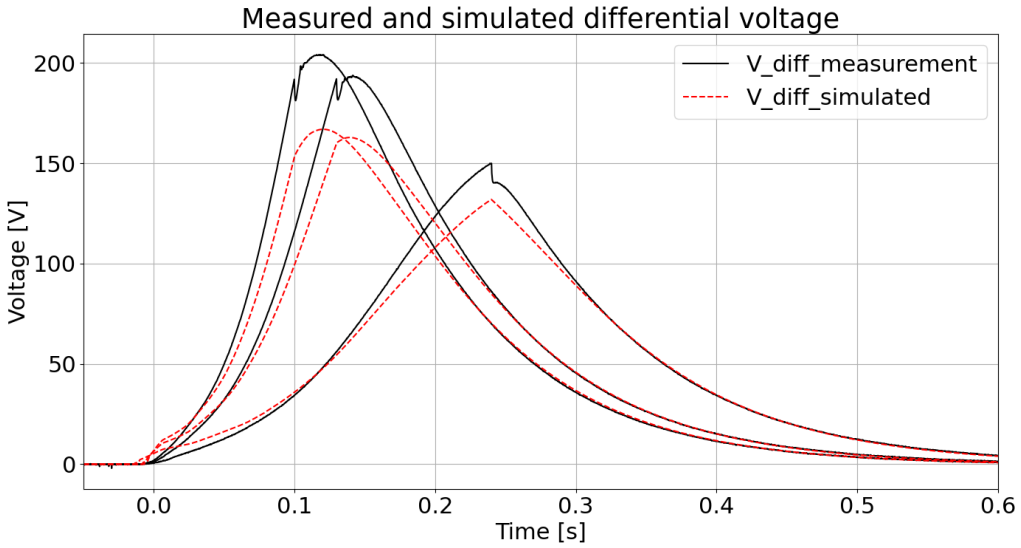

Figure 4.28: Measured and simulated differential voltage for the three high current cases represented in solid black and dashed red curves, respectively.

The main model parameters are summarized in Table 4.9. The most significant parameters being $wetted_p$ and $f_{internal,voids}$ with a value of 0.7 and 2 %, respectively.

Final parameters of the short model of the MBRD magnet [8]

f_{eff}		2
R_c	$\mu\Omega$	100
$wetted_p$		0.7
$f_{internal,voids}$	%	2

Table 4.9: Final parameters of the MBRD short model obtained by the validation.

As all measured discharges are analysed and the best fitting values for $wetted_p$ and $f_{internal,voids}$ are found, the consecutive simulation model of LEDET and PyBBQ is seen to be validated and can now be used to simulate the baseline MBRD magnet.

5 Simulation of MBRD baseline quench protection

In order to ensure the safety and integrity of the baseline MBRD magnet, the quench protection scheme will be validated with dedicated tests on a prototype magnet. As described in the preceding chapter, tests were already completed on a short model magnet, which were used to validate the consecutive simulation of PyBBQ and LEDET. Before starting the tests on the prototype magnet it will be possible to foresee potential damage in the magnet with the validated consecutive simulation. The baseline protection design for the MBRD magnet includes 16 QH strips arranged in 8 circuits. When a quench is detected, four out of eight QH circuits are powered. The remaining four circuits are not powered and are kept as spares. The layout and placement of the QHs in the coil section is the same as for the short model. The nomenclature is adopted and shown in Figure 5.1. All tests will not include an EE so the magnet will only be protected by QHs.

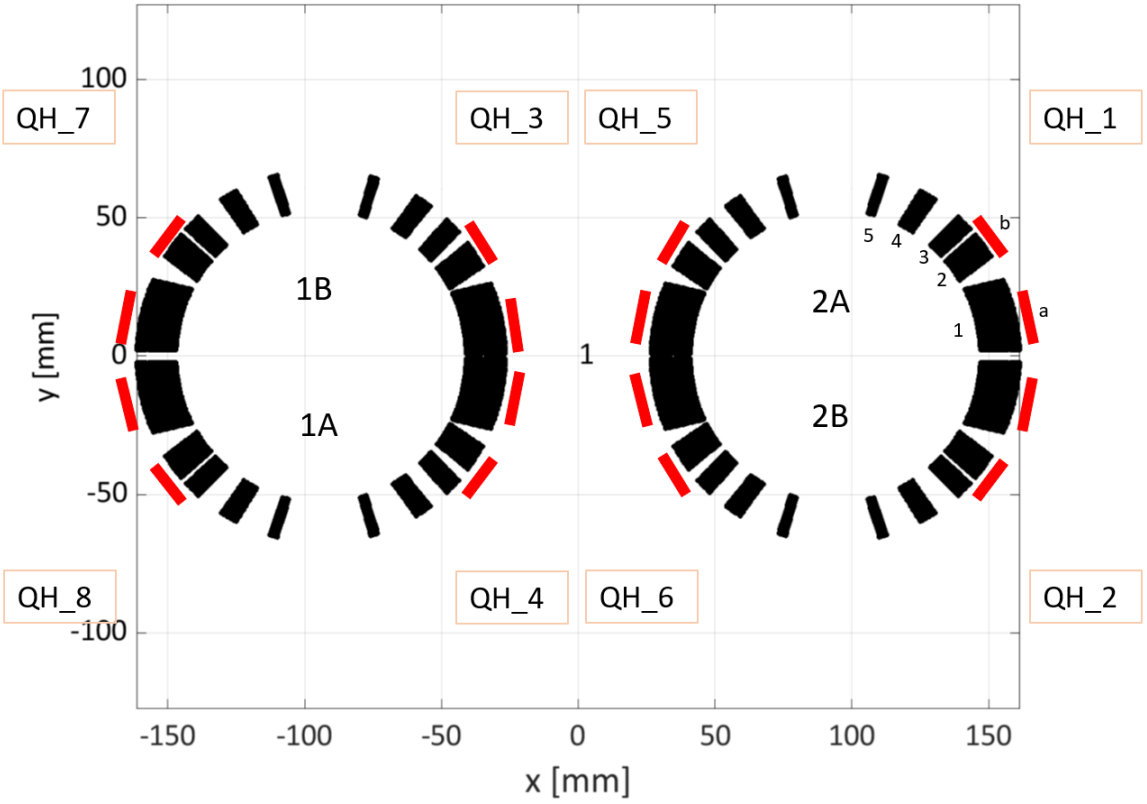

Figure 5.1: Cross-section of the baseline MBRD magnet, showing the 8 existing QH in their order, including the two strips. The two apertures and four different coils are indicated as well as the 5 blocks per coil.

Five different cases are defined for which key parameters of the magnet simulation have to stay below their thresholds to ensure the safety of the magnet in case of failures.

The considered parameters are the adiabatic temperature ($T_{adiabatic}$) of the hot-spot, the peak voltage to ground (U_{ground}) in the magnet, the peak turn to turn voltage ($U_{TurntoTurn}$) and the quench load calculated from $t = 0$ s. The quench load is the time integral of the magnet current squared written as following $\int I^2 dt$ and can be used to quantify the energy which is converted into heat inside the magnet. $T_{adiabatic}$ is calculated assuming adiabatic conditions in the spot where the quench starts from the time of the quench onset, which leads to a conservative hot-spot temperature value. All cases are summarized in Table 5.1, where the triggered QHs are indicated. Two cases use the baseline configuration of the protection system including QH1, QH3, QH6 and QH8 at nominal and ultimate current. Additionally three failure cases are defined in which one or two QHs are not functioning. In all simulations a quench is initiated at -27 ms in half-turn 186 which is part of block 5 of coil 2B. Starting a quench in the block furthest away from the mid-plane leads to a worst case scenario as the highest field occurs there leading to higher dissipated energy in the affected half-turns. The time of -27 ms to start the quench is chosen as it is an average value for t_{QH} taken from previous measurements [63]. By implementing Failure cases 2 and 3 two characteristic cases are covered in which one aperture is not protected (Failure case 3) and one where the coil in which the quench starts is not protected (Failure case 2).

Baseline and Failure cases for the MBRD prototype

Case name	QHs fired
Baseline / Nominal current	QH1, QH3, QH6, QH8
Baseline / Ultimate current	QH1, QH3, QH6, QH8
Failure 1 / Nominal current	QH1, QH3, QH6
Failure 2 / Nominal current	QH1, QH3
Failure 3 / Nominal current	QH1, QH6

Table 5.1: Summary of the five defined baseline and failure cases at their dedicated current levels. The QHs used are assigned to the related cases.

5.1 Simulation results

Performing the consecutive simulation with the baseline configuration at nominal and ultimate current leads to a $T_{adiabatic}$ of 292 K and 348 K, respectively. These values would be acceptable as they are still below the target temperature of 350 K which usually is referred to. U_{ground} is reasonable for both cases with values of 76 V and 95 V. The same accounts for $U_{TurntoTurn}$ at 48 V and 64 V. The quench load for nominal and ultimate current is 31.5 and 32.7 $10^6 \mathrm{A}^2\mathrm{s}$. The failure cases in comparison are partly exceeding the limits of hot-spot temperature and U_{ground}. While Failure case 1 still lies below the critical values with 336 K, 303 V, 56 V and 33.4 $10^6 \mathrm{A}^2\mathrm{s}$ both other cases lie above, reaching a $T_{adiabatic}$ equal to 410 K. U_{ground} is 335 V for Failure case 2 and 713 V for Failure case 3. $U_{TurntoTurn}$ equals 70 V for both cases. The values of the key parameters of the five defined cases are listed in Table 5.2. The increasing temperature with decreasing number of QHs can be explained by the slower discharge of the magnet for those cases giving the hot-spot more time to heat up. The very high value for U_{ground}

of Failure case 3 is caused by the asymmetry of the protection, as QH 1 and 6 are used, only aperture 2 is protected leading to high voltages to ground at the connecting turns between the apertures.

Key parameters of the MBRD prototype

Case name	$T_{adiabatic}$ [K]	U_{ground} [V]	$U_{TurntoTurn}$ [V]	Quench load [10^6A^{2}s]
Baseline / Nominal	292	76	48	31.5
Baseline / Ultimate	348	95	64	32.7
Failure 1 / Nominal	336	303	56	33.4
Failure 2 / Nominal	410	335	70	36.2
Failure 3 / Nominal	410	713	70	36.2

Table 5.2: Key parameters of the five defined cases using 4 QHs as protection. $T_{adiabatic}$ is calculated from -27 ms, U_{ground} is the maximum voltage to ground, $U_{TurntoTurn}$ is the maximum turn to turn voltage during the discharge and Quench load is the quench load calculated from t = 0 s.

The voltages to ground for the no-failure case and Failure case 3 at nominal current are shown in Figure 5.6 and Figure 5.7. The pattern of increasing and decreasing U_{ground} in Figure 5.6 develops due to resistive and inductive voltages occurring regularly after each other as all 4 QH circuits are working. As only aperture 2 is protected by QHs in Failure case 3 the behaviour of U_{ground} changes dramatically. The absolute voltage can develop to substantially higher values at the connecting turn between the apertures, as no resistive parts mitigate the inductive voltage in aperture 1.

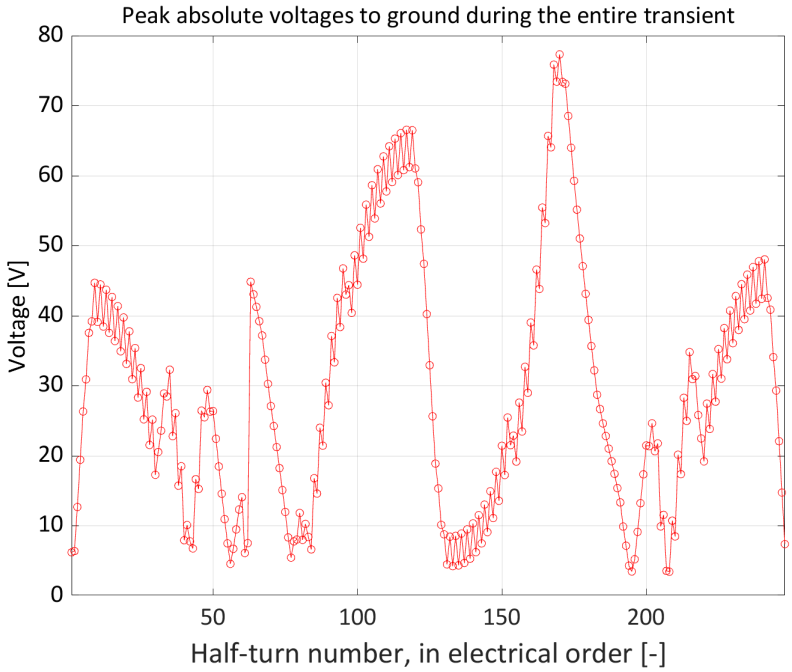

Figure 5.2: The absolute voltage to ground for each half-turn in electrical order is shown for the no-failure case at nominal current.

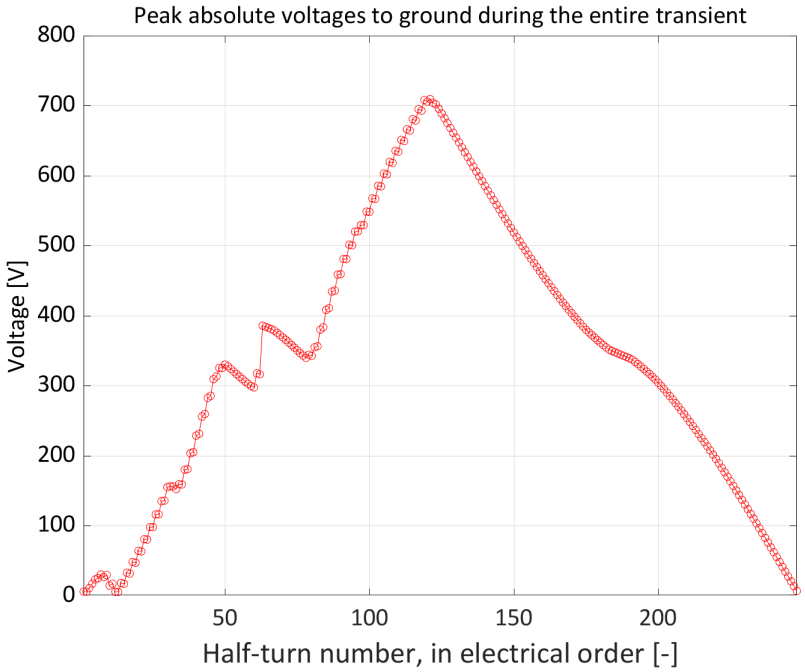

Figure 5.3: The absolute voltage to ground for each half-turn in electrical order is shown for Failure case 3.

As $T_{adiabatic}$ is calculated excluding heat transfer from the quenched hot-spot to the surrounding material, a more realistic temperature (T_{real}) can also be considered. This temperature is calculated including heat transfer to neighbouring turns and to the thermal sink. The simulated temperature distribution in the cross-section of the MBRD magnet for the no-failure case and Failure case 3 is shown in Figure 5.4 and Figure 5.5. In the no-failure case the symmetric pattern of the QHs is clearly visible. The Failure case shows the temperature difference between the apertures due to the asymmetric protection. In both cases the highest temperature is reached in the initially quenched half-turn 186. While the half-turns in contact to QHs remain below 200 K the hot-spot reaches 250 K and 350 K, respectively. These values can be acceptable, but no margin is kept.

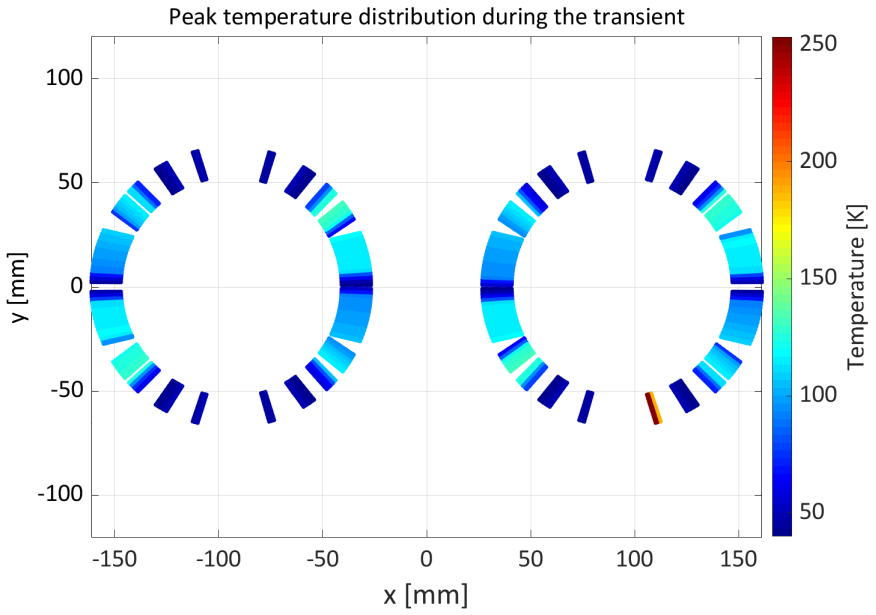

Figure 5.4: Cross-section of MBRD displaying the peak temperature including heat transfer to surrounding turns of every half-turn during the full discharge of the magnet using QHs 1, 3, 6 and 8. The case shown is the no-failure case at nominal current with an initiated quench in half-turn 186.

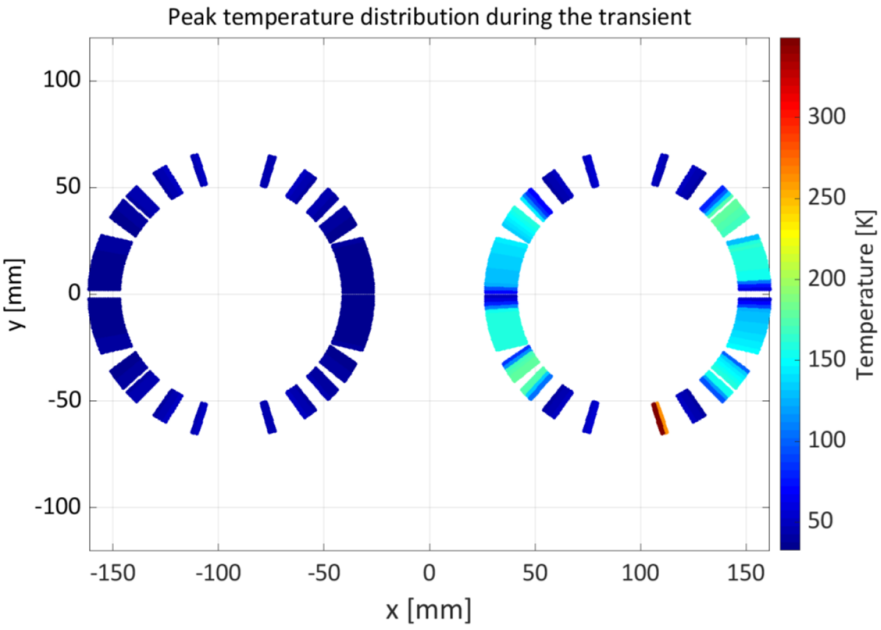

Figure 5.5: Cross-section of MBRD displaying the peak temperature including heat transfer to surrounding turns of every half-turn during the full discharge of the magnet using QHs 1 and 6. The case shown is Failure case 3 with an initiated quench in half-turn 186 and only protecting one aperture.

5.2 Proposed alternative quench protection scheme

An improvement of the protection system of MBRD magnet can be achieved by powering all available QH circuits. With this alternative scheme, a single or double QH unit failure would result in triggering 7 out of 8, or 6 out of 8 QH circuits, hence achieving better redundancy with respect to the current baseline. In this section, the proposed characteristic failure cases are: QH8 not being active for Failure case 1, QH2 and 6 failing in Failure case 2 and QH3 and 7 in Failure case 3. The baseline cases using 8 QHs and the resulting failure cases are shown in Table 5.3. In the Failure cases 2 and 3, it is chosen to assume a failure of the QH circuit attached to the coil that is in first or last electrical position in the magnet. These configurations are expected to achieve the highest U_{ground}, and are therefore representative of the worst-case scenario for the alternative protection scheme.

Baseline and Failure cases for the MBRD prototype using 8 QHs

Case name	QHs fired
Baseline / Nominal current	QH1, QH2, QH3, QH4, QH5, QH6, QH7, QH8
Baseline / Ultimate current	QH1, QH2, QH3, QH4, QH5, QH6, QH7, QH8
Failure 1 / Nominal current	QH1, QH2, QH3, QH4, QH5, QH6, QH7
Failure 2 / Nominal current	QH1, QH3, QH4, QH5, QH7, QH8
Failure 3 / Nominal current	QH1, QH2, QH4, QH5, QH6, QH8

Table 5.3: Summary of the five defined baseline and failure cases and the used current levels. The QHs used are assigned to the related cases.

Using all available QHs in the baseline for the MBRD magnet drastically reduced values for $T_{adiabatic}$, U_{ground}, $U_{TurntoTurn}$ and quench load can be achieved. The highest values for $T_{adiabatic}$, $U_{TurntoTurn}$ and quench load now occur for the no-failure case at ultimate current with 259 K, 43 V and 28.7 $10^6 A^2 s$. U_{ground} reaches its maximum for Failure case 3 with 396 V. These values all are acceptable and the magnet can safely operate in this configuration.

Key parameter of the MBRD prototype using 8 QHs

Case name	$T_{adiabatic}$ [K]	U_{ground} [V]	$U_{TurntoTurn}$ [V]	Quench load [$10^6 A^2 s$]
Baseline / Nominal	219	64	30	27.4
Baseline / Ultimate	259	83	43	28.7
Failure 1 / Nominal	232	158	34	28.3
Failure 2 / Nominal	250	352	38	29.3
Failure 3 / Nominal	250	396	38	29.3

Table 5.4: Key parameters of the five defined cases using 8 QHs as protection. $T_{adiabatic}$ is calculated from -27 ms, U_{ground} is the maximum voltage to ground, $U_{TurntoTurn}$ is the maximum turn to turn voltage during the discharge and quench load is the quench load calculated from t = 0 s.

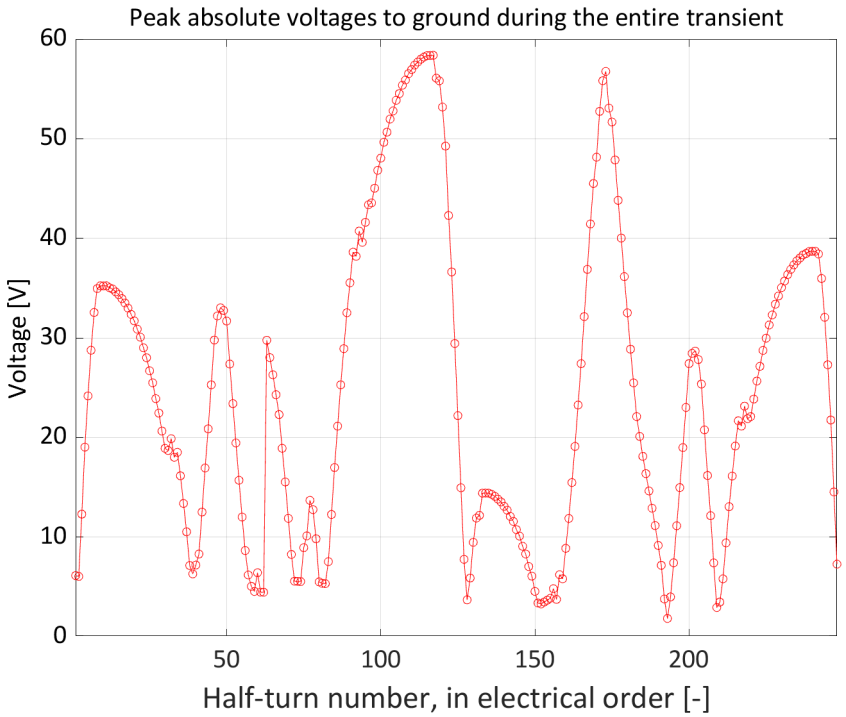

Figure 5.6: The absolute voltage to ground for each half-turn in electrical order is shown for the no-failure case using 8 QHs at nominal current.

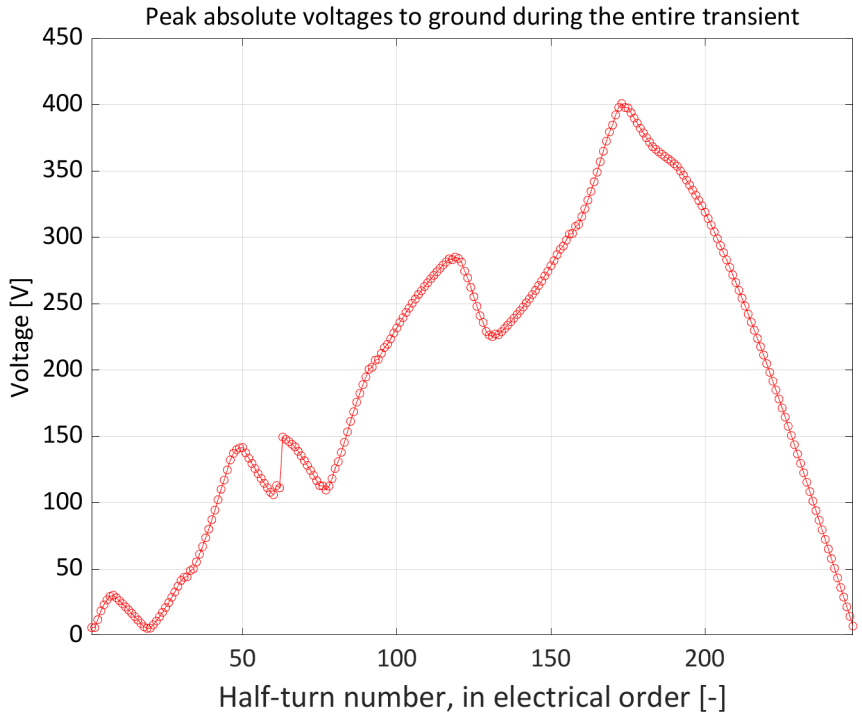

Figure 5.7: The absolute voltage to ground for each half-turn in electrical order is shown for Failure case 3 using 6 QHs.

As already observed for the protection scheme using 4 QHs the absolute voltage to ground is highly dependant on the pattern of resistive and inductive coil parts. While the case using 8 QH circuits shows the short successive resistive and inductive voltages, high inductive voltages develop in Failure case 3. The strong increase of inductive voltage in Failure case 3 is possible as the last coil in electrical position is not protected by QHs. In both cases the voltage stays significantly below the values of the protection scheme using 4 QHs.
The simulated temperature distribution in the cross-section of the MBRD magnet for the non-failure case and Failure case 3 considering 8 QHs as baseline are shown in Figure 5.8 and Figure 5.9. Both show significantly lower temperatures for the hot-spot compared to the protection scheme using 4 QHs. The maximum value for T_{real} now lies at 218 K in half-turn 186 and the half-turns below the QHs reach values below 120 K.

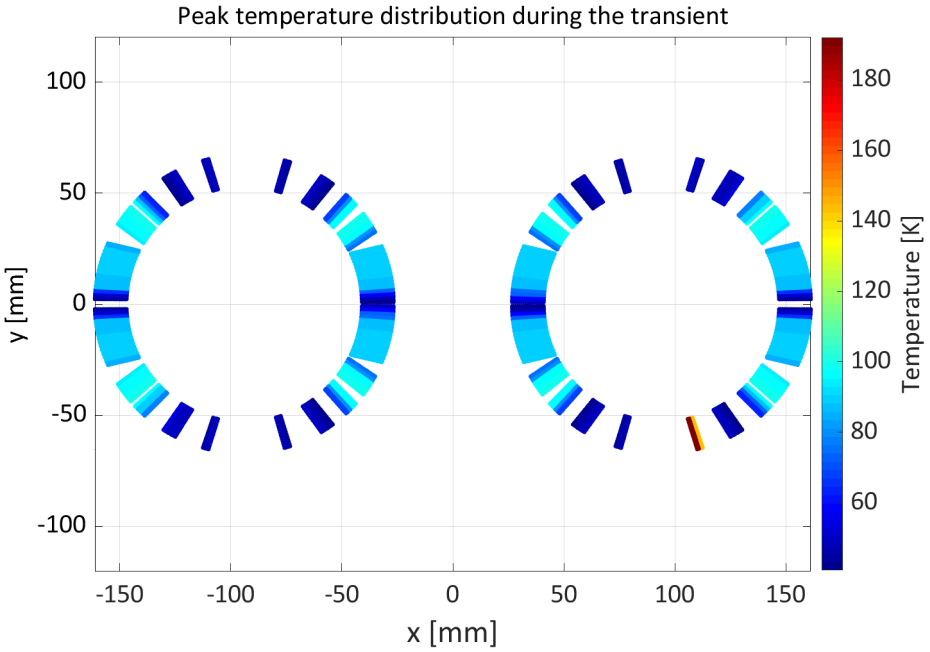

Figure 5.8: Cross-section of MBRD displaying the peak temperature of every half-turn during the full discharge of the magnet using all 8 QH circuits. The case shown is the no-failure case with an initiated quench in half-turn 186.

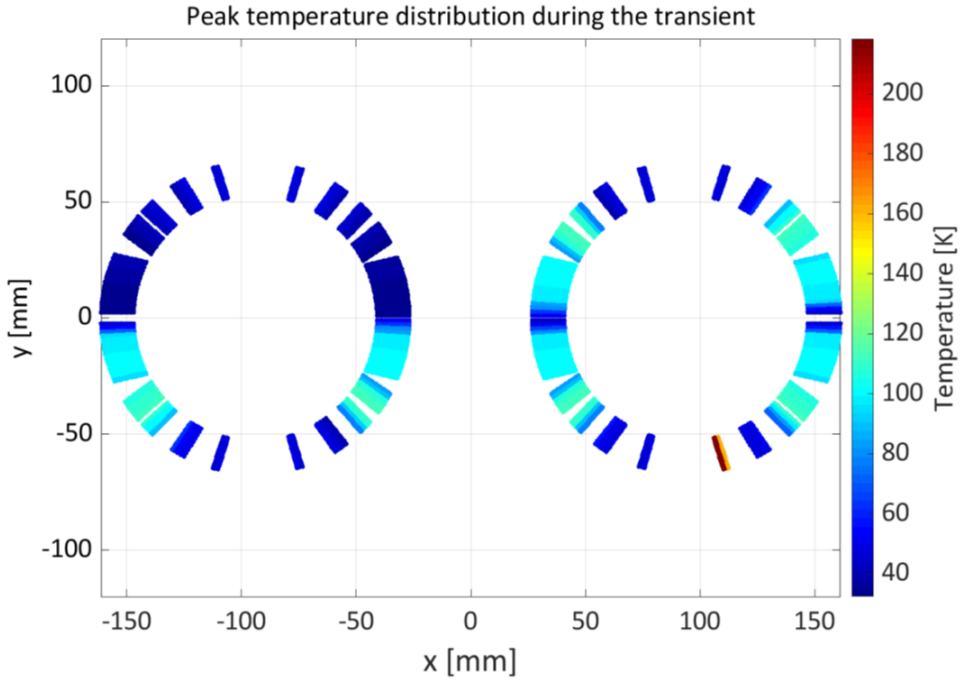

Figure 5.9: Cross-section of MBRD displaying the peak temperature of every half-turn during the full discharge of the magnet using 6 QHs. The case shown is Failure case 3 with an initiated quench in half-turn 186.

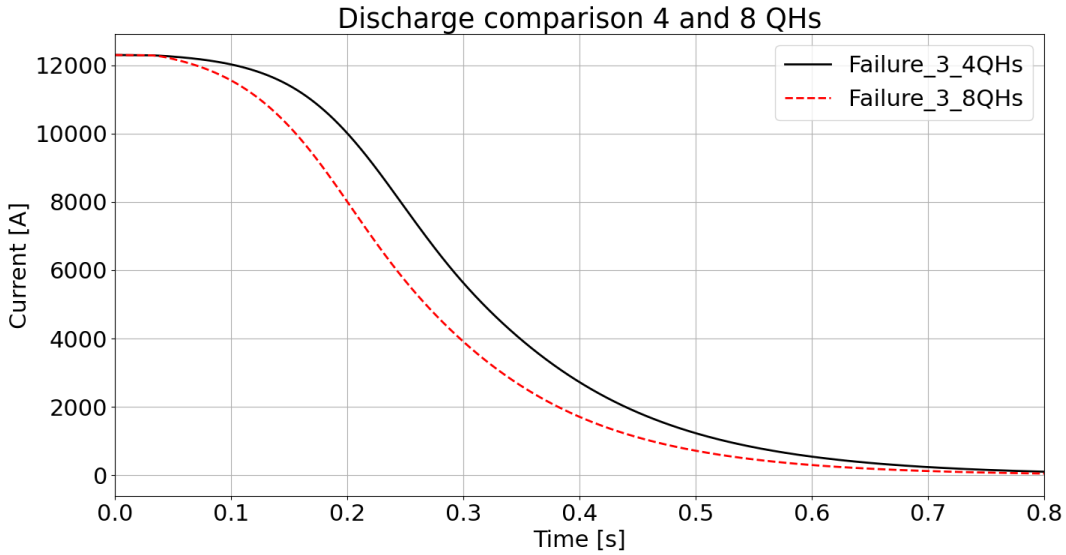

Figure 5.10: Full discharge comparison of Failure case 3 using 4 QHs as baseline, represented by the solid black curve. The dashed red curve represents Failure case 3 for the baseline of 8 QHs.

A comparison between the simulated magnet current in the worst case using 4 QH circuits and the worst case using 8 QH circuits is shown in Figure 5.10. It is clearly

visible that using 8 QH circuits a significantly faster discharge can be achieved through which lower hot-spot temperatures are obtained. The proposed alternative protection leads to reducing the simulated worst case hot-spot temperature by 160 K and the peak voltage to ground by 44 %. The reduction of these two key parameters of the magnet could give a significantly improved margin during the operation of the MBRD magnet in the future.

6 Conclusion

Superconducting magnets are one of the key components of the Large Hadron Collider (LHC) at the European Organization for Nuclear Research. Ensuring their safety and integrity as well as simulating and understanding transients occurring in superconducting circuits is very important. As part of the Performance Assessment and Electrical Quality Assurance section the STEAM (Simulation of Transient Effects in Accelerator Magnets) team developed a framework consisting of various in-house developed tools based on in-house developed code and commercial software. The STEAM framework allows to simulate multi-scale, multi-physics and multi-rate transients in superconducting magnets and circuits. As part of the framework a magnet model library exists, consisting mostly of LHC and HL-LHC (High Luminosity LHC) conductor, magnet, and circuit models. In order to validate the library, all models have to be compared to measurements and the effect of unknown parameters on the simulations has to be assessed. To enhance repeatability, consistency, traceability and versioning the STEAM-framework of standalone tools was restructured into a Python framework (STEAM-SDK), which relies on generalized YAML input files. With STEAM-SDK it is also possible to conduct analyses using customized functions specifically designed for the current use-case.
The main purpose of this thesis is the validation of a 2D electro-magnetic and thermal model of the HL-LHC recombination dipole magnet (MBRD), using the STEAM-SDK framework. The MBRD magnet is protected by quench heaters (QH). The LEDET 2D model reproduces adequately the transients at medium to high current, when the quench propagation velocity between coil parts in thermal contact to QH is fast (<10 ms). However, at low current the quench propagation velocity between heating stations needs to be considered to correctly capture quench transients. To accurately calculate the quench propagation between the QH heating stations and at the same time correctly capture the quench transient in the magnet a consecutive simulation approach was chosen. The simulation was implemented in the analysis structure of the STEAM-SDK. A customized simulation can be set up and run through a limited number of magnet-specific input parameters. The simulation output can be automatically compared with measurements by providing key metrics or used for automatically plotting various measured and simulated signals. The analysis can also provide predictions for key parameters for already validated magnet models implementing different operation scenarios and failure cases.
The developed consecutive simulation combines two tools part of the STEAM framework, namely STEAM-PyBBQ and STEAM-LEDET. While PyBBQ was used to simulate the initial quench propagation velocity on the conductor scale, LEDET simulates the QH-induced heat transfer, quench occurrence, heat diffusion between turns, ohmic loss and coupling losses in the magnet coils during the discharge. The pre-calculation of the quench propagation velocity with PyBBQ improves the simulation results as it varies significantly with the conductor current and is used to modify the simplified analytically-calculated quench propagation velocity that is calculated by LEDET, which notably does not account for the cooling effect of superfluid helium.

Motivated by the ability to connect a tool able to accurately simulate quench behaviour in superconducting conductors to the STEAM framework PyBBQ was recently implemented by a member of the STEAM team. As part of this thesis the benchmarking of the new tool against two other programs (BBQ and LEDET 3D) was successfully completed and documented. PyBBQ simulation results were analyzed for single and multi-strand cables as well as with and without including helium cooling.
The validation process of the consecutive simulation model was conducted by using measurements of a short model of the MBRD magnet. As the only significant difference between the short model and full-scale baseline magnet is its magnetic length, the simulation validated with the short model can be used to predict key parameters for the full-scale magnet and asses its safety in different operation and failure scenarios. In the validation process two important unknown parameters $f_{internal,voids}$, representing the fraction of voids in the cable filled with helium, and $wetted_p$, representing the fraction of strand perimeter in contact to superfluid helium, where found. The modification of $f_{internal,voids}$ leads to a change of the heat capacity of the cable which leads to a change in the simulated time when a quench starts in the cable. The proposed best value for $f_{internal,voids}$ lies at 2 % of the cable cross section. The impact of $wetted_p$ is restricted to the PyBBQ simulation by determining the cooling by superfluid helium which penetrated the cable. Simulations at 6000 A showed a significant impact of $wetted_p$ on the magnet discharge with a value of 0.7 leading to a very good match of simulation and measurement.
A few opportunities for improving the features of STEAM tools were identified. To better capture the start of the quench in the half-turns in thermal contact to QH strips in LEDET at low currents the heat diffusion in the longitudinal direction could be included. Furthermore, it should be discussed how the fraction of helium which penetrated the cable should be treated in case of a quench as it could evaporate and therefore reduce the heat capacity of the cable dramatically. To further improve the developed consecutive simulation specifically at low currents the QH heating stations assumptions in PyBBQ could be improved. By doing so the transient of the heat flow from the QH into the conductor through the insulation can be captured more accurately. This is very important at low currents as in order to calculate accurately the quench propagation velocity, one needs to include both heat diffused from the QH and ohmic loss developed in the conductor.
The developed and validated consecutive simulation model was successfully applied to the full-scale MBRD magnet. The baseline protection strategy of the full-scale MBRD magnet foresees to power 4 of the 8 existing QH circuits, while keeping the other four as spares. To evaluate the impact of QH circuit failure three failure scenarios at nominal current were introduced and compared to the reference case with all heaters working at nominal and ultimate current. Failure case 1 considers one QH circuit failure, while Failure cases 2 and 3 consider the failure of two QH circuits. The reference case at nominal current leads to an adiabatic hot-spot temperature ($T_{adiabatic}$) of 292 K and peak voltage to ground (U_{ground}) of 76 V, while the worst case (Failure case 3) leads to $T_{adiabatic}$ = 410 K and U_{ground} = 713 V. Since the simulated value lies above the desired limit of 350 K for $T_{adiabatic}$ an alternative baseline protection for the MBRD magnet was proposed and analyzed. The alternative scheme would foresee to power all eight available QH circuits. This leads to a significant reduction of $T_{adiabatic}$ to

259 K and U_{ground} to 396 V in the worst case scenario. These values need still to be confirmed by measurements on the first MBRD prototype magnet which are expected to be conducted during 2022.
To structure and generalize the developed simulation model a Python function was implemented which will make future validation processes for models of QH protected magnets very convenient. By adjusting the dedicated inputs a large number of operation scenarios can be automatically simulated and compared to measurement results, when available. Through the implementation of the simulation in the STEAM framework all simulations will remain traceable and reproducible in the future.

List of Figures

List of Tables

Annex

6.1 Annex to Chapter 4

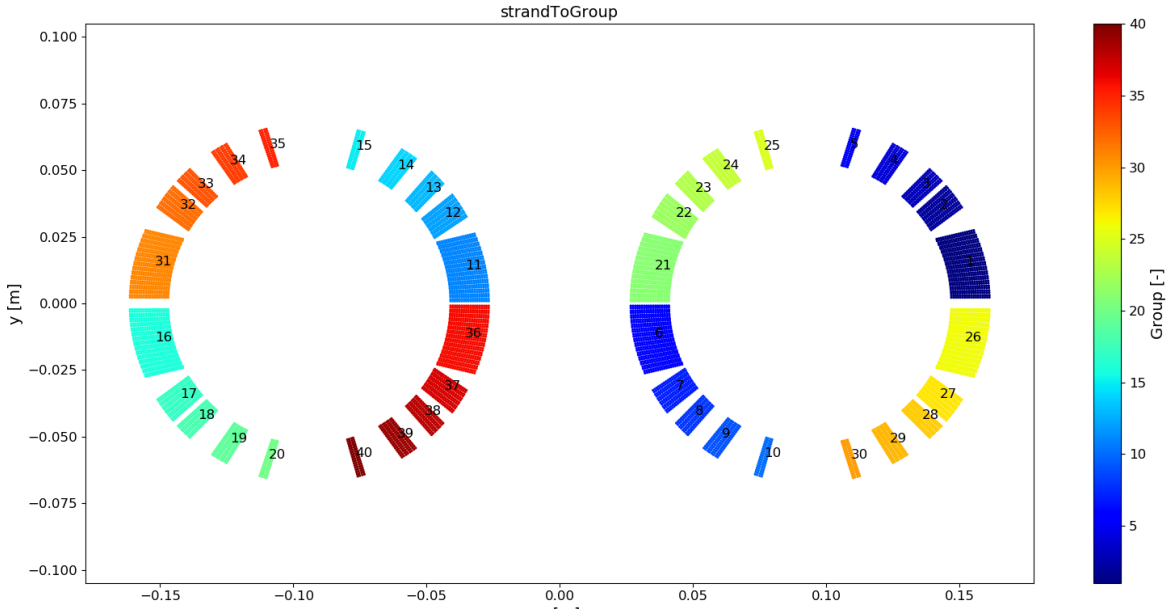

Figure 6.1: Cross-section of MBRD including the block numbering.

Half-turns to blocks

Block number	Half-turn number
1	1, 2, 3, 4, 5, 6, 7, 8, 9, 10, 11, 12, 13, 14, 15
2	16, 17, 18, 19, 20, 21
3	22, 23, 24, 25
4	26, 27, 28, 29
5	30, 31
6	32, 33, 34, 35, 36, 37, 38, 39, 40, 41, 42, 43, 44, 45, 46
7	47, 48, 49, 50, 51, 52
8	53, 54, 55, 56
9	57, 58, 59, 60
10	61, 62
11	63, 64, 65, 66, 67, 68, 69, 70, 71, 72, 73, 74, 75, 76, 77
12	78, 79, 80, 81, 82, 83
13	84, 85, 86, 87
14	88, 89, 90, 91
15	92, 93

16	94, 95, 96, 97, 98, 99, 100, 101, 102, 103, 104, 105, 106, 107, 108
17	109, 110, 111, 112, 113, 114
18	115, 116, 117, 118
19	119, 120, 121, 122
20	123, 124
21	125, 126, 127, 128, 129, 130, 131, 132, 133, 134, 135, 136, 137, 138, 139
22	140, 141, 142, 143, 144, 145
23	146, 147, 148, 149
24	150, 151, 152, 153
25	154, 155
26	156, 157, 158, 159, 160, 161, 162, 163, 164, 165, 166, 167, 168, 169, 170
27	171, 172, 173, 174, 175, 176
28	177, 178, 179, 180
29	181, 182, 183, 184
30	185, 186
31	187, 188, 189, 190, 191, 192, 193, 194, 195, 196, 197, 198, 199, 200, 201
32	202, 203, 204, 205, 206, 207
33	208, 209, 210, 211
34	212, 213, 214, 215
35	216, 217
36	218, 219, 220, 221, 222, 223, 224, 225, 226, 227, 228, 229, 230, 231, 232
37	233, 234, 235, 236, 237, 238
38	239, 240, 241, 242
39	243, 244, 245, 246
40	247, 248

Table 6.1: List of half-turns and in which block they are placed.

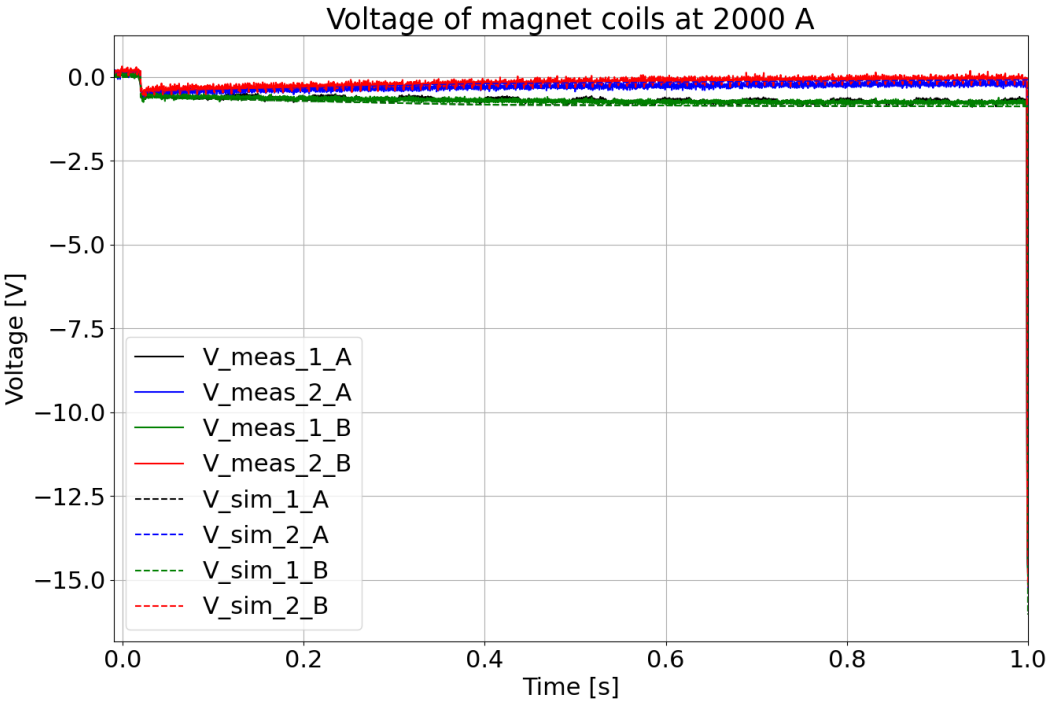

Figure 6.2: Coil voltages for the 2000 A discharge of the MBRD magnet.

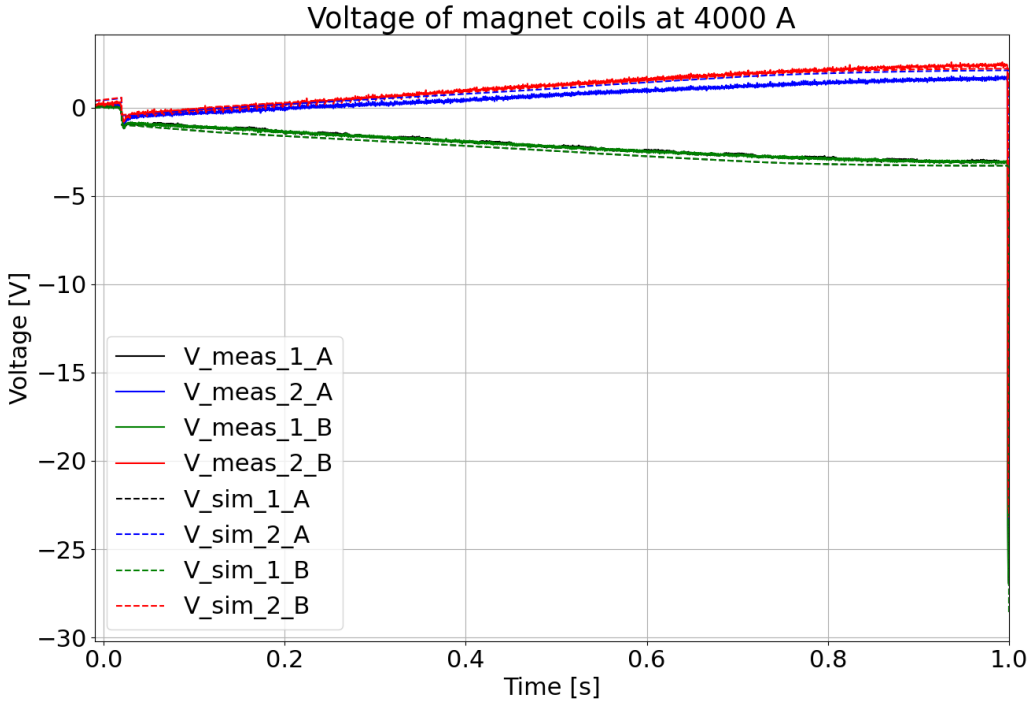

Figure 6.3: Coil voltages for the 4000 A discharge of the MBRD magnet.

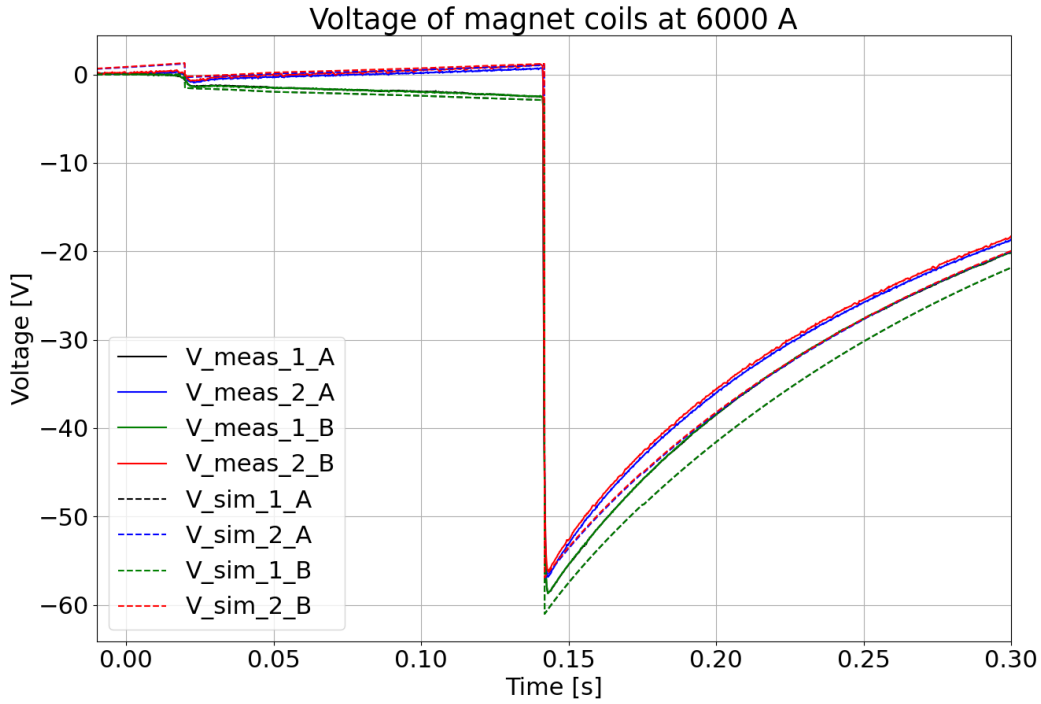

Figure 6.4: Coil voltages for the 6000 A discharge of the MBRD magnet.

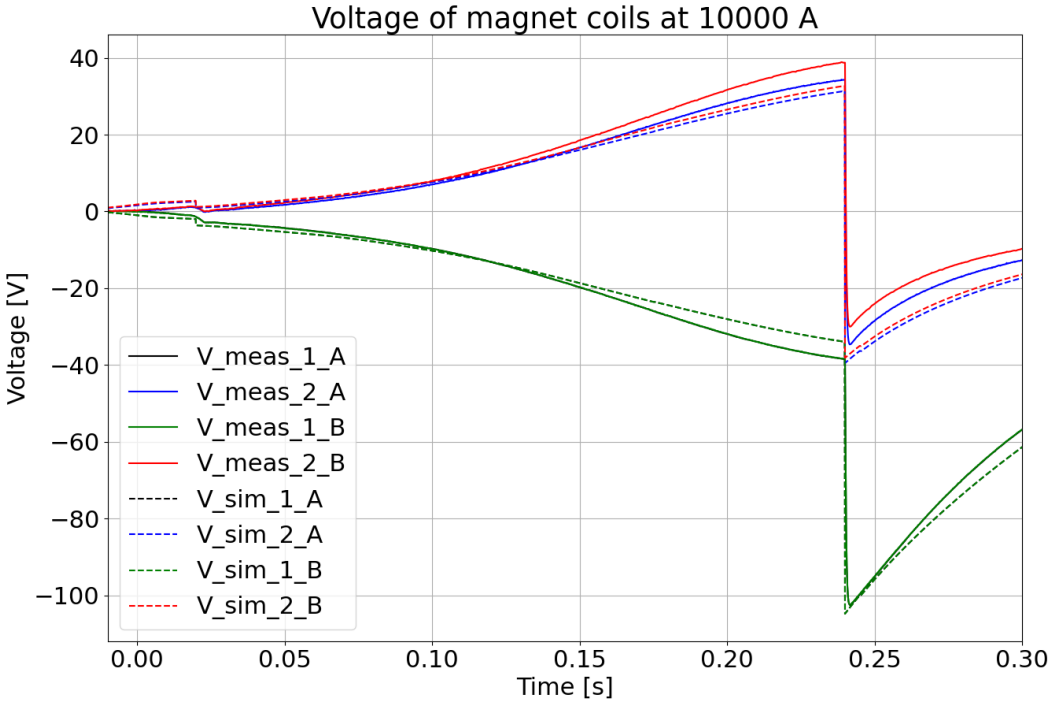

Figure 6.5: Coil voltages for the 10000 A discharge of the MBRD magnet.

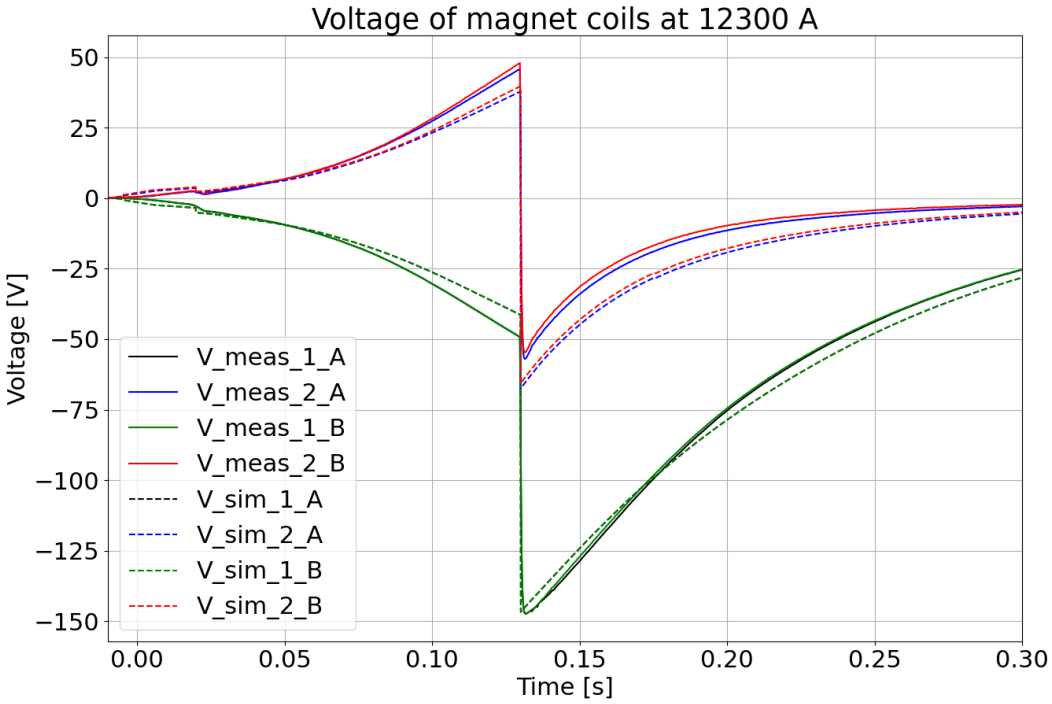

Figure 6.6: Coil voltages for the 12300 A discharge of the MBRD magnet.

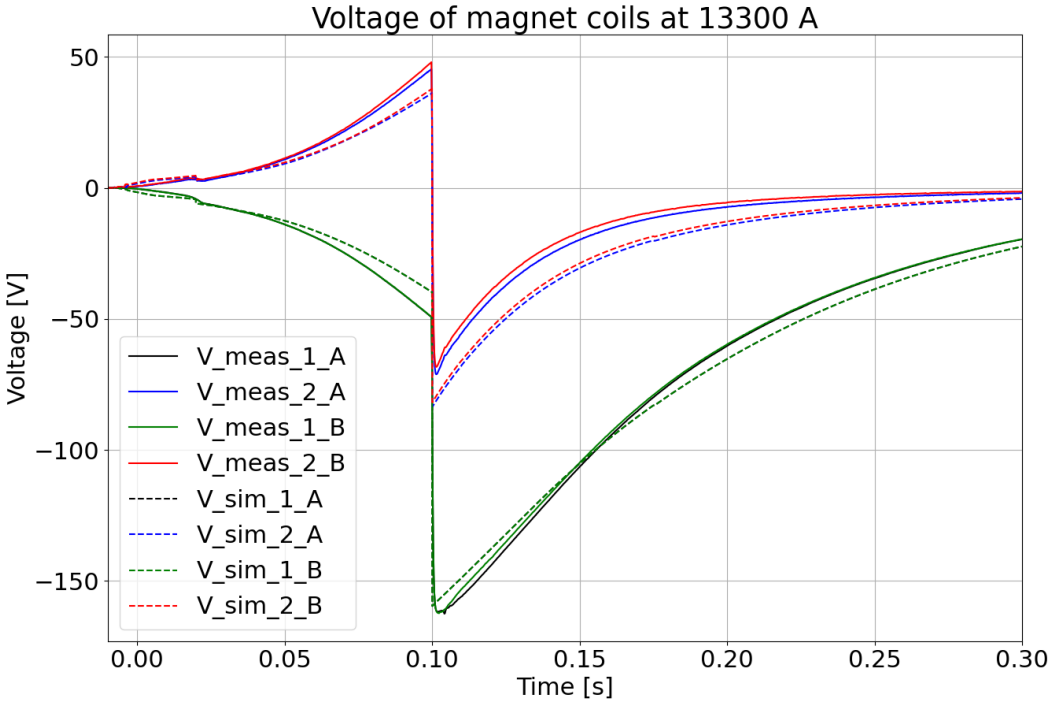

Figure 6.7: Coil voltages for the 13300 A discharge of the MBRD magnet.

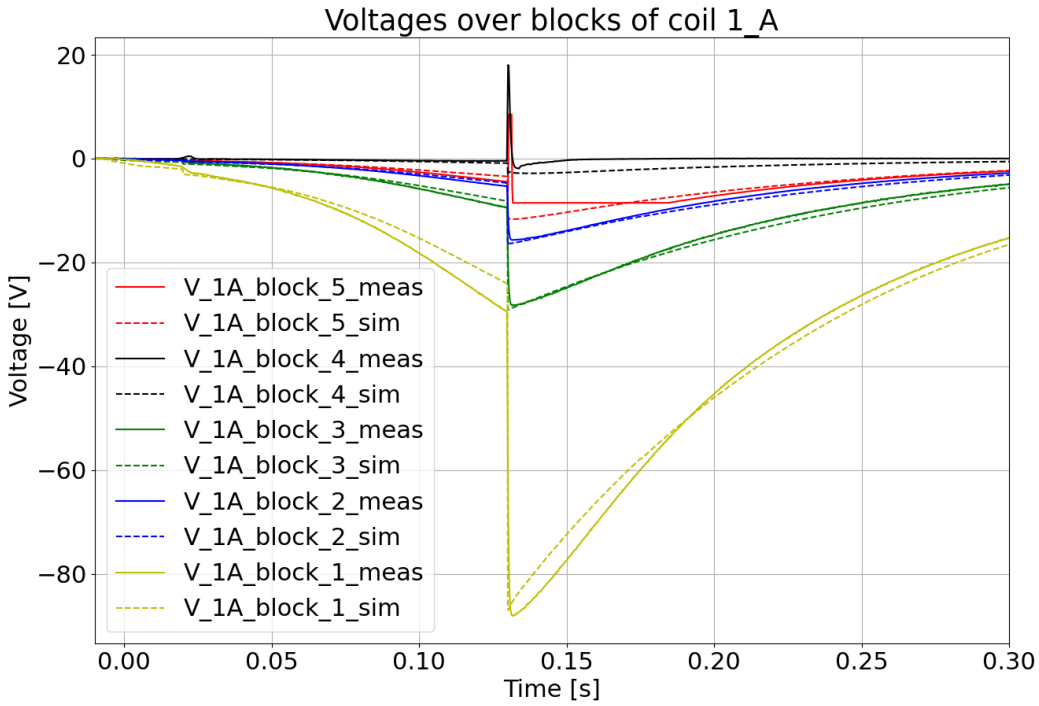

Figure 6.8: Block voltages for coil 1A for the 12300 A discharge of the MBRD magnet.

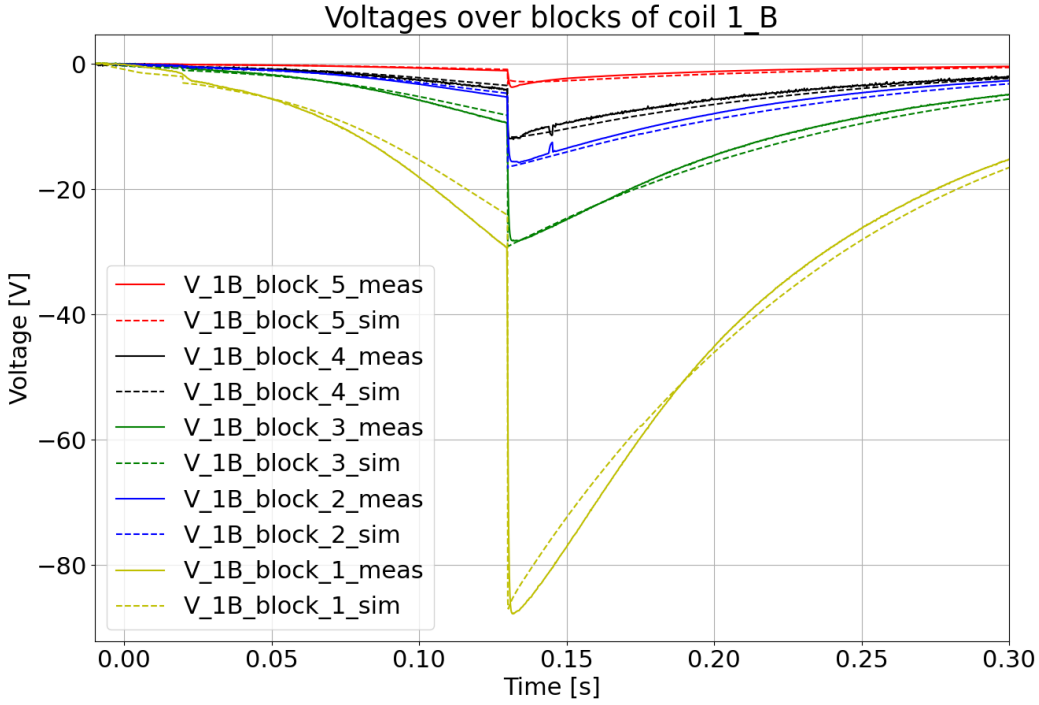

Figure 6.9: Block voltages for coil 1B for the 12300 A discharge of the MBRD magnet.

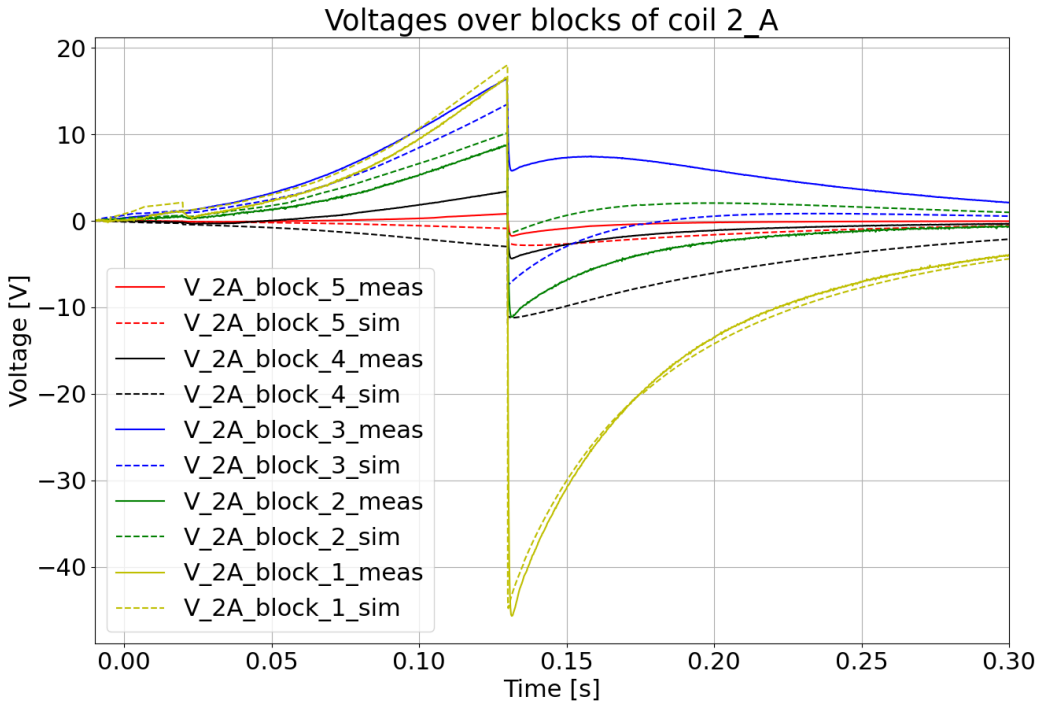

Figure 6.10: Block voltages for coil 2A for the 12300 A discharge of the MBRD magnet.

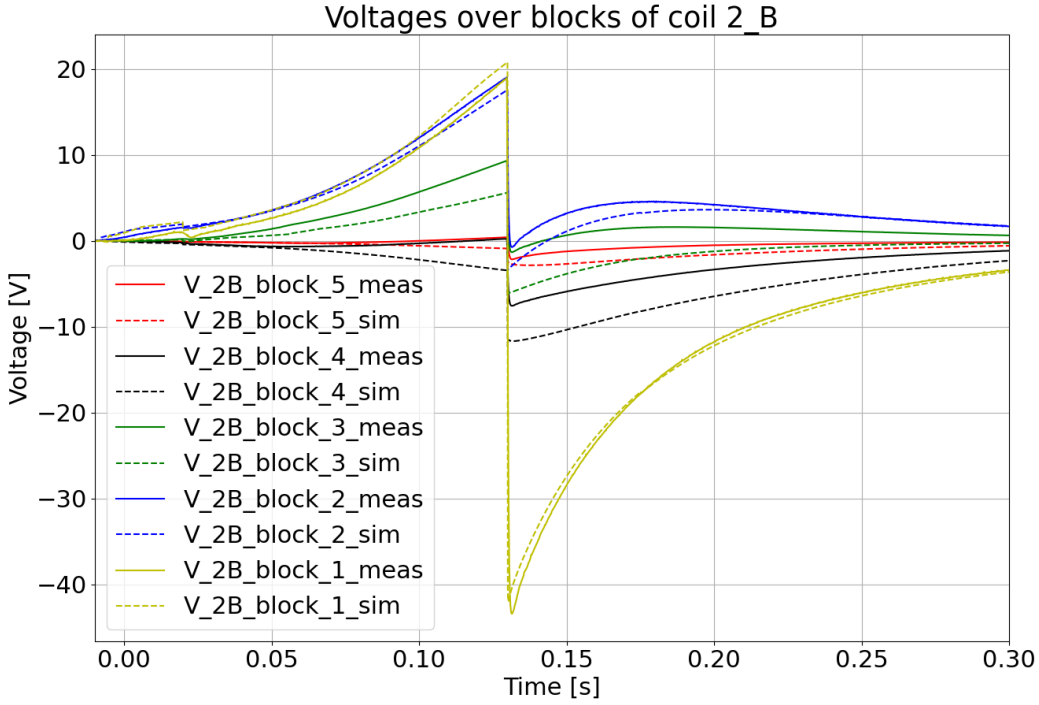

Figure 6.11: Block voltages for coil 2B for the 12300 A discharge of the MBRD magnet.

Bibliography

[1] University batch; URL: https://www.h-ka.de

[2] ATLAS Experiment, Exploring the secrets of the universe; URL: https://atlas.cern/

[3] Large Hadron Collider beauty experiment, The LHCb detector; URL: https://lhcb-public.web.cern.ch/en/Detector/Detector-en.html

[4] CMS website, Detector; URL: https://cms.cern/index.php/detector

[5] ALICE, ALICE detects quark-gluon plasma, a state of matter thought to have formed just after the Big Bang; URL: https://home.cern/science/experiments/alice

[6] CERN Website, "CERN's accelerator complex"; URL: https://home.web.cern.ch/science/accelerators/accelerator-complex?msclkid=de46f44ccf7011ec8414ec0d66fbc1a0

[7] CERN Website, "The Large Hadron Collider"; URL: https://home.cern/science/accelerators/large-hadron-collider

[8] I. Béjar Alonso, O. Brüning, P. Fessia, M. Lamont, L. Rossi, L. Tavian, M. Zerlauth "Vol. 10 (2020): High-Luminosity Large Hadron Collider (HL-LHC): Technical design report", 12.2020; DOI: 10.23731/CYRM-2020-0010

[9] High Luminosity LHC Project press releasde 2022; URL: https://home.web.cern.ch/press/2022/HL-LHC

[10] High Luminosity LHC Project; URL: https://hilumilhc.web.cern.ch/

[11] Superconductivity, An OpenLearn chunk used by permission of The Open University copyright (2019); License: https://creativecommons.org/licenses/by-nc-sa/4.0/deed.en_GB, URL: https://www.open.edu/openlearn/science-maths-technology/engineering-technology/superconductivity/content-section-0?intro=1

[12] Daniel Schoerling, "Superconducting accelerator magnets", 19.05.2021; URL: https://indico.cern.ch/event/1018359/contributions/4312237/attachments/2246966/3811056/Schoerling_CASatEAS_2021.pdf

[13] Philipp Krüger, "Optimisation of hysteretic losses in high-temperature superconducting wires", PhD thesis, Karlsruhe Institute of Technology, 2014; ISBN: 978-3-7315-0185-5

[14] Werner Buckel, Reinhold Kleiner, "Supraleitung, Grundlagen und Anwendung", 2013; ISBN: 978-3-527-66870-0

[15] Steve Myers, “The engineering needed for particle physics”, Philosofical transactions of the royal society a mathematical, physical and engineering sciences 08.22.2012; DOI: 10.1098/rsta.2011.0053

[16] National high magnetic field laboratory, Nb-Ti Image Gallery; Light microscope montage for SSC Nb-Ti strand manufactured by IGC-AS; URL: https://nationalmaglab.org/images/magnet_development/asc/image_gallery/nb_ti/nb_ti_light_microscope_small.jpg

[17] A. Godeke, “Performance Boundaries in Nb3Sn Superconductors”, PhD thesis, University of Twente, 2005; URL: https://research.utwente.nl/en/publications/performance-boundaries-in-nb3sn-superconductors

[18] Emmanuele Ravaioli, “CLIQ, A new quench protection technology for superconducting magnets”, PhD thesis, University of Twente, 2015; URL: http://cds.cern.ch/record/2031159/

[19] Lucio Rossi, “Superconducting Magnets for the LHC”, CERN Accelerator School 26 February 2009 - Divonne; URL: https://cas.web.cern.ch/sites/default/files/lectures/divonne-2009/rossi.pdf

[20] L.Bottura, “Cable stability”, 2014; DOI: 10.5170/CERN-2014-005.401

[21] Stephan Russenschuk, “Field Computation for Accelerator Magnets”, WILEY-VCH Verlag GmbH & Co. KGaA, Weinheim, Germany, 2010; ISBN: 978-3-527-40769-9, DOI: 10.1002/9783527635467

[22] H. ten Kate, H. Boschman, and L. van de Klundert, “Longitudinal propagation velocity of the normal zone in superconducting wires”, IEEE Transactions on Magnetics 23.2 (1987), pp. 1557–1560.; DOI: 10.1109/TMAG.1987.1065020

[23] Herman ten Kate, “Superconducting Magnets: Quench Propagation and Protection”, 2013; URL: https://indico.cern.ch/event/194284/contributions/1472819/attachments/281522/393603/TenKate_-_CAS_-Handout-Quench-Erice-2103.pdf

[24] A. Siemko, “Magnet quench process”, Chamonix 11 workshop; URL: https://cds.cern.ch/record/567209/files/7-4-as.pdf

[25] A. Verweij, V. Baggiolini, A. Ballarino, B. Bellesia, F. Bordry, A. Cantone, M. Casas Lino, A. Castaneda Serra, C. Castillo Trello, N. Catalan Lasheras, Z. Charifoulline, G. Coelingh, K. Dahlerup-Petersen, G. D’Angelo, R. Denz, S. Feher, R. Flora, M. Gruwe, V. Kain, B. Khomenko, G. Kirby, A. MacPherson, A. Marqueta Barbero, K.-H. Mess, M. Modena, R. Mompo, V. Montabonnet, S. le Naour, D. Nisbet, V. Parma, M. Pojer, L. Ponce, A. Raimondo, S. Redaelli, H. Reymond, D. Richter, G. de Rijk, A. Rijllart, I. Romera Ramirez, R. Saban, S. Sanfilippo, R. Schmidt, A. Siemko, M. Solfaroli Camillocci, Y. Thurel, H. Thiessen, W. Venturini Delsolaro, A. Vergara Fernandez, R. Wolf, M. Zerlauth, “PERFORMANCE OF THE MAIN DIPOLE MAGNET CIRCUITS

OF THE LHC DURING COMMISSIONING", LHC Project Report 1140, 11th European Particle Accelerator Conference, June 2008, Genoa, Italy; URL: https://cds.cern.ch/record/1124069/files/LHC-PROJECT-REPORT-1140.pdf

[26] F. Rodriguez-Mateos, R. Schmidt, A. Siemko and F. Sonnemann, "Quench Process and Protection of LHC Dipole Magnets", LHC Project Note 184, 1999; URL: https://cds.cern.ch/record/692002

[27] V. Mnroussov, S. Sanfilippo and A. Siemko, "Temperature Profiles During Quenches in LHC Superconducting Dipole Magnets Protected by Quench Heaters", IEEE Transactions on Applied Superconductivity, Volume: 10, Issue: 1, March 2000; DOI: 10.1109/77.828320

[28] G. Chlachidze, G. Ambrosio, M. Anerella, F. Borgnolutti, R. Bossert, S. Caspi, D.W. Cheng, D. Dietderich, H. Felice, P. Ferracin, A. Ghosh, A. Godeke, A.R. Hafalia, M. Marchevsky, D. Orris, P.K. Roy, G.L. Sabbi, T. Salmi, J. Schmalzle, C. Sylvester, M. Tartaglia, J. Tompkins, P. Wanderer, X.R. Wang, and A.V. Zlobin, "Performance of HQ02, an Optimized Version of the 120 mm N b3Sn LARP Quadrupole", IEEE Transactions on Applied Superconductivity, vol. 24, no. 3, June 2014; DOI: 10.1109/TASC.2013.2285885

[29] Marvin Janitschke, "Thermal analysis of quench-heater heating stations using STEAM-BBQ", 2nd STEAM Workshop, 10.2021; URL: https://indico.cern.ch/event/1060073/contributions/4454956/

[30] T. Mulder, "Tagged and working version of PyBBQ"; URL: https://gitlab.cern.ch/steam/pybbq/-/tags/2022.01

[31] E. Todesco, "Quench limits in the next generation of magnets", CERN Yellow Report CERN-2013-006, pp.10-16; URL: https://cds.cern.ch/record/1643430/files/p10.pdf

[32] Zlobin A. V. (Fermilab), Andreev N. (Fermilab), Apollinari G. (Fermilab), Auchmann B. (CERN), Barzi E. (Fermilab), Izquierdo Bermudez S. (CERN), Bossert R. (Fermilab), Buehler M. (Fermilab), Chlachidze G. (Fermilab), DiMarco J. (Fermilab), Karppinen M. (CERN), Nobrega F. (Fermilab), Novitski I. (CERN), Rossi L. (CERN), Smekens D. (CERN), Tartaglia M. (Fermilab), Turrioni D. (Fermilab), Velev Genadi (Fermilab), "11 T Twin-Aperture Nb3Sn Dipole Development for LHC Upgrades", IEEE Trans. Appl. Supercond. 25 (2015) 4002209; DOI: 10.1109/TASC.2014.2367312

[33] Barbara Caiffi, Andrea Bersani, Roberto Cereseto, Pasquale Fabbricatore, Stefania Farinon, Lucio Fiscarelli, Arnaud Foussat, Filippo Levi, Franco Mangiarotti, Alessandra Pampaloni, Ezio Todesco, Salvador Ferradas Troitino, and Gerard Willering, "The Development of the Superconducting Dipoles D2 for the High Luminosity Upgrade of LHC", IEEE Transactions on Applied Superconductivity (Volume: 31, Issue 5, Aug. 2021); DOI: 10.1109/TASC.2021.3057561

[34] E. Todesco et al, “The High Luminosity LHC interaction region magnets towards series production”, 2021 Supercond. Sci. Technol. 34 053001; URL: https://iopscience.iop.org/article/10.1088/1361-6668/abdba4

[35] HiLumi LHC Work Package 3 - Magnets for Insertion Regions, MBRD; Cross-section of MBRD; URL: https://espace.cern.ch/HiLumi/WP3/SiteAssets/SitePages/MBRD/D2.jpg

[36] L. Bender, B.Caiffi, P.Fabbricatore, F.Levi, A.Pampaloni, E.Ravaioli, “Quench and protection of D2 magnet (MBRD) for the High Luminosity upgrade of LHC”, Report 02.15.2022; URL: https://edms.cern.ch/ui/#!master/navigator/document?P:100989895:101042045:subDocs

[37] STEAM team, “Tagged and working version of STEAM-SDK on gitlab”; URL: https://gitlab.cern.ch/steam/steam_sdk/-/tags/2022.01

[38] STEAM team, “Version of STEAM-SDK used in this thesis”; URL: https://pypi.org/project/steam-sdk/

[39] E.Ravaioli and M.Wozniak, “STEAM framework for simulation of transients in superconducting magnet circuits”, TE-MPE-PE section meeting 06.08.22; URL: https://indico.cern.ch/event/1149931/

[40] M. Mentink et al., “Quench Behavior of the HL-LHC Twin Aperture Orbit Correctors”, IEEE Trans. on Appl. Supercond. 28, p 4004806 (2018); URL: https://ieeexplore.ieee.org/document/8260839

[41] STEAM team, “FiQus code”; URL: https://gitlab.cern.ch/steam/fiqus

[42] L. Bortot, B. Auchmann, I. Cortes Garcia, A. M. Fernandez Navarro, M. Maciejewski, M. Prioli, S. Schöps, A. Verweij, “A 2-D Finite-Element Model for Electro-Thermal Transients in Accelerator Magnets”, IEEE Transactions on Magnetics, 2017; URL: https://ieeexplore.ieee.org/document/8024019

[43] E. Ravaioli, B. Auchmann, M. Maciejewski, H.H.J. ten Kate, A.P. Verweij, “Lumped-Element Dynamic Electro-Thermal model of a superconducting magnet”, Cryogenics, Volume 80, Part 3, December 2016, Pages 346-356; DOI: 10.1016/j.cryogenics.2016.04.004

[44] E. Ravaioli, “Tagged version of LEDET on gitlab”; URL: https://gitlab.cern.ch/steam/steam-ledet/-/tags/LEDET_v2.02.15

[45] E. Ravaioli, O. Tranum Arnegaard, A. Verweij, M. Wozniak, “Quench Transient Simulation in a Self-Protected Magnet With a 3-D Finite-Difference Scheme”, IEEE Trans. on Appl. SC, 2022; URL: https://ieeexplore.ieee.org/document/9743807

[46] M. Mentink et al., “Quench Behavior of the HL-LHC Twin Aperture Orbit Correctors”, IEEE Trans. on Appl. Supercond. 28, p 4004806 (2018); URL: https://ieeexplore.ieee.org/document/8260839

[47] STEAM: Simulation of Transient Effects in Accelerator Magnets; URL: https://espace.cern.ch/steam/

[48] L. Bortot, B. Auchmann, I. Cortes Garcia, A.M. Fernandez Navarro, M. Maciejewski, M. Mentink, M. Prioli, E. Ravaioli, S. Schöps, A. Verweij SSTEAM: A hierarchical cosimulation framework for superconducting accelerator magnet circuits.ÏEEE Transactions on applied superconductivity 28.3 (2017): 1-6; URL: https://ieeexplore.ieee.org/document/8240720

[49] Marvin Janitschke, "Framework for automatic superconducting magnet model generation & validation against transients measured in LHC magnets", December 2021, Berlin; URL: https://cds.cern.ch/record/2799810

[50] A. P. Verweij, "Electrodynamics of Superconducting Cables in Accelerator Magnets", PhD thesis, University of Twente, 1995; URL: https://cds.cern.ch/record/292595/files/Thesis-1995-Verweij.pdf

[51] G. H. Morgan, "Theoretical Behavior of Twisted Multicore Superconducting Wire in a Time–Varying Uniform Magnetic Field", In: Journal of Applied Physics 41.9 (1970), pp. 3673–3679; DOI: 10.1063/1.1659491

[52] Federica Murgia, "Multiphysics Modelling of the LHC Individually Powered Quadrupole Superconducting Circuits", 2020, Bologna; URL: https://cds.cern.ch/record/2729131/files/CERN-THESIS-2020-102.pdf

[53] Dimitri Pracht, "Multiphysics modelling of the LHC main quadrupole superconducting circuit", 2019, Hochschule Hanover; URL: http://cds.cern.ch/record/2681097/files/CERN-THESIS-2019-071.pdf

[54] Marvin Janitschke, Matthias Mentink, Federica Murgia, Dimitri Pracht, Emmanuele Ravaioli and Arjan P. Verweij, "A Simplified Approach to Simulate Quench Development in a Superconducting Magnet", IEEE TRANSACTIONS ON APPLIED SUPERCONDUCTIVITY, VOL. 31, NO. 5, AUGUST 2021; DOI: 10.1109/TASC.2021.3059980

[55] Matthias Mentink and Michal Maciejewski, "STEAM-BBQ user manual v1.0", 2019, Technical Note; URL: https://edms.cern.ch/ui/#!master/navigator/document?D:100379191:100379191:subDocs

[56] Martin N. Wilson, "Superconducting Magnets", March 1987, Pages: 204-217; ISBN: 9780198548102

[57] STEAM team, "steam-ledet-material-library"; URL: https://gitlab.cern.ch/steam/steam-ledet-material-library

[58] STEAM team, "steam-material-library"; URL: https://gitlab.cern.ch/steam/steam-material-library

[59] O. Brüning, P. Collier, P. Lebrun, S. Myers, R. Ostojic, J. Poole, P. Proudlock, "LHC Design Report", 2004; DOI: 10.5170/CERN-2004-003-V-1

[60] STEAM team, “Tagged and working version of steam-models on gitlab”; URL: https://gitlab.cern.ch/steam/steam_models/-/tags/2022.01

[61] STEAM team, “Tagged and working version of steam-model-dev on gitlab”; URL: https://gitlab.cern.ch/steam/steam-models-dev/-/tags/2022.01

[62] “SM18 magnet test facility at CERN”; URL: http://sm18-operation.web.cern.ch/sm18new.asp?wycf=0

[63] G. Willering, “QUENCH ANALYSIS VOLTAGE BUILD UP ANALYSIS”, 03.2022; URL: https://edms.cern.ch/document/2677676/1